Università degli Studi di Modena e Reggio Emilia

PhD Program in Molecular and Regenerative Medicine

Cycle XXXV

Detection of Aging Biomarkers with Organic Electronics

Pamela Allison Manco Urbina

Supervisor

Prof. Carlo Augusto Bortolotti

Coordinator

Prof. Michele de Luca

ABSTRACT

‘‘Inflammaging’’ refers to the chronic, low-grade proinflammatory status associated with aging, in which biomarkers could predict physical and cognitive performance, as well as mortality in the elderly population. Although there is no specific biomarker, epidemiological evidence associates elevated levels of inflammatory mediators and the immune response to the recurrent infection by cytomegalovirus (CMV) with this condition. The current gold standard techniques for inflammatory biomarkers detection are Enzyme-linked immunosorbent assay and Flow cytometry-based technologies. Both techniques rely on antibody-antigen interaction, and colorimetric reaction to quantitatively determine the specific analyte. These techniques are very robust and characterized by high sensitivity and specificity; however, they require a relatively large amount of sample, specialized equipment and personnel, as well as fluorescent labeling. These disadvantages hamper their implementation at the point-of-care (PoC) and as portable devices.

Within this thesis, we propose the development of biosensors based on Electrolyte Gated Organic Transistors (EGOTs) as an alternative to conventional techniques. EGOTs are rapidly emerging as one of the architectures of choice for label-free biosensing for their outstanding capability of amplification of small biological signals, operating at low voltages, and with a low-cost fabrication. As their inorganic counterpart, they are three-terminal devices, comprising source and drain electrodes connected by the organic semiconductor (OSC), and a third gate electrode, connected to the OSC through the electrolyte, using the Field-Effect Transistor terminology. The gate electrode is capacitively coupled to the OSC, therefore a potential application at the gate electrode leads to the formation of a first electrical double layer (EDL) at the gate/electrolyte interface, which induces the formation of a second EDL at the OSC/electrolyte interface, tunning the transistor electrical performance.

The aim of this thesis is the development of individual EGOT-based biosensors for four aging biomarkers: Interleukin 6 (IL-6), Interleukin 1β (IL-1β), anti-CMV antibodies, and p-Tau_{181}. To this end, two EGOT architectures were explored, Organic Electrochemical Transistors (OECTs) and Electrolyte-Gated Field Effect Transistors (EGOFETs) as biosensors, which differ in the permeability of the OSC to ions penetration, and both working as potentiometric biosensors. In order to use EGOTs as biosensors, they were endowed with biorecognition capabilities by immobilizing biorecognition elements (e.g., antibodies) on the gate electrode.

Consequently, the biorecognition event at the gate/electrolyte interface is transduced and amplified into a change in the drain current. During this thesis, different gate functionalization strategies were studied, optimized, and validated with complementary techniques, such as Electrochemical Impedance Spectroscopy (EIS) and Surface Plasmon Resonance (SPR).

We demonstrated the detection of these biomarkers in the physio-pathological range, exploiting EGOT-based biosensors not only as a sensing tool but also for investigating the biorecognition phenomena occurring at the gate/electrolyte interface. Additionally, the integration of these devices with microfluidics led to the real-time monitoring of proteins, bringing the bench lab closer to PoC testing.

This work is the beginning of the development of multiplexing sensing platforms based on EGOT architectures, with the aim to implement it at PoC testing.

SINTESI

Il termine "Inflammaging" si riferisce allo stato proinfiammatorio cronico di basso grado associato all'invecchiamento, in cui i biomarcatori potrebbero prevedere le prestazioni fisiche e cognitive, nonché la mortalità nella popolazione anziana. Sebbene non esistano biomarcatori specifici, l'evidenza epidemiologica associa l'inflammaging a livelli elevati di mediatori dell'infiammazione così come la risposta immunitaria all'infezione da Citomegalovirus (CMV). Le attuali tecniche di riferimento per il rilevamento dei biomarcatori infiammatori si basano su immunosensori e su una reazione colorimetrica per quantificare l'analita specifico. Queste tecniche sono molto robuste e caratterizzate da elevata sensibilità e specificità; tuttavia, richiedono una quantità relativamente grande di campioni, attrezzature e personale specializzati, nonché l'uso di "labels" come cromofori o fluorofori. Questi svantaggi ne ostacolano l'implementazione al point-of-care (PoC) e come dispositivi portatili.

In questa tesi, proponiamo lo sviluppo di biosensori basati su transistor organici operanti in liquido (EGOT) come alternativa alle tecniche convenzionali. Gli EGOT si stanno imponendo come una delle architetture preferite per il rilevamento "label-free", grazie alla loro eccezionale capacità di amplificazione di piccoli segnali biologici, operando a bassi potenziali e venendo fabbricati con metodi a basso costo. Gli EGOTs sono dispositivi a tre terminali, comprendenti elettrodi di source (S) e drain (D) collegati dal semiconduttore organico (OSC) e un terzo elettrodo di gate (G), collegato all'OSC tramite una soluzione elettrolitica. L'elettrodo di G è accoppiato capacitivamente all'OSC, quindi una applicazione di potenziale al G porta alla formazione di un primo doppio strato dielettrico (EDL, dall'inglese electrical double layer) all'interfaccia gate/elettrolita, e alla formazione di un secondo EDL all'interfaccia semiconduttore organico/elettrolita elettrolita, modulando così la risposta elettriche del transistor.

Lo scopo di questa tesi è lo sviluppo di biosensori individuali basati su architettura EGOT per tre biomarcatori dell'inflammaging: Interleuchina 6, Interleuchina 1β, anticorpi anti-CMV, e proteina p-Tau_{181}. A tal fine, sono state esplorate due architetture EGOT: transistor elettrochimici organici (OECT) e transistor a effetto di campo modulati da elettrolita (EGOFET), i quali differiscono per la permeabilità dell'OSC alla penetrazione degli ioni. Per rendere gli EGOT sensibili ad un determinato marcatore, sono stati immobilizzati elementi di bioriconoscimento sull'elettrodo di G. Di conseguenza, l'evento di rilevazione all'interfaccia G/elettrolita viene trasdotto e amplificato in un cambiamento nella corrente di D. Durante

questa tesi sono state studiate, ottimizzate e validate diverse strategie di funzionalizzazione del G con tecniche complementari, come la spettroscopia di impedenza elettrochimica (EIS) e la risonanza plasmonica di superficie (SPR).

Abbiamo dimostrato la capacità di rilevazione di questi biomarcatori nell'intervallo fisio-patologico, e la possibilità di studiare la termodinamica dei processi di bioriconoscimento. Inoltre, l'integrazione di questi dispositivi con un sistema microfluidico ha consentito la quantificazione in tempo reale dei biomarcatori, dimostrando le potenzialità di questi dispositivi per un utilizzo PoC. Infine, è stata esplorata un'architettura alternativa.

Questo lavoro getta le basi per lo sviluppo di piattaforme di rilevamento multiplexing basate su architetture EGOT, nell’ottica di un utilizzo finale delle stesse al point-of-care.

KEYWORDS

Inflammaging

Organic Transistors

Biomarkers

Label-free sensor

Point-of-Care

Table of Contents

1 INTRODUCTION

The first part of this chapter describes Inflammaging and its association with the immune system. Here the possible biomarkers of healthy aging and their correlation with longevity or pathological aging are also described. The state-of-the-art techniques for biomarker detection are briefly reviewed. The second part is an introduction to organic bioelectronics, with a focus on EGOTs as a sensing platform. This section is partially based on the following review published in collaboration with Professor D. T. Simon's group, from the University of Linkoping: B. Burtscher, P. A. Manco Urbina, C. Diacci, S. Borghi, M. Pinti, A. Cossarizza, C. Salvarani, M. Berggren, F. Biscarini, D. T. Simon, C. A. Bortolotti," *Sensing Inflammation Biomarkers with Electrolyte-Gated Organic Electronic Transistors*", Adv. Healthc. Mater. 2021, 2100955.

1.1 INFLAMMAGING

Aging and age-related diseases share some common features that largely converge on inflammation. A comprehensive theory explaining the interconnections among aging, inflammation, and age-related disease is known as ‘‘inflammaging’’: this term, coined in 2000, refers to the chronic, low-grade proinflammatory status associated with aging.[1] Inflammaging biomarkers, which are considered within the “immune risk profile” (IRP), could predict physical and cognitive performance, as well as mortality in the elderly population.[2–4] This is because many age-related diseases, such as cardiovascular diseases, neurodegenerative diseases, obesity, metabolic syndrome, diabetes, cancer, and depression, all share a pathogenesis where chronic inflammation plays a crucial role. On the other hand, long-lived people, especially centenarians, seem to cope with chronic subclinical inflammation through an anti-inflammatory response, called ‘‘anti-inflammaging’’.[5]

1.1.1 Aging and the Immune System

Clearly, the immune system is closely related to aging. Originally, the focus was on changes in the adaptive immune system; however, in the last decades, evidence suggests that such aging-associated changes also occur in the innate immune system.

Regarding the effects on the adaptive immune response, it is a reflection of a lifetime exposure to what is called *stress* in a generic way, encompassing **antigenic**, metabolic, physicochemical, oxidative, among others kind of stress (**Figure 1.1**).[1,6] In a first stage, the stress can lead to a measured immune response; however, when prolonged over time, it can result in an excessive, uncontrolled and chronic inflammatory response.[7,8] With aging, the T cells tend to become more senescent, resulting in the release of a significant quantity of **pro-inflammatory cytokines** and mediators. Therefore, these mediators will activate other immune cells, but without an actual functional immunology role, they will lead to a change in T cells functions such as proliferation, migration, cytokine production, and pathogens killing.[9]

On the other hand, the innate immune response has been considered less sophisticated when compared to the adaptive immune response. This immune system has three main roles: avoiding and mitigating the damage stimuli, priming the adaptive immune system, and antigen presentation. Under physiological conditions, this response, like the adaptive response, maintains the functional homeostasis and the appropriate cellular response. However, in the elderly, the cells involved in this process have been found to be in a constant activated state, producing pro-inflammatory mediators, among them, pro-inflammatory cytokines.[9,10]

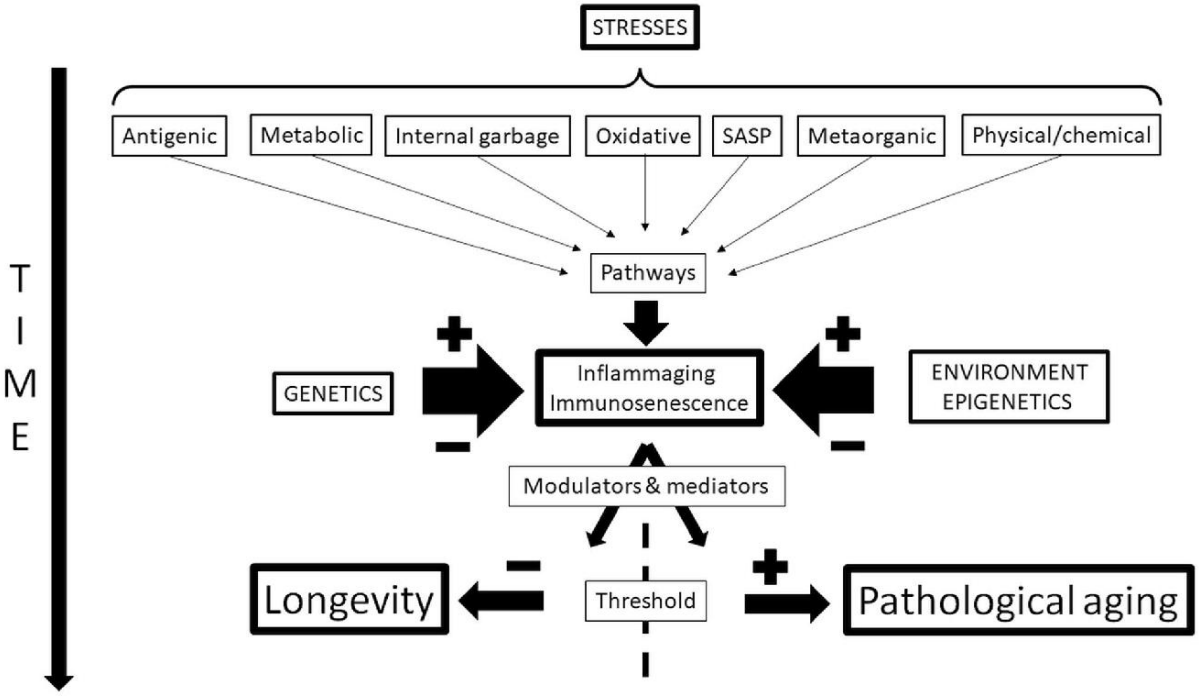

Figure 1.1. Conceptualization of Inflammaging, adapted from ref.[9] The stress includes the harmful stimuli that, through changes in the immune system lead to inflammaging, which in turn is affected by genetics and environmental factors. Depending on the levels of the resulting inflammation modulators and mediators this whole process can end up in longevity or pathological aging.

Viewing inflammaging as part of the aging process, one can consider changes in the immune system as adaptation or maladaptation. Therefore, in the former case, such changes help to fight the harmful agents in a less damaging way. Meanwhile, in the latter case, when the immune response fails to control the stress, it results in an unsuccessful aging, characterized by frailty, functional decline, and death.[5,9] This has been observed in several longitudinal studies, where subjects with extreme longevity presented a balance between anti- and pro-inflammatory cytokines as adaptive response to the stress, while subjects with reduce life expectancy presented more pro-inflammatory cytokines instead.[2,5,11,12]

1.1.2 Inflammaging Biomarkers

Although there is no specific biomarker for inflammaging, epidemiological evidence associates elevated levels of inflammatory mediators with this condition. Among those, the most commonly used are pro-inflammatory cytokines and acute phase proteins, e.g interleukin-6 (**IL-6**) and C-reactive protein (CRP). Longitudinal studies agree that IL-6 and CRP are good predictors of physical and cognitive performance, as well as of mortality in the elderly, even in subjects never diagnosed with age-related diseases.[2,13,14] These studies also raise attention to other proinflammatory cytokines such as Tumor Necrosis Factor α (TNF-α), which shows an age-related upregulation and correlation with early mortality,[5] and interleukin-1β (**IL-1β**),

which elevated levels have been associated with two specific clinical conditions, Congestive Heart Failure (CHF) and Angina.[15] Aging of the immune system is also characterized by the reduction in the frequency of naïve T cells, together with the increasing proportion of terminally differentiated, oligoclonal T lymphocytes. The increased proportion of this T cell subset in the elderly is the consequence of recurrent or chronic immune activation,[10] and in particular to the infection with persistent viruses, such as cytomegalovirus (**CMV**). The role of CMV infection in inflammaging is mainly related to recurrent activation of the immune system, leading to a vicious cycle of constant release of pro-inflammatory cytokines, which contributes to this chronic inflammatory state characteristic of inflammaging. Therefore, CMV infection can also be listed as a potential inflammaging biomarker.[16,17]

Another biomarker of interest, although it is not an inflammaging biomarker *per se*, would be the phosphorylated Tau protein (**p-Tau**). This protein is a good predictor of Alzheimer's Disease (AD), which is a common dementia pathology. The cause of AD has been associated with inflammation and oxidative stress, among others. Like in inflammaging, AD biomarkers are also considered to be part of the IRF, giving information about the physical and cognitive progression in the elderly.[18,19]

1.1.3 Biosensors for Proteins Detection and Quantification

Biosensors are devices for specific analyte detection, providing an output signal that correlates to analyte concentration. A biosensor consists of three main components: (i) a biorecognition element (such as an antibody, aptamer, or enzyme) that specifically detects and binds to the target analyte, (ii) a transducer that converts a physical or chemical change (like a binding event or enzymatic reaction) into a measurable signal (with common transducers including electrochemical, optical, piezoelectric, thermometric, and magnetic), and a read-out that processes and displays the signal.[20] In **Figure 1.2** we have a representation of a label-free biosensor.

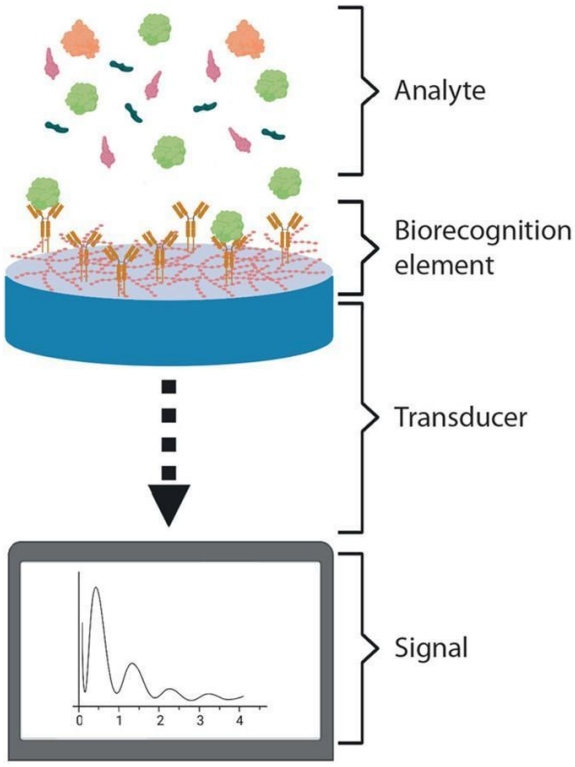

Figure 1.2. Schematics of a label-free biosensor with its three main components.[21]

The current gold standard techniques for inflammatory biomarkers detection are Enzyme-linked immunosorbent assay (ELISA) and Flow cytometry-based technologies. Both techniques rely on antibody-antigen interaction, and colorimetric reaction to quantitatively determine the specific analyte.[21] These techniques are very robust and are characterized by high sensitivity and specificity; however, they require a relatively large amount of sample, specialized equipment and personnel, as well as labelling. These disadvantages hamper their implementation at the point of care and as portable devices.

We recently reviewed the development of label-free biosensors for the detection of proteins, more specifically cytokines biosensors, classified based on their transducer principle. Optical biosensors have proved to be very sensitive, and recent efforts have allowed its implementation into microfluidics and miniaturization; however, the requirement for bulky instrumentation for the read-out is still a limitation for its application in the clinical practice.[22–24] Piezoelectric-based biosensors on the other hand have achieved sensing in low concentration, reaching a LOD around 1pg mL^{-1}; however, they require relatively long times for detection, and the improved sensitivity was achieved by using magnetic beads as labels, which then entail all the complications associated with label-based sensing.[25,26] Electrochemical biosensors exhibit low LOD, span its operability across several orders of magnitude, including relevant concentration range, and have shown good performance in complex solution, including

biological samples.[27–30] Field Effect Transistors (FETs) have been used for real-time detection of cytokines and the study of binding kinetics, allowing for protein detection even in the fM range.[31,32] All this biosensors present excellent performances, but their translation from the laboratory-scale research to the Point-of-Care (PoC) is yet to be achieved.

1.2 ORGANIC BIOELECTRONICS

Organic bioelectronics is the field of research that focuses on the development of electronic devices that work as translators between the biological signal or function and the human-made electronic processing systems, bridging the signalling gap between the biology and the technology world. For this purpose, organic devices employ organic molecules or polymers as the communication interface.[33] These materials exhibit electrical and/or ionic conductivity, unlike their inorganic counterparts. Additionally, they feature the following advantages: low temperature processability, compatibility with flexible substrates, large-scale manufacturing, and easy microfabrication methods.[34]

One can find commercially available devices based on organic electronics. This is, for example, the case of Organic Light Emitted Diodes (OLEDs). However, most of the technology based on organic bioelectronics remains at the forefront of technology-based innovative research. Within the organic electronics field,, organic transistors have been studied for their high electrical performances and their potential as innovative sensing platforms.[35] Taking this into consideration, it is not surprising that organic transistors have emerged as an alternative to the conventional silicon-based transistors, being characterized by low-cost production, flexibility, biocompatibility, and the possibility to modify *ad hoc* their active material with respect to the specific application.[36]

1.2.1 Electrolyte-Gated Organic Transistors

Typically, they are three terminal devices, composed by a drain electrode (D) and a source (S) electrode interconnected via an organic semiconductor (OSC) material, which in turn is connected to the third electrode, namely gate (G), through a solid dielectric material in the case of Organic Field Effect Transistors (OFETs), and an electrolyte solution in the case of Electrolyte-Gated Organic Transistors (EGOTs).[37,38]

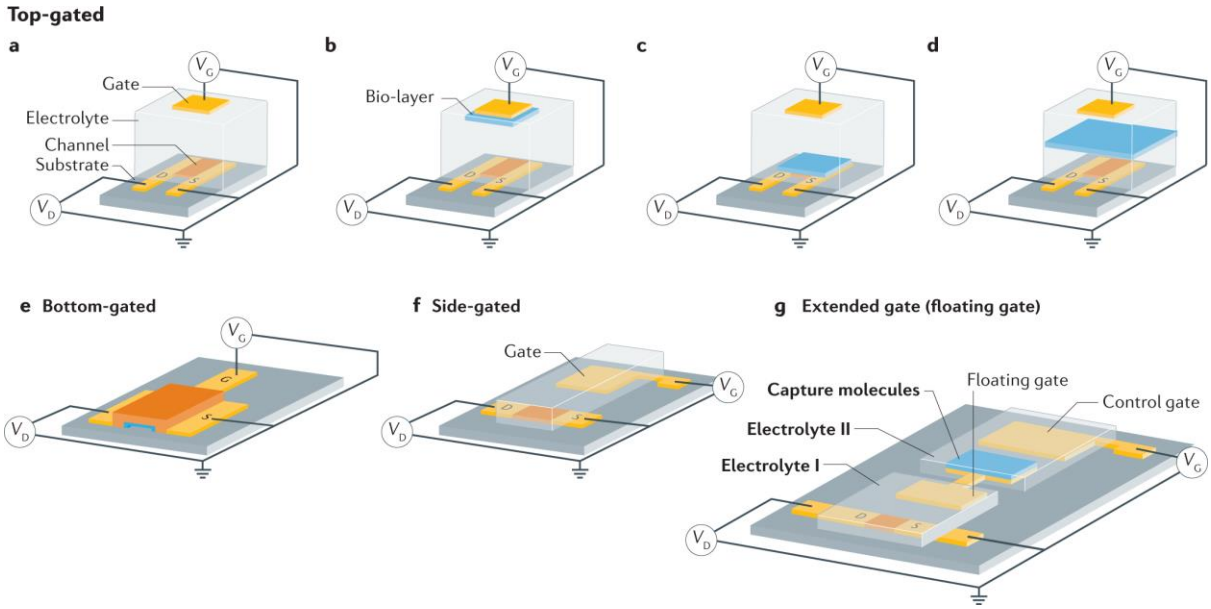

Figure 1.3. Different configurations of EGOT, highlighting the classical top-gate (a-d), the bottom-gated (e,not discussed in this work), side-gated (f), and the Extended-Gate EGOT (g).[38]

What distinguishes EGOTs from the other transistor architectures, such as FETs or OFETs, is their operability in liquid environment. and hence allowing to operate them directly in biological media as electrolyte. To confer sensitivity with respect to a target molecule, one of the interfaces, either the gate/electrolyte or the electrolyte/OSC must be decorated with biorecognition elements on the surface (e.g. antibodies, DNA/RNA aptamers, enzymes). EGOT devices can be fabricated with different configurations of the gate electrode with respect to the semiconducting channel as shown in **Figure 1.3**. The already presented top-gated configuration (**Figure 1.3 a-d**) is the most common architecture used for the fabrication of highly sensitive biosensors. However, the side-gated configuration(**Figure 1.3 f**), where gate and channel are on the same plane has also proved to be an excellent choice, especially for certain applications (i.e. neuromorphics).[39,40] Recently, a more developed configuration has been proposed, named Extended-Gate EGOT (EG-EGOT) (**Figure 1.3 g**), which features an extended gate with two areas bridged by a solid state conductor, one (G) in contact with the channel material via the first electrolyte, and the other one (EG) in contact with a control gate (CG) electrode via the second electrolyte. In this case, the EG is the sensing surface, being the one exposed to the sample to be tested (e.g. blood, plasma,). This was proposed to prevent the OSC exposure to complex media and avoid any effects on the device performance.[41,42]

EGOTs can be classified as Electrolyte-Gated Organic Field Effect Transistors (EGOFETs), when the OSC is impermeable to ions penetration, or as Organic Electrochemical Transistors

(OECTs), when ions can penetrate the whole OSC.[37] **Figure 1.4** displays both architectures, showing an OECT in the left panel and an EGOFET in the right panel.

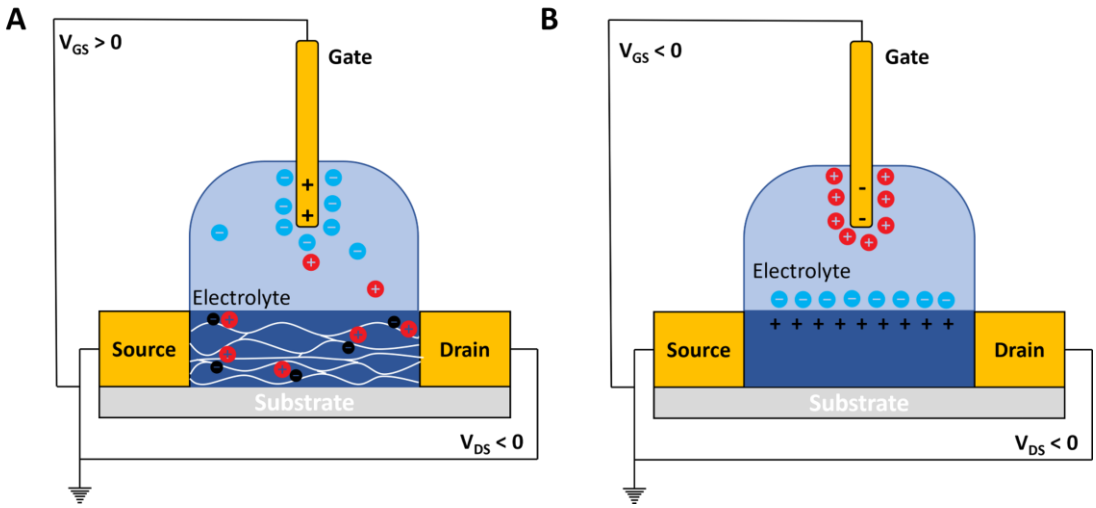

Figure 1.4. OECT (left) and EGOFET (right) architectures with their electrical connections. Ions are represented as blue circles for anions, and red circles for cations, while holes (positive charge carriers) are represented as "+".

1.2.1.1 EGOFET working principle

EGOFETs can be fabricated using p-type or n-type semiconductor materials, which differ from the type of charge carriers that are mainly responsible for the current flowing in the device channel; in p-type OSC, the charge carriers are positive, holes, in n-type OSC, the charge carries are negative, electrons. **Figure 1.4 B** depicts a p-type EGOFET device, where a negative potential is applied to the gate electrode (V_{GS}) and to the drain electrode (V_{DS}), both using as reference the source electrode, which is typically grounded. The application of negative V_{GS} causes the migration of cations to the gate/electrolyte interface, and in consequence a migration of anions to electrolyte/OSC interface, resulting in an electrical double layer (EDL) at both interfaces. The EDL at the electrolyte/OSC interface is formed due to the injection of free charge carriers (holes) present in the OSC to compensate for the negative charges at the gate/electrolyte interface, rendering the channel conductive. Finally, upon the application of a negative V_{DS} we obtain the current flow (I_{DS}).

Here resides one of the main characteristics of these devices. Small changes in the gate potential (V_{GS}) are transduced into large changes in drain current (I_{DS}) through an ionic-electronic modulation due to the device operability in electrolyte. When the applied V_{GS} is positive, anions flow from the bulk of the electrolyte to the gate/electrolyte interface, forming a very compact layer, namely EDL. This EDL acts like a capacitor, where the capacitance is inversely

proportional to the thickness of the dielectric separating the charges. The thickness of the EDL is remarkably small, this leads to a very high capacitance (a few tens of μF cm^{-2}) in EGOFETs at the gate/electrolyte interface, thus allowing EGOTs operation at very low V_{GS} (<1 V). The importance of operating at such small voltage is two-fold: (i) working in "safe" potential window avoids redox processes involving the solvent, typically between 0 and 0.5 V, thus preventing undesired faradaic processes; (ii) a low applied potential is crucial when interfacing with biolayers in order to not damage their integrity.[36–38]

The EGOFET detection mechanism relies on changes of the EDL at the interface between the electrolyte and the surface (gate electrode or OSC) bearing the biorecognition unit (e.g., antibody, aptamer): upon binding of the analyte, the surface electrochemical potential and/or the EDL capacitance can be affected. Therefore, any small biological signal will be transduced and amplified into large changes in current (I_{DS})

1.2.1.2 OECT working principle

OECTs operate by V_{GS}-driven changes in the bulk of the ion-permeable OSC channel. Like in the case of EGOFETs, V_{GS} causes the formation of EDL at the polarizable gate/electrolyte interface and drives ions from the electrolyte into the permeable polymer, thereby modulating its conductivity by (de)doping and thus affecting the I_{DS}. **Figure 1.4 A** shows an example of a p-type OECT device, based on the most widely used polymer poly(3,4-ethylenedioxythiophene) doped with the polyanion polystyrene sulfonate (PEDOT:PSS). OECTs with PEDOT:PSS as OSC work in depletion mode, i.e., increasing V_{GS} depletes the channel of mobile charges and decreases I_{DS}. On the contrary, OECTs working in accumulation mode increase the number of charge carriers as a consequence of an increased ionic doping;, hence, increasing V_{GS} increases the density of mobile charges in the channel and thereby increases I_{DS}.

OECTs are also typically operated at sub-1V potentials. Additionally, OECTs exhibit very high transconductance compared to EGOFETs due to the coupling between ionic and electronic charges across the whole OSC volume. However, this also limits the response time.[43]

A widely adopted model to account for the detection mechanism of an OECT based biosensors in faradic mode was proposed by Bernards and Malliaras.[44] The model relies on potential changes at the electrode/electrolyte interface, due to faradic reactions, thus shifting the effective gate voltage and the current in the channel. Although the Bernards model proposed in 2008 is a good starting point, more recent studies suggest that some additional factors should

be taken into consideration. A more complete model should include the contact resistance effects, the influence of disorder on hole transport in the channel, and/or charge density-dependent conductivity.[43]

OECTs have largely been preferred as amperometric biosensors operated in the faradic regime. In the few examples of OECTs biosensors in the non-faradic mode, the transduction mechanism was ascribed to charge variations at the surface following analyte binding[45] or to limited access of ions to the OSC resulting from their interaction with a peptide-containing membrane.[46]

1.2.2 EGOT Applications

This technology has been extensively explored in the last decades for a wide variety of applications (**Figure 1.5**). EGOTs have proved to be an excellent strategy for ***two-dimensional and three-dimensional cell culture monitoring***. The trend in cellular biology goes towards growing cell culture in three dimensions, more closely mimicking the *in vivo* cell environment, to this end, bendable transistor arrays have promising applications, covering the whole surface of the tissue.[47] Another interesting approach is the use of conductive polymers as scaffolding electrodes to integrate, or even mimic, the tissue of study.[48,49] EGTs, especially OECTs have been tested for its application in ***Electrophysiology***. Since these devices have to be in direct contact with the body, the conformability of the device into the substrate is of great importance.[50] To this end, conjugated polymers, such as PEDOT:PSS haven used due to their flexibility, stretchability, high transconductance for a better signal amplification, and for its easily engineered tunability, improving both neuron recording and stimulation.[51–54] There are still many possibilities regarding the application of EGOTs in this field, such as polymer integration in textiles,[55] tattoo electrodes,[56] recording epileptic seizures,[57] mapping of the heart and brain,[52,53] and stimulation of cortical neurons.[54] EGOTs have been also used in ***Synaptic and neuromorphic bio-interfaces***. High-capacitance polarizable gate electrodes can transform OECTs into a capacitor, enabling the demonstration of a volatile artificial synapse for neuromorphic computing.[38] EGOTs can also mimic the common electrochemical environment in biological neural networks.[40] Finally, the integration of neuromorphic devices with living matter is a promising research direction. The EGT-based synaptic device is useful for neuromorphic signal processing in e-skin ***prosthetic and robotic applications***. This is a very exciting and promising technological field; by combining resistive pressure sensors with organic transistor ring oscillators, the device can mimic the synapses of biological afferent nerves and combine information from multiple inputs.[58–60] It allows for fast processing of a

large amount of data from multiple sensors, enabling immediate decision-making based on detected information.

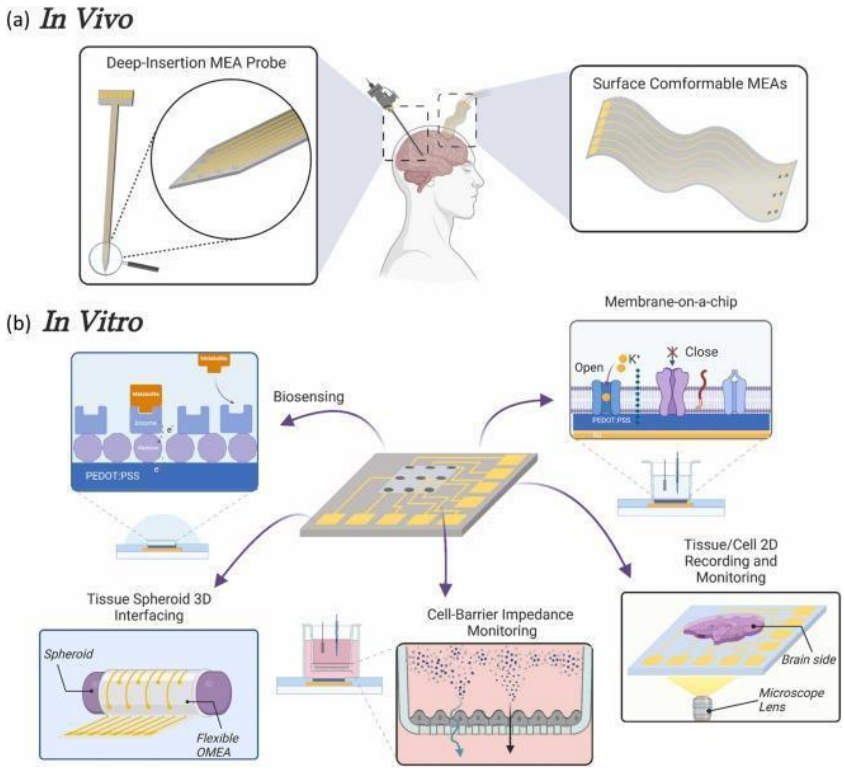

Figure 1.5. EGOTs application, classified as in vivo or in vitro application.[61] Here are depicted examples of EGOT application in the 2D or 3D cell monitoring (in vitro), and in Electrophysiology (in vivo).

1.2.2.1 EGOT-based biosensors

Compared to other detection technologies, organic transistors represent an optimal biosensor platform due to their unique features. Organic transistors are based on OSCs, which can be stable in liquid/aqueous environments, including physiological media and bodily fluids.[43] They operate at low voltages (0.1–1 V) and therefore require relatively low power (micro- to mJ).[62] Moreover, they can be fabricated onto inexpensive and disposable substrates such as paper[63] or plastic[64] and with low-cost fabrication techniques (spin-coating, spray coating, screen printing, and inkjet-printing), facilitating scaling up of their manufacturing. Organic transistors can be miniaturized and integrated with microfluidics, making portable bioelectronic devices relatively straightforward to design and prototype. Interestingly, their fundamental operational principle relies on ion motion, which is also the physiological mechanism for communication, making them effectively suitable for bridging electronics to biology.[33]

In the last decade, EGOTs, both in OECT and EGOFET configurations, have been extensively used as biosensors. Such applications have been previously reviewed.[33,37,43,65,66] Table 1

reports few examples of EGOT-based biosensors for sensing inflammatory biomarkers or soluble proteins of comparable size.

Table 1.1. A selection of OECT and EGOFET protein sensing demonstrations and their various mechanisms and materials.

Target molecule	Functionalized interface	Sensing unit	Channel material
	OECT for protein detection		
Prostate specific agent (PSA)	Channel	Antibody/AuNPs	PEDOT:PSS
Human epidermal growth factor receptor 2 (HER2)	Gate electrode	Nanoprobes	PEDOT:PSS
Immunoglobulin-G (IgG)	Gate electrode	Antibody	PEDOT:PSS
Interleukin 6 (IL6)	Gate electrode	Antibody	PEDOT:PSS
L-histidine, L-tryptophan	Gate electrode	MIPs	PEDOT:PSS
β-Amyloids	Channel	Nanoporous membrane	PEDOT:PSS
Spike proteins (SARS)	Gate electrode	Nanobody	p(g0T2-g6T2)
Caspase-3	Gate electrode	Peptide	PEDOT:PSS
	EGOFET for protein detection		
Interleukin 4 (IL-4)	Gate electrode	Antibody	Pentacene
Interleukin 6 (IL-6)	Gate electrode	Antibody/aptamer	Pentacene
Tumor necrosis factor-α (TNF-α)	Gate electrode	Antibody	Pentacene
Tumor necrosis factor-α (TNF-α)	Gate electrode	Aptamer	Pentacene
C-reactive protein (CRP)	Gate electrode/SAM	Antibody	P3HT
C-reactive protein (CRP)	Channel	Antibody	P3HT
Procalcitonin (PCT)	Channel	Antibody	P3HT
Vascular endothelial growth factor (VEGF)	Gate electrode	Aptamer hydrogel	DPP-DTT
Ricin	Floating gate	Aptamer	P3HT

EGOT-based biosensors have proved to be a successful tool for protein detection in solution. Our group has reported the application of these devices for the detection of inflammatory biomarkers,[67–70] but also of cancer biomarkers,[71] reaching LOD in the sub-pM range. Taking all this together, EGOTs feature optimal LOD, ease of manufacture, with the possibility of large-scale manufacturing, and ease of integration with other (bio)electronic systems. Hence, these devices represent a promising sensing platform, as an alternative to the current standard detection methods, for implementation at the PoC.

1.3 AIM of the Thesis

The main goal of this thesis was the development of EGOT-based biosensors for the detection of aging biomarkers. As previously described, there is no such thing as a single biomarker for healthy ageing. Rather, the levels of different biomolecules, especially (though not only) pro- and anti-inflammatory cytokines, should be monitored to obtain a comprehensive profiling of the subject. As a consequence, although we here focused on the demonstration of individual biosensors of ageing, the final goal would be to implement such sensors in a multiplexer for simultaneous detection of such analytes.

Therefore, in Chapters 3 to 6, four EGOT-based biosensors, namely towards IL-6, IL-1β, anti-CMV antidoy, and p-Tau181, will be described. For each biosensor, the fabrication is described along with the electrical characterization of the devices. The response to the target analytes was always quantified by construction of the corresponding dose curve, and the robustness of each biosensor was always assessed in terms of selectivity by performing control experiments. Besides their potential as analytical tools, the devices developed within this thesis also allowed us to investigate both the thermodynamics and kinetics of the recognition processes between two biomolecules, one bound to the surface (typically, though not always, an antibody) and the corresponding partner diffusing from the solution and binding to its probe at the electrode/electrolyte interface. The possibility to use these ultra-sensitive and highly versatile devices as tools for investigating fundamental aspects of biorecognition is crucial for both complementing other state-of-the-art techniques to determine affinity and therefore specificity of biomolecules, as well as to elucidate the molecular determinants to the response of widely-used immunosensors.

Also, one of the main features of this work was the focus on the different functionalization strategies that can be employed to endow EGOTs with sensing capabilities, thanks to the use of a portfolio of techniques, spanning from electrochemical to optical methods, which allowed to monitor and compare functionalization protocols for optimal operation of the devices as biosensors.

1.4 REFERENCES

[1] C. Franceschi, M. Bonafè, S. Valensin, F. Olivieri, M. De Luca, E. Ottaviani, G. De Benedictis, *Ann. N. Y. Acad. Sci.* **2000**, *908*, 244.

[2] M. Cesari, B. W. J. H. Penninx, M. Pahor, F. Lauretani, A. M. Corsi, G. R. Williams, J. M. Guralnik, L. Ferrucci, *Journals Gerontol. - Ser. A Biol. Sci. Med. Sci.* **2004**, *59*, 242.

[3] U. Fagiol, A. Cossarizza, C. S. Santacaterina, C. Franceschy, *Cytokine Prod.* **1992**, 490.

[4] G. Pawelec, S. Gupta, *Front. Immunol.* **2019**, *10*, 1.

[5] P. L. Minciullo, A. Catalano, G. Mandraffino, M. Casciaro, A. Crucitti, G. Maltese, N. Morabito, A. Lasco, S. Gangemi, G. Basile, *Arch. Immunol. Ther. Exp. (Warsz).* **2016**, *64*, 111.

[6] A. Vitlic, J. M. Lord, A. C. Phillips, *Age (Dordr).* **2014**, *36*, 1169.

[7] E. L. Goldberg, A. C. Shaw, R. R. Montgomery, *Interdiscip. Top. Gerontol. Geriatr.* **2020**, *43*, 1.

[8] C. Franceschi, P. Garagnani, G. Vitale, M. Capri, S. Salvioli, *Trends Endocrinol. Metab.* **2017**, *28*, 199.

[9] T. Fulop, A. Larbi, G. Pawelec, A. Khalil, A. A. Cohen, K. Hirokawa, J. M. Witkowski, C. Franceschi, *Clin. Rev. Allergy Immunol.* **2023**, *64*, 109.

[10] M. Pinti, V. Appay, J. Campisi, D. Frasca, T. Fülöp, D. Sauce, A. Larbi, B. Weinberger, A. Cossarizza, *Eur. J. Immunol.* **2016**, *46*, 2286.

[11] D. Baylis, D. B. Bartlett, H. P. Patel, H. C. Roberts, *Longev. Heal.* **2013**, *2*, 1.

[12] C. Franceschi, D. Monti, P. Sansoni, A. Cossarizza, *Immunol. Today* **1995**, *16*, 12.

[13] R. Varadhan, W. Yao, A. Matteini, B. A. Beamer, Q. L. Xue, H. Yang, B. Manwani, A. Reiner, N. Jenny, N. Parekh, M. Daniele Fallin, A. Newman, K. Bandeen-Roche, R. Tracy, L. Ferrucci, J. Walston, *Journals Gerontol. - Ser. A Biol. Sci. Med. Sci.* **2014**, *69 A*, 165.

[14] M. Puzianowska-Kuźnicka, M. Owczarz, K. Wieczorowska-Tobis, P. Nadrowski, J. Chudek, P. Slusarczyk, A. Skalska, M. Jonas, E. Franek, M. Mossakowska, *Immun. Ageing* **2016**, *13*, 1.

[15] A. Di Iorio, L. Ferrucci, E. Sparvieri, A. Cherubini, S. Volpato, A. Corsi, M. Bonafè, C. Franceschi, G. Abate, R. Paganelli, *Cytokine* **2003**, *22*, 198.

[16] A. E. Aiello, Y. Chiu, D. Frasca, *GeroScience* **2017**, *39*, DOI 10.1007/s11357-017-9983-9.

[17] L. Papagno, C. A. Spina, A. Marchant, M. Salio, N. Rufer, S. Little, T. Dong, G. Chesney, A. Waters, P. Easterbrook, P. R. Dunbar, D. Shepherd, V. Cerundolo, V. Emery, P. Griffiths, C. Conlon, A. J. McMichael, D. D. Richman, S. L. Rowland-Jones, V. Appay, *PLoS Biol.* **2004**, *2*, DOI 10.1371/journal.pbio.0020020.

[18] O. Sheppard, M. Coleman, in *Azheimer's Dis. Drug Discov.* (Ed.: X. Huang), **2020**, pp. 1–22.

[19] S. J. Fuller, H. R. Sohrabi, K. G. Goozee, A. Sankaranarayanan, R. N. Martins, *Neurodegener. Alzheimer's Dis. Role Diabetes, Genet. Horm. Lifestyle* **2019**, 9.

[20] B. Burtscher, P. A. Manco Urbina, C. Diacci, S. Borghi, M. Pinti, A. Cossarizza, C. Salvarani, M. Berggren, F. Biscarini, D. T. Simon, C. A. Bortolotti, *Adv. Healthc. Mater.* **2021**, *2100955*, DOI 10.1002/adhm.202100955.

[21] W. De Jager, H. Te Velthuis, B. J. Prakken, W. Kuis, G. T. Rijkers, *Clin. Diagn. Lab. Immunol.* **2003**, *10*, 133.

[22] M. C. Estevez, M. A. Otte, B. Sepulveda, L. M. Lechuga, *Anal. Chim. Acta* **2014**, *806*, 55.

[23] X. Li, M. Soler, C. I. Özdemir, A. Belushkin, F. Yesilköy, H. Altug, *Lab Chip* **2017**, *17*, 2208.

[24] S. Ghosh, D. Datta, S. Chaudhry, M. Dutta, M. A. Stroscio, *IEEE Trans. Nanobioscience* **2018**, *17*, 417.

[25] Y. Kyoung Bahk, H. H. Kim, D.-S. Park, S.-C. Chang, J. S. Go, *Korean Chem. Soc* **2011**, *32*, 4215.

[26] M. Pohanka, *Talanta* **2018**, *178*, 970.

[27] L. S. S. Kumar, X. Wang, J. Hagen, R. Naik, I. Papautsky, J. Heikenfeld, *Anal. Methods* **2016**, *8*, 3440.

[28] R. Sharma, S. E. Deacon, D. Nowak, S. E. George, M. P. Szymonik, A. A. S. Tang, D. C. Tomlinson, A. G. Davies, M. J. McPherson, C. Wälti, *Biosens. Bioelectron.* **2016**,

80, 607.

[29] E. B. Aydın, M. K. Sezgintürk, *Anal. Biochem.* **2018**, *554*, 44.

[30] S. Verma, A. Singh, A. Shukla, J. Kaswan, K. Arora, J. Ramirez-Vick, P. Singh, S. P. Singh, *ACS Appl. Mater. Interfaces* **2017**, *9*, 27462.

[31] V. A. Pham Ba, Y. M. Han, Y. Cho, T. Kim, B. Y. Lee, J. S. Kim, S. Hong, *ACS Appl. Mater. Interfaces* **2018**, *10*, 17100.

[32] H. Nam, B. R. Oh, P. Chen, M. Chen, S. Wi, W. Wan, K. Kurabayashi, X. Liang, *Sci. Reports 2015 51* **2015**, *5*, 1.

[33] D. T. Simon, E. O. Gabrielsson, K. Tybrandt, M. Berggren, *Chem. Rev.* **2016**, *116*, 13009.

[34] J. Rivnay, R. M. Owens, G. G. Malliaras, *Chem. Mater.* **2014**, *26*, 679.

[35] S. Lai, A. Spanu, P. Cosseddu, A. Bonfiglio, in *Org. Bioelectron. Life Sci. Healthc.*, **2019**.

[36] L. Kergoat, B. Piro, M. Berggren, *Anal. Bioanal. Chem.* **2012**, *402*, 1813.

[37] D. Wang, V. Noël, B. Piro, *Electron.* **2016**, *5*, DOI 10.3390/electronics5010009.

[38] F. Torricelli, D. Z. Adrahtas, Z. Bao, M. Berggren, F. Biscarini, A. Bonfiglio, C. A. Bortolotti, C. D. Frisbie, E. Macchia, G. G. Malliaras, I. McCulloch, M. Moser, T.-Q. Nguyen, R. M. Owens, A. Salleo, A. Spanu, L. Torsi, *Nat. Rev. Methods Prim.* **2021**, *1*, DOI 10.1038/s43586-021-00065-8.

[39] D. A. Koutsouras, T. Prodromakis, G. G. Malliaras, P. W. M. Blom, P. Gkoupidenis, *Adv. Intell. Syst.* **2019**, *1*, 1900013.

[40] P. Gkoupidenis, D. A. Koutsouras, G. G. Malliaras, *Nat. Commun.* **2017**, *8*, 1.

[41] S. P. White, K. D. Dorfman, C. D. Frisbie, *J. Phys. Chem.* **2016**, *120*, 108.

[42] M. S. Thomas, S. P. White, K. D. Dorfman, C. D. Frisbie, *J. Phys. Chem. Lett.* **2018**, *9*, 1335.

[43] J. Rivnay, S. Inal, A. Salleo, R. M. Owens, M. Berggren, G. G. Malliaras, *Nat. Rev. Mater.* **2018**, *3*, DOI 10.1038/natrevmats.2017.86.

[44] D. A. Bernards, D. J. MacAya, M. Nikolou, J. A. Defranco, S. Takamatsu, G. G. Malliaras, *J. Mater. Chem.* **2007**, *18*, 116.

[45] D. J. Kim, N. E. Lee, J. S. Park, I. J. Park, J. G. Kim, H. J. Cho, *Biosens. Bioelectron.* **2010**, *25*, 2477.

[46] S. Wustoni, S. Wang, J. R. Alvarez, T. C. Hidalgo, S. P. Nunes, S. Inal, *Biosens. Bioelectron.* **2019**, *143*, DOI 10.1016/J.BIOS.2019.111561.

[47] A. Kalmykov, C. Huang, J. Bliley, D. Shiwarski, J. Tashman, A. Abdullah, S. K. Rastogi, S. Shukla, E. Mataev, A. W. Feinberg, K. Jimmy Hsia, T. Cohen-Karni, *Sci. Adv.* **2019**, *5*, 729.

[48] D. Iandolo, J. Sheard, G. Karavitas Levy, C. Pitsalidis, E. Tan, A. Dennis, J. S. Kim, A. E. Markaki, D. Widera, R. M. Owens, *MRS Commun.* **2020**, *10*, 179.

[49] C. M. Moysidou, C. Pitsalidis, M. Al-Sharabi, A. M. Withers, J. A. Zeitler, R. M. Owens, *Adv. Biol.* **2021**, *5*, 2000306.

[50] A. Campana, T. Cramer, D. T. Simon, M. Berggren, F. Biscarini, *Adv. Mater.* **2014**, *26*, 3874.

[51] D. Khodagholy, J. Rivnay, M. Sessolo, M. Gurfinkel, P. Leleux, L. H. Jimison, E. Stavrinidou, T. Herve, S. Sanaur, R. M. Owens, G. G. Malliaras, *Nat. Commun.* **2013**, *4*, 1.

[52] W. Lee, D. Kim, N. Matsuhisa, M. Nagase, M. Sekino, G. G. Malliaras, T. Yokota, T. Someya, *Proc. Natl. Acad. Sci. U. S. A.* **2017**, *114*, 10554.

[53] W. Lee, S. Kobayashi, M. Nagase, Y. Jimbo, I. Saito, Y. Inoue, T. Yambe, M. Sekino, G. G. Malliaras, T. Yokota, M. Tanaka, T. Someya, *Sci. Adv.* **2018**, *4*, DOI 10.1126/SCIADV.AAU2426/SUPPL_FILE/AAU2426_SM.PDF.

[54] A. Williamson, M. Ferro, P. Leleux, E. Ismailova, A. Kaszas, T. Doublet, P. Quilichini, J. Rivnay, B. Rõzsa, G. Katona, C. Bernard, G. G. Malliaras, *Adv. Mater.* **2015**, *27*, 4405.

[55] S. J. Kim, H. Kim, J. Ahn, D. K. Hwang, H. Ju, M. C. Park, H. Yang, S. H. Kim, H. W. Jang, J. A. Lim, *Adv. Mater.* **2019**, *31*, 1900564.

[56] A. Mascia, R. Collu, A. Spanu, M. Fraschini, M. Barbaro, P. Cosseddu, *Sensors* **2023**, *23*, 1.

[57] G. Buzsáki, *Rhythms of the Brain*, Oxford University Press, **2011**.

[58] B. C. K. Tee, A. Chortos, A. Berndt, A. K. Nguyen, A. Tom, A. McGuire, Z. C. Lin,

K. Tien, W. G. Bae, H. Wang, P. Mei, H. H. Chou, B. Cui, K. Deisseroth, T. N. Ng, Z. Bao, *Science (80-.).* **2015**, *350*, 313.

[59] Y. Kim, A. Chortos, W. Xu, Y. Liu, J. Y. Oh, D. Son, J. Kang, A. M. Foudeh, C. Zhu, Y. Lee, S. Niu, J. Liu, R. Pfattner, Z. Bao, T. W. Lee, *Science* **2018**, *360*, 998.

[60] F. Bengtsson, R. Brasselet, R. S. Johansson, A. Arleo, H. Jörntell, *PLoS One* **2013**, *8*, e56630.

[61] Z. Lu, A. Pavia, A. Savva, L. Kergoat, R. M. Owens, *Mater. Sci. Eng. R Reports* **2023**, *153*, DOI 10.1016/j.mser.2023.100726.

[62] Y. Duan, B. Zhang, S. Zou, C. Fang, Q. Wang, Y. Shi, Y. Li, *J. Phys. Mater.* **2020**, *3*, 014009.

[63] M. K. Akbari, S. Zhuiykov, S. U. Zschieschang, H. Klauk, U. Zschieschang, *J. Mater. Chem. C* **2019**, *7*, 5522.

[64] T. Someya, Z. Bao, G. G. Malliaras, *Nat. 2016 5407633* **2016**, *540*, 379.

[65] X. Strakosas, M. Bongo, R. M. Owens, *J. Appl. Polym. Sci.* **2015**, *132*, 41735.

[66] R. A. Picca, K. Manoli, E. Macchia, L. Sarcina, C. Di Franco, N. Cioffi, D. Blasi, R. Österbacka, F. Torricelli, G. Scamarcio, L. Torsi, *Adv. Funct. Mater.* **2020**, *30*, 1904513.

[67] V. Parkula, M. Berto, C. Diacci, B. Patrahau, M. Di Lauro, A. Kovtun, A. Liscio, M. Sensi, P. Samorì, P. Greco, C. A. Bortolotti, F. Biscarini, *Anal. Chem.* **2020**, *92*, 9330.

[68] M. Berto, C. Diacci, R. D'Agata, M. Pinti, E. Bianchini, M. Di Lauro, S. Casalini, A. Cossarizza, M. Berggren, D. Simon, G. Spoto, F. Biscarini, C. A. Bortolotti, *Adv. Biosyst.* **2018**, *2*, 1700072.

[69] C. Diacci, M. Berto, M. Di Lauro, E. Bianchini, M. Pinti, D. T. Simon, F. Biscarini, C. A. Bortolotti, *Biointerphases* **2017**, *12*, DOI 10.1116/1.4997760/124302.

[70] P. A. Manco Urbina, M. Berto, P. Greco, M. Sensi, S. Borghi, M. Borsari, C. A. Bortolotti, F. Biscarini, *J. Mater. Chem. C* **2021**, *9*, 10965.

[71] M. Selvaraj, P. Greco, M. Sensi, G. D. Saygin, N. Bellassai, R. D'Agata, G. Spoto, F. Biscarini, *Biosens. Bioelectron.* **2021**, *182*, DOI 10.1016/J.BIOS.2021.113144.

2 METHODS

In this chapter all the materials and techniques employed throughout the course of this thesis are described. All the steps for the fabrication of the devices are explained in detail, encompassing the substrates, organic semiconductor materials, and its deposition techniques, alongside the different gate functionalization strategies explored. Furthermore, this chapter expounds upon the characterization techniques employed in conjunction with an analytical evaluation of the measurement parameters.

2.1 EGOT DEVELOPMENT

2.1.1 Test Pattern

In this section, the substrates, called Test Patterns (TPs), used for the Electrolyte Gated Transistor (EGT) development, both commercially available and those designed and fabricated in the laboratory, as well as the cleaning procedure for each substrate will be described. The TPs were then used for different sensing purposes (Chapters 3 to 5) and integrated into microfluidics (Chapter 4).

2.1.1.1 Quartz

Interdigitated gold electrodes on quartz substrate were purchased from "Fondazione Bruno Kessler"-FBK, Trento, Italy). They were fabricated by photolithography and lift-off technique, featuring four interdigitated source (S) and drain (D) gold electrodes of 50 nm thickness, with a few nm of chromium adhesive layer. The final substrate was of 1cm^2 total area, less than 2nm electrode roughness, and a channel width-to-length ratio (W/L) of 2000 and 50 (**Figure 2.1**, right panel).

Before the organic semiconductor (OSC) deposition, TPs were i) rinsed with acetone to remove the photoresist layer and ii) gently dried with nitrogen flow, then iii) they were washed in hot acetone (70°C) for 10 minutes, and again iv) gently dried with nitrogen flow; a final cleaning step was performed by v) washing it in piranha solution (H_2SO_4:H_2O_2 1:1) for one minute at 150°C, followed by vi) abundant rinsing with water and vii) drying with nitrogen flow.

2.1.1.2 Glass

ED-IDE1-Au interdigitated gold electrodes on a glass substrate were purchased from Micrux Technology. These TPs feature a diameter channel (electrochemical cell) of 3.5 nm, with an adhesive layer of titanium of 50 μm and a gold layer of 150 μm. The interdigitated D and S electrodes and the gap between electrodes are 10 μm, with 490 mm channel width, resulting in W/L = 49 000 (**Figure 2.1**, left panel).

The substrates were cleaned following a standard protocol before the OSC deposition. i) sonication for 15 minutes in 1% Hellmanex II aqueous solution and rinse with water, ii) sonication for 15 minutes in water and rinse with water, iii) sonication for 15 minutes in ethanol, and a final rinse with water and ethanol and dry with N_2.

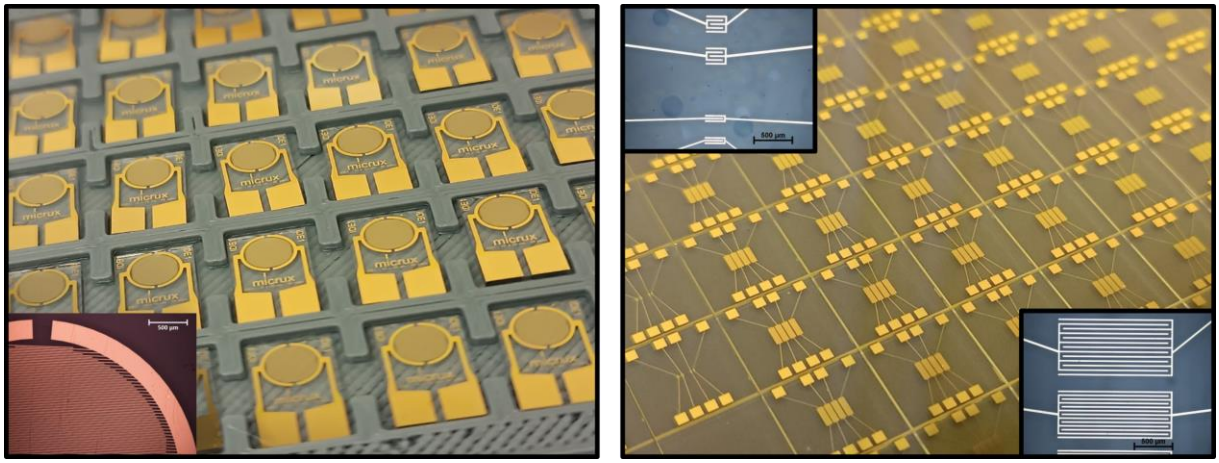

Figure 2.1. Substrate for sensor fabrication, in the inset zoom-in of the respective channel. Left panel, glass substrate, right panel, quartz substrate.

2.1.2 Organic Semiconductor Material

Organic semiconductors (OSCs) possess the ability to substitute inorganic silicon semiconductors due to their flexibility and lightness, along with their tunable optoelectronic characteristics. OSCs can be classified according to their polarity or charge carriers, but also according to the repeated units that form the material, which will determine the film structure and consequently also its electrical performance. Based on polarity, OSC can be classified into p-type and n-type, where the charge carriers contributing to the current flow are holes and electrons, respectively. Based on the combination of carriers, they can be classified as unipolar or ambipolar. Additionally, OSCs can be classified into molecular and polymeric according to the repeated units forming the material.[1] The success of the application of this class of materials in bioelectronics relies on the mobility of their charge carriers, and the diffusivity of these charges plays a pivotal role in determining their efficacy.[2]

An additional important feature of the OSC used specifically in Electrolyte Gated Organic Transistors (EGOTs) is the material (im)permeability to ions penetration from the electrolyte. The ion-impermeable OSCs form an electrical double layer (EDL) at the electrolyte/OSC interface upon gate bias application, while the ion-permeable OSCs form an EDL across the whole volume of the OSC. In this present work, we used only *p*-type OSCs.[3,4] Here I want to introduce TIPS-Pentacene, a molecular ion-impermeable OSC, and PEDOT:PSS and DPP-DTT, both polymeric and ion-permeable OSCs, which will be explained in more detail in this section.

2.1.2.1 TIPS-Pentacene

The small molecule 6,13-Bis(triisopropylsilylethynyl)pentacene (TIPS-Pentacene) is a derivative of the well-known OSC pentacene, functionalized in positions 6 and 13 with the functional group triisopropylsilylethynyl (TIPS), depicted in **Figure 2.2 A**. The functional group is positioned at a distance from the pentacene molecule through the utilization of a rigid alkyne spacer. This spacer is implemented in order to maintain a separation between the bulky groups and the aromatic core, thereby enabling the aromatic rings to approach as closely as possible. These modifications increase the π-orbital overlap by avoiding the herringbone pattern adopted by the non-functionalized pentacene.[5,6] These modifications in the molecular ordering have a great impact on the field-effect mobility (μ), which plays a major role in the performance of devices based on OSC as the active layer. Field-effect mobility values from 0.2 to even well above 1 $cm^2\ V^{-1}\ s^{-1}$ for organic field effect transistors (OFETs) have been reported, with a major effect of the deposition technique on such values.[6–12] For Electrolyte Gated Organic Field Effect Transistors (EGOFETs), μ values are slightly lower, in the range of 10^{-2} $cm^{-2}\ V^{-1}\ s^{-1}$ using water as electrolyte,[13,14] with an increase of one decade when using a saline solution as electrolyte.[14] In addition to its contribution to molecular ordering, the TIPS functional group provides further stability to the resulting material and enhances the solubility of the compound in most organic solvents, making it easier to process in solution for low-cost and large-area fabrication of organic transistors.[5,6] After deposition, TIPS-pentacene forms a film with large and elongated crystalline domains as can be seen in **Figure 2.2 B**. Shows an optical microscope image with a magnification of 20x. TIPS-Pentacene has been used as OSC for the development of anti-IL-6 EGOFET-based biosensor, described in Chapter 3.

Protocol

(i) 2% (w/w) TIPS-Pentacene in mixed hexene:toluene (20:80) solvent.

(ii) Stirring for 3 hours at 70 °C.

The TIPS-Pentacene solution was stored at 4 °C until use. Before use it was stirred at ~60 °C for a few minutes.

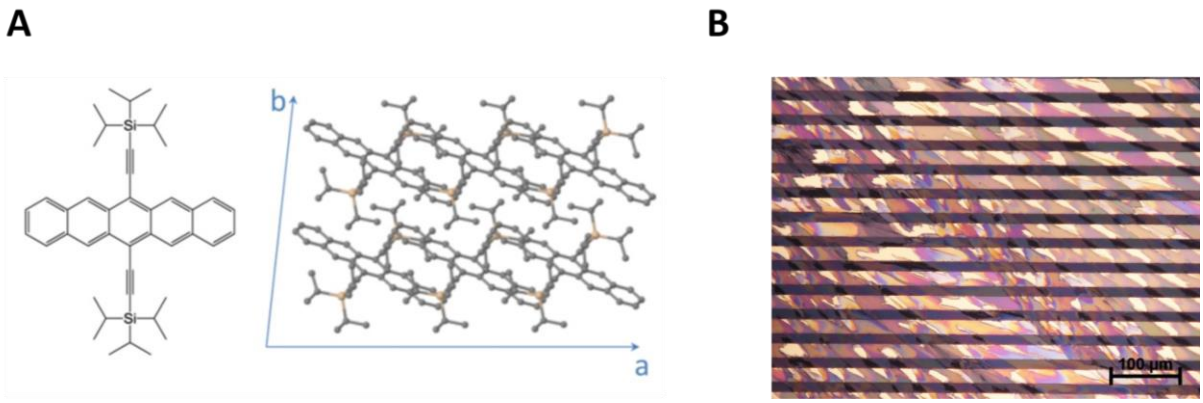

Figure 2.2. A) Chemical and packing structures of TIPS-Pentacene, adapted from D. T. James, *et al.*[15] **B)** 20x Optical microscope image of the source and drain interdigitated electrodes of a test pattern covered by TIPS-pentacene film (2% TIPS-Pentacene dissolved in hexene:toluene (20:80)).

2.1.2.2 PEDOT:PSS

The polymer Poly(3,4ethylenedioxythiophene) doped with poly(styrene sulfonate) (PEDOT:PSS) is the most widely employed channel material for the fabrication of Organic electrochemical Transistors (OECTs) because of its commercial availability and its extraordinary stability within an aqueous environment.[16] Since the development of PEDOT in 1988 by Bayer AG research laboratories,[17] PEDOT has been extensively explored as active material for organic electronics due to its high electrical conductivity, biocompatibility, and optical transparency.[18] However, one of the main drawbacks of PEDOT is its poor solubility in water or other solvents. It was not until 1997 that the addition of the water-soluble polyelectrolyte PSS overcame solubility issue, allowing the production and commercialization of a water-based solution that can facilitated the OSC deposition.[18,19] The resulting conjugated polymer is a highly doped *p*-type semiconductor, where the sulfonate anions on the PSS^- chains (dopant) compensate for the holes in the $PEDOT^+$ chains (**Figure 2.3 A**).[20] To further avoid the delamination and dissolution in aqueous environment, crosslinkers such as (3-glycidyloxypropyl) trimethoxysilane (GOPS) and divinylsulfone (DVS) are required.[21,22]

Here we focus on the effect of GOPS, since it is the crosslinker used for the fabrication of PEDOT:PSS based OECTs. GOPS might lead to the reaction between the sulfonic acid group and the epoxy group of PSS and GOPS, respectively, at very high temperatures (*i.e.*, 140°C).[21] All these previous described modifications have led to a more fibrillar microstructure, with a better interconnection of PEDOT domains that improves its electrical properties. The final PEDOT:PSS film is therefore featuring very high electrical conductivity (> 1000 S cm^{-1}),[23,24] mixed electrical and ionic conductivity, stretchability, biocompatibility, low toxicity, and transparency. All these properties span the application of PEDOT:PSS based devices from

batteries and supercapacitors development to light emitting electrochemical cells, electrochromic windows, sensors, and OECT based sensors and neuromorphic computing.[16] PEDOT:PSS has been exploited as channel material for the fabrication of OECT-based biosensor for the detection of IL-6 (Chapter 3) and anti-CMV Antibody (Chapter 5).

Protocol

(i) Weight PEDOT:PSS (~1 g) and add 5 % (w/w) dimethyl sulfoxide (DMSO) and 0.2 % (w/w) GOPS.

(ii) Mix solution in ultrasonication bath at 70 °C for 20 minutes.

The PEDOT:PSS solution was stored at 4 °C until use. Before use it was ultrasonicated for a few minutes and then diluted in water (1:4) for spin coating and (1:200) for drop casting, and then ultrasonicated again before deposition.

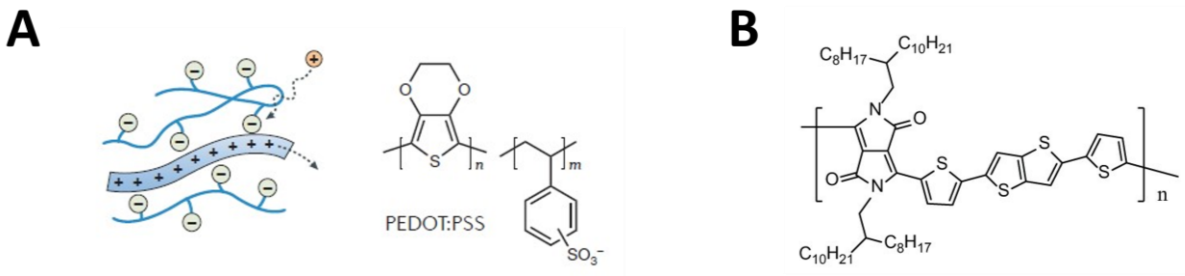

Figure 2.3. A) conjugated polymer PEDOT:PSS, polymer structural arrangement (left, adapted from Rivnay J. *et al.*[3]), chemical structure (right). **B)** Chemical structure of polymer DPP-DTT (adapted from Li J. *et al.*[25])

2.1.2.3 DPP-DTT

This *p*-type organic semiconductor was first designed in 2012 by Li J. *et al.*,[25] aiming for a conjugated polymer, where the strong donor moiety was the molecule dithienylthieno[3,2-b]thiophene (DTT), and the weaker acceptor moiety was the molecules Nalkyldiketopyrrolo-pyrrole (DPP) (**Figure 2.3 B**). The obtained OSC is a conjugated polymer that is soluble in organic solvents, but when it has a high molecular weight, chlorobenzene is the optimum solvent due to its great solvency ability for soluble polythiophene polymers.[25] As it has been previously stated, a soluble OSC facilitates the fabrication of organic transistors, allowing the formation of the semiconducting channel directly from the solution (see Section 2.1.3). The resulting film was expected to have great electrical properties since increasing the molecular weight of the polymer can lead to a more tightly packed and interconnected structure, which allows for more efficient movement of charge through the material.[26–28] An extensive characterization is reported in the work by Li J. *et al.*, where the resulting film proved to be

composed by large fibrous crystalline domains, with very high crystallinity which is correlated to tighter π−π stacking (3.43 Å π−π stacking distance). Electrical characterization of OFET devices showed very high hole mobility values in saturation regime (up to 10.5 $cm^2 V^{-1} s^{-1}$) and ON/OFF ratio above 10^6.[25] All these properties make DPP-DTT a promising OSC candidate for EGOT fabrication. Since its synthesis it has been used as active material for OFETs[29–31], EGOTs[32–34], and organic photovoltaic cells[35] fabrication. In this work it was employed for the development of IL-1β (Chapter 4) and Ptau (Chapter 6) EGOT-based biosensor.

Protocol

(i) 5 mg mL^{-1} DPP-DTT in Dichlorobenzene (DCB).

(ii) Stirring for one hour at 70 °C.

DPP-DTT solution was stored at 4 °C until use for no longer than one week. Before use it was stirred at 70°C for a few minutes.

2.1.3 Processing Techniques

One of the greatest advantages of working with organic semiconductors is that they can be processed utilising techniques that are both more energy-efficient and cost-effective, while being performed under near ambient conditions. In the past decades, major improvements have been made on the development of novel materials, paying attention not only to their chemical structure, but also to the processing techniques, as the film morphology and its possible defects determine the device electrical performance. In the pioneering years, vapor phase growth techniques were explored for the deposition of organic semiconductors, yielding some of the highest charge carrier mobilities. In more recent years, solution processing techniques have been considered a more industrially relevant route for the deposition of OSCs, but the quality and performance of solution-deposited thin films have not been able to match that of vapor-grown single crystals until recently.[36] The different solution-processing techniques have been reviewed by Diao Y. *et al.*,[37] categorizing the many solution-processing techniques into: drop casting, spin coating, meniscus-guided coating, and printing. In this work we exploited the bench techniques, i.e. drop casting and spin coating.

2.1.3.1 Drop Casting

This is one of the simplest techniques for OSC deposition. It consists of casting the OSC solution followed by the subsequent solvent evaporation, depicted in **Figure 2.4 A**. This technique can be used for the deposition of single crystals or thin films; however, in the latter case it presents several drawbacks, such as poor reproducibility, and might lead to non-

homogeneous films.[37,38] Therefore, several modifications have been developed to improve the crystal and films quality. For instance, the implementation of vibration-induced crystallization, which entails subjecting the drop-cast solution to unidirectional sound waves (~100 Hz) during the process of evaporation, has been identified to improve the crystal quality and the device electrical performance. Another target would be the control of the solvent evaporation, which can be accomplished by utilizing mixed solvents, azeotropic mixtures, sealed chambers, saturated solvent environments, inert gas purging, and surface treatments.[37] In this thesis, drop casting was implemented in the development of OECTs, in particular for deposition of the conjugated polymer PEDOT:PSS, using heating annealing as post treatment (Chapter 5).

Protocol for PEDOT:PSS deposition(Chapter 5)

(i) Rinse quartz TP with acetone, water, and dry under N_2 flow.

(ii) TP in acetone at 70 °C for 10 minutes. Rinse with water and dry under N_2 flow.

(iii) TP in piranha solution (H_2SO_4:H_2O_2 1:1) for one minute at 150 °C, abundantly rinse with water and dry under N_2 flow.

(iv) TP in hot plate at 120 °C, cast 10 µL PEDOT:PSS diluted in water (1/200) and cure for 30 minutes.

Devices were stored at room temperature until use.

2.1.3.2 Spin Coating

Spin coating is one of the most used techniques for obtaining controlled and uniform OSC films. It involves four stages: 1) deposition, the dropping of the OSC solution on the substrate, followed by: 2) spin-up, the acceleration of spin to a high angular velocity that occurs within a fraction of a second (**Figure 2.4 B**); 3) spin-off, the centripetal force, in combination with the solution surface tension, results in the uniform distribution of the solution. Simultaneously, 4) the solvent undergoes evaporation, leaving a uniform film covering the substrate.[37,39,40] The film thickness is controlled by the OSC concentration, the solution viscosity, and the spin parameters (velocity and acceleration), where the thickness is proportional to inverse of the square root of the spin speed. Once the liquid is spread, the film thickness will be determined by viscous forces, which depend on the solution viscosity and the solvent evaporation process that is contingent upon the solvent's volatility, vapor pressure, and ambient conditions. It is worth mentioning that a non-uniform evaporation rate, such as at the edge of the substrate, will yield a non-homogeneous film in such regions.[39]

Here I would like to highlight the importance of the evaporation rate and how it can be tailored to improve the crystallinity order of the resulting OSC film. It has been proved that longer solvent evaporation times lead to a better molecular arrangement and, therefore, more crystalline structure and better electrical performance. This can be achieved by solvent vapour annealing (SVA), keeping the film in a vapour rich environment.[41,42] This is one of the explored strategies for the deposition of TIPS-Pentacene, explained in more detail in Chapter 3. Briefly, after the spin coating the substrate was still wet, and was covered by a petri dish and positioned on a hot plate, slowing down the solvent evaporation and curing the film by SVA. In the same chapter, spin coating was also used for the deposition of PEDOT:PSS, proceeding with heating annealing, it yielded a bluish transparent film. In Chapter 6 this same technique was used for the deposition of DPP-DTT, followed by thermal annealing for the development of p-Tau EGOT-based biosensor, resulting in a coloured polymer film.

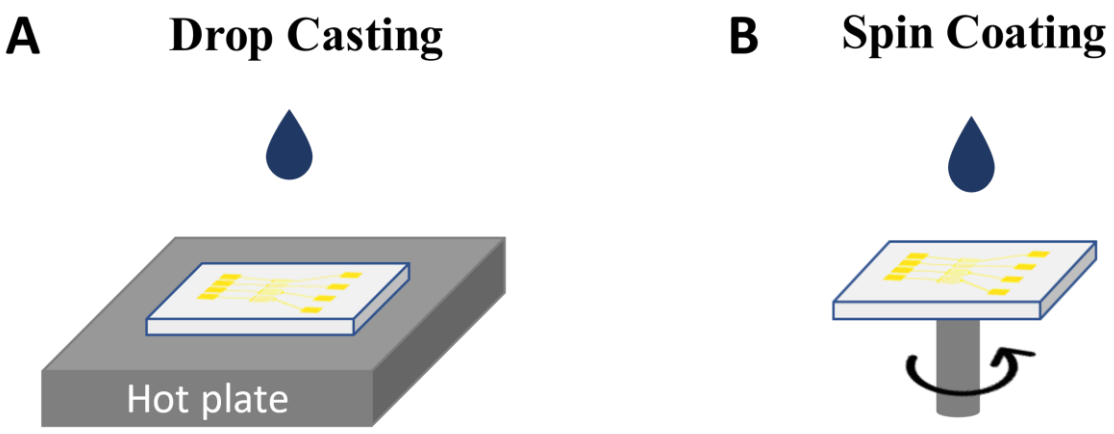

Figure 2.4. Solution-based processing techniques. **A)** Drop casting followed by thermal annealing. **B)** Spin coating, the spin parameter will change according to the substrate and the OSC.

Protocol for TIPS-Pentacene deposition (Chapter 3)

(i) Rinse quartz TP with acetone, water, and dry under N_2 flow.

(ii) TP in acetone at 70 °C for 10 minutes. Rinse with water and dry under N_2 flow.

(iii) TP in piranha solution (H_2SO_4:H_2O_2 1:1) for one minute at 150 °C, abundantly rinse with water and dry under N_2 flow.

(iv) TP in spin coater, centre position. Pipet 80 µL TIPS-Pentacene solution on substrate and spin for 15 seconds at 600 rpm.

(v) Heating annealing on hot plate at 60 °C for 30 minutes in a closed chamber, vapour rich environment.

Devices were stored at room temperature in a desiccator to prevent moister and protected from the light.

Protocol for PEDOT:PSS deposition (Chapter 3)

(i) Rinse quartz TP with acetone, water, and dry under N_2 flow.

(ii) TP in acetone at 70 °C for 10 minutes. Rinse with water and dry under N_2 flow.

(iii) TP in piranha solution (H_2SO_4:H_2O_2 1:1) for one minute at 150 °C, abundantly rinse with water and dry under N_2 flow.

(iv) TP in spin coater, centre position. Pipet 80 µL PEDOT:PSS diluted in water (1/5) on substrate and spin in two steps: 1) 3 seconds at 500 rpm, followed by 2) 20 seconds at 2000 rpm.

(v) Heating annealing in the oven at 120 °C for 45 minutes.

Devices were stored at room temperature until use.

Protocol for DPP-DTT deposition (Chapter 4 & 6)

(i) Micrux TP in ultrasonication bath for 15 minutes in Hellmanex 1%, 15 minutes water, and 15 minutes in ethanol. Washing (x3) in between ultrasonication baths. Final rinse with ethanol and dry under N_2 flow. (Chapter 4)

(ii) Quartz TP was cleaned as described before, with acetone and piranha solution (Chapter 6)

(iii) TP in spin coater, channel positioned in the centre. Pipet 10 µL DPP-DTT solution on substrate and spin for 2 minutes at 2000 rpm.

(iv) Heating annealing in the oven at 140 °C for 45 minutes.

Devices were stored at room temperature immersed in 50 mM Phosphate buffer solution until use.

2.1.4 Gate Functionalization

Another important part of the device development is the gate functionalization, since here we are using these EGOT devices as biosensors. The sensing mechanism relies on the alteration of the EDL at the electrolyte/gate or electrolyte/OSC interface, depending on where the biorecognition unit has been immobilized. The most prevalent method in biosensing with EGOTs involves antibody (Ab) attachment to a gold gate, given the well-established protocols for immobilizing biomolecules on bare or modified metal surfaces, predominantly gold. The

utilization of peptide- or oligonucleotide-based aptamers or other biorecognition units, as well as the functionalization of the OSC instead of the gate electrode, is also a viable option, albeit less frequently employed.[43] Antibodies are considered an exceptional recognition receptor due to their high specificity, stability, and versatility. They can be chemically conjugated to various reporter types and coated onto diverse surfaces. Moreover, antibodies can be generated against a wide range of biological materials, ranging from ssDNA to proteins. The scientific community has mastered the genetics of antibodies, manipulating them and producing an array of specific antibodies. As a result, antibodies are a valuable tool in research and diagnostics biosensing applications, and have been used as the recognition unit of choice during this thesis.[44,45]

In this section, the emphasis is on the functionalization of the gate, with a more detailed description of the four strategies used during this work. Torricelli *et al.*[46] reviewed and summarized, among other aspects of EGOTs, the different gate functionalization strategies, describing it as a three-step process: **1) the linker**, it refers to the functional groups or molecules that interact with the metal surface by covalent or strong non-covalent bonds. Regarding the gold surface, metal-sulphur covalent bond is one of the most exploited strategies. This and other approaches summarized in the aforementioned review are characterized by their simplicity, versatility, and ease of implementation, as they can be based on either pre-existing chemical functionalities or molecular groups that can be readily incorporated through molecular engineering. **2) the primer** is the biolayer that works as matrix for the anchoring of the biorecognition unit. We can find three major approaches according to the nature of the primer: *i) avidin/biotin layer*, based on the well-known and highly stable biotin-avidin strong non-covalent interaction, where the avidin molecule (either streptavidin or neutravidin) binds on one side the biotin group linked to the self-assembled monolayer (SAM), and on the other side it binds biotinylated biorecognition moieties. *ii) protein A/G monolayer*, these proteins are either molecularly engineered to bear the linker for direct immobilization, or can be attached to a SAM through amide bonds. The use of these proteins ensures the correct orientation of the antibody at the gate/electrolyte interface, due to the strong affinity of the protein A/G to the Fc region of the IgG-type antibodies. *iii) SAM-forming linkers*, the biorecognition moieties are attached to the SAM by click chemistry or by physical interactions; this is one of the most explored techniques, exploiting the chemical activation by EDC/NHS reaction to form the amide bond between the SAM and the biorecognition protein. **3) passivation** of the gate with

an antifouling molecule to avoid non-specific adsorption. Antifouling SAMs or bovine serum albumin (BSA) have been used to fill the left bare metal spots left after functionalization,.[46]

During this work we explored the three different primers for gate functionalization, which will be introduced in more detail in the following section. Additionally, we also explored another elegant strategy based on the immobilized metal affinity chromatography (IMAC), that will also be explained later in this section.

2.1.4.1 SAM-forming linkers

For the development of the IL-6 EGOT-based biosensors (Chapter 3), we used a mixed SAM of mercaptoundecanoic acid:mercaptohexanol (MUA:MCH). Before the functionalization process, the gate, a polycrystalline gold electrode, was cleaned following a standard protocol: after a first incubation in 2.5 M KOH at 130 °C for 4 hours, the gate was abundantly rinsed with water and then incubated again in concentrated sulphuric acid at 220 °C for 2 hours. Finally, the electrode was abundantly rinsed with water and dried under nitrogen flow.

In this strategy, the mixed SAM of MUA:MCH have the ability to self-assemble on a gold surface thanks to the thiol linker, exploiting the metal-sulphur covalent bond. The SAM layer has carboxylic and hydroxyl terminal groups. The MCH molecule is used as spacer since it has been proved that the mixed length of the SAM chains eventually leads to a denser protein layer.[47] The carboxylic groups of the chains are chemically activated through EDC/NHS and, by exploiting the carbodiimide crosslinker chemistry, the antibodies were covalently bound to the SAM surface by incubation in anti-IL-6 Ab. Once the antibody biolayer is formed, the remaining activated carboxylic groups are blocked by immersion in ethanolamine (ETA), this step providing chemical stability to the biolayer. Finally, the passivation is performed by incubating the gate in a mixed solution of BSA and detergent Tween20 to avoid non-specific adsorption. The physisorption of BSA/Tween20 should promote a more compact biolayer, filling the gaps left after the Ab immobilization.[48] **Figure 2.5** provides a schematic representation of the functionalization process.

Protocol:

(i) Overnight incubation of the gold wire in a mixture of SAM-forming molecules MUA:MCH (1:3) diluted in ethanol at concentration 1mM and 3mM for MUA and MCH respectively.

(ii) Immersion in 200mM EDC mixed with 50mM NHS in water for 30 minutes.

(iii) Incubation in 0.1 mg/mL anti-IL-6 Ab in 50mM Phosphate Buffer solution, pH 7.4, for one hour.

(iv) Immersion in 0.5 M ETA in Phosphate Buffer solution, pH 7.4, for 30 minutes. (v)

(v) A final step of incubation in 0.1 mg/mL BSA, 0.05% Tween 20 in 50mM Phosphate Buffer solution, pH 7.4, for 30 minutes.

After each incubation step, the gold wire was gently rinsed with the pertinent buffer; all incubation steps were performed at room temperature.

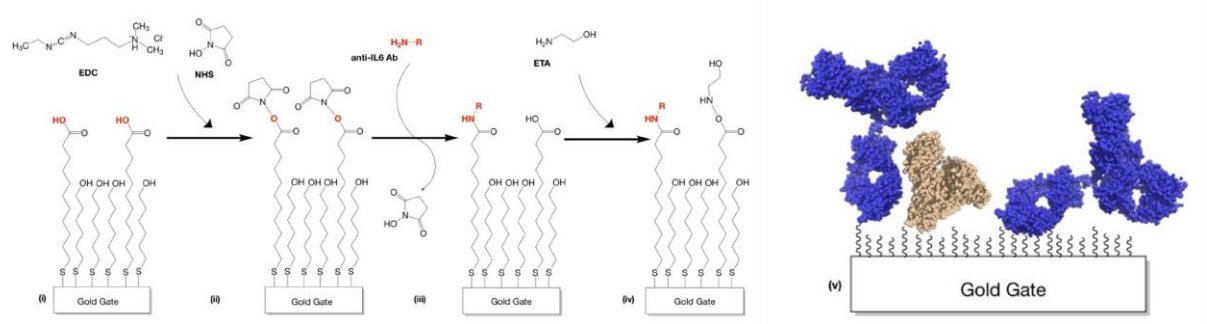

Figure 2.5. Schematic drawing of the gate functionalization procedure from step (i) to step (iv). We can observe the chemical activation of the carboxylic acid terminal groups, which bind covalently the anti-IL-6 antibody (Ab). (v) is a cartoon representation of the possible assembly of the proteins (Antibodies and BSA) at the electrolyte/gate interface; the detergent Tween 20 is not represented in this drawing.

2.1.4.2 Avidin/biotin layer

For the development of IL-1β EGOT-based biosensor, we used a biotinylated oligo(ethylene glycol) (OEG) SAM, using as spacer OEG SAM to yield a biotin-OEG:OEG ratio of 1:9. The gate electrode was a polycrystalline gold, which was cleaned as previously described. To ensure a well-formed SAM monolayer, the gold electrode was incubated in the mixed SAM overnight. This strategy exploits the well-known avidin-biotin strong non-covalent bond (K_d $\sim 10^{15}$);[49] in this case we used Neutravidin (NA). As described before, OEG film formation is one of the strategies for passivation, however, in this case we also included the BSA/Tween20 physisorption since optical techniques (as explained in next section) showed non-specific adsorption in the absence of BSA/Tween20. I would like to highlight that the antibody presents 3-5 biotin tags, randomly distributed on the Ab surface, therefore the orientation of the antibody with respect to the surface is not uniform. In **Figure 2.6** a representation of the possible configuration of the functionalized gate is provided.

Protocol:

(i) Overnight incubation of the gold wire in a mixture of SAM-forming molecules biotin-OEG:OEG (1:9) diluted in ethanol at concentration 0.1 mM and 0.9 mM for biotin-OEG and OEG respectively.

(ii) Incubation in 2μM NA in 1x PBS, pH 7.4, for 20 minutes.

(iii) Incubation in 0.1 mg/mL anti-IL-1β biotinylated Ab in 1x PBS, pH 7.4, for 40 minutes.

(iv) Incubation in 0.1 mg/mL BSA, 0.05% Tween 20 in 1x PBS, pH 7.4, for 20 minutes.

After each incubation step, the gold wire was gently rinsed with the pertinent buffer; all incubation steps were performed at room temperature.

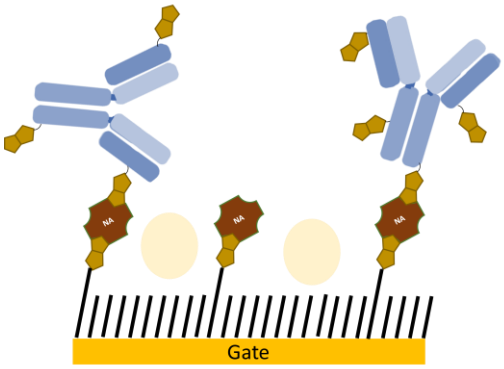

Figure 2.6. Cartoon representation of the possible configuration of the functionalized gate in the electrolyte/gate interface. NA is represented in brown, showing the four pockets for biotin binding, and BSA in light cream circle shape. Tween20 molecule is not included in the drawing.

2.1.4.3 Protein G monolayer

The strategy of choice for the development of a p-Tau sensor was based on using protein G as immobilization matrix, depicted in **Figure 2.7**. As it has been explained before, Protein G can be engineered to bear a linker. We exploited the high affinity of the Protein G to the Fc domain of the Ab, providing an Ab biolayer within the biorecognition region with a uniform orientation with respect to the surface. This strategy has been previously exploited by our group,[50,51] yielding satisfactory sensitivity and specificity, with limits of detection (LOD) even below 1pM.[51] The cys-Protein G might be forming dimers through disulphide bonds between the cyst-tag, therefore a previous reduction step is beneficial for a higher surface coverage of Protein G. For this purpose, tributyl phosphine and tris (2-carboxyethyl) phosphine (TCEP) was used as a reducing agent, since it has been widely applied in molecular biology for disulfide bond (S-S) cleavage. When used in the absence of denaturing agents and at room temperature, it only reduces the more accessible disulfide bonds, leaving intact the S-S bond in the protein core.[52] Regarding the passivation, we used OEG SAM to cover the gold spots left after the cys-Protein G immobilization, and added BSA to contribute to the anti-fouling activity. The

functionalization process was performed in a planar gate on Kapton substrate, produced by photolithography, featuring a 24 mm^2 area.

Protocol

(i) Reduction of the cys-protein G disulfide bond. Take 50 µL TCEP in an Eppendorf and centrifuge for 1 minute at 1000 g, remove supernatant, and add ~ half of the initial volume of 50 mM Phosphate Buffer solution (pH 7.4). Repeat centrifugation, remove supernatant, and add buffer solution. Repeat this process three times, to make sure we removed as much as possible of the clay in the TCEP solution. Add 2 mg mL^{-1} cys-Protein G in 50mM Phosphate buffer solution to the remaining pellet, mix and centrifuge for 1 minute at 1000 g. The reduced cys-Protein G is in the supernatant.

(ii) Overnight incubation in 2 mg mL^{-1} reduced cys-Protein G at 4 °C. Gentle wash with buffer solution.

(iii) Incubation in 0.1 mg mL-1 anti-p-Tau_{181} antibody in 50 mM Phosphate buffer pH 7.4 for 1 hour.

(iv) Incubation in 10 µM OEG in water for 30 minutes. Wash with buffer solution.

(v) Incubation in 0.1 mg mL^{-1} BSA in 50 mM Phosphate buffer pH 7.4 for 30 minutes.

The whole process was performed at room temperature, except for step (ii), in a humid environment to prevent the solution evaporation.

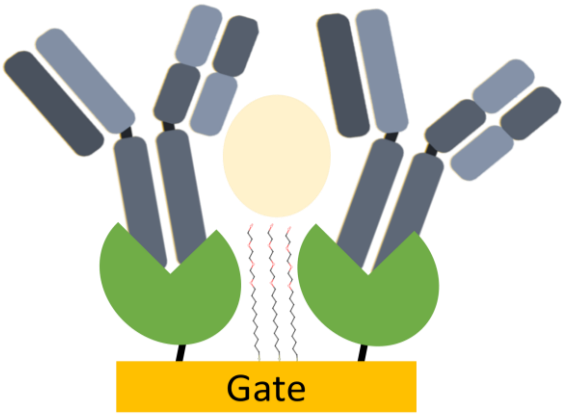

Figure 2.7. Cartoon representation of the gate functionalization using Protein G (in green), OEG and BSA (circle light cream) as passivation layer. Here is depicted the optimal Ab orientation facing towards the electrolyte.

2.1.4.4 Metal ion chelate affinity

The immobilization procedure that we used for the His-tag Cytomegalovirus phosphoprotein 65 (CMV pp65) closely parallels the strategy proposed by W. Knoll and co-workers in 2004[53] to develop protein-tethered lipid bilayers, which in turn was inspired by the well-established

metal-ion affinity chromatography, in which proteins with histidine residues interact with metal ions fixed to a solid support.[54] In this case, the metal-chelating group lysine nitrilotriacetic acid (ANTA) was immobilized on the gold surface using Lomant's reagent as a crosslinking agent. A metal-containing complex was obtained by immersion in a Cu^{2+} solution. The coordinated divalent copper ions can then be used to reversibly bind a recombinant CMV pp65 endowed with a poly histidine tag (6-His-tag CMV pp65) that is used as biorecognition unit for the detection of anti-CMV Ab. This elegant approach presents an opportunity for adaptability in the functionalization process, given the prevalence of the 'histidine tags' in the production of recombinant proteins, which in our perspective facilitates the binding of diverse proteins to the electrode interface. The histidine tag is frequently used and, as it is located at a specific position of the protein (N- or C-terminus), it facilitates the formation of a more ordered bio-layer on the electrode surface. In contrast, other standard electrode functionalization strategies, such as the EDC/NHS method, link protein to carboxylate SAM with a random orientation, leading to differences in binding efficiencies depending on the protein orientation. The functionalization process is illustrated in **Figure 2.8**. For this strategy the gate electrode was a square silicon substrate (16 mm^2 area) with an adhesive layer of chromium (~5 nm) and a gold layer (~50 nm), both deposited by evaporation.

Protocol:

(i) Incubation of the gold electrode in 5 mM 3,3′-Dithiodipropionic acid di(N-hydroxysuccinimide ester) (DTSP, Lomant's reagent) in DMSO overnight, followed by washing steps with DMSO and water.

(ii) Incubation in 10 μM OEG in water for 30 minutes.

(iii) Incubation in 80 mM N_{α},N_{α}-Bis(carboxymethyl)-L-lysine hydrate (ANTA), buffered at pH 9.8, for 3 hours.

(iv) Incubation in 40 mM $CuSO_4$ in 50mM acetate buffer, pH 5.5 for 30 minutes.

(v) Incubation in 0.05 mg/mL CMV pp65 in 50 mM Phosphate Buffer, pH 7.4 for 2 hours.

(vi) Final incubation in 0.1 mg/mL BSA mixed with 0.05% Tween20 in 50 mM Phosphate Buffer, pH 7.4 for 30 minutes.

After each incubation step, the gold wire was gently rinsed with the pertinent buffer and the whole process was performed at room temperature.

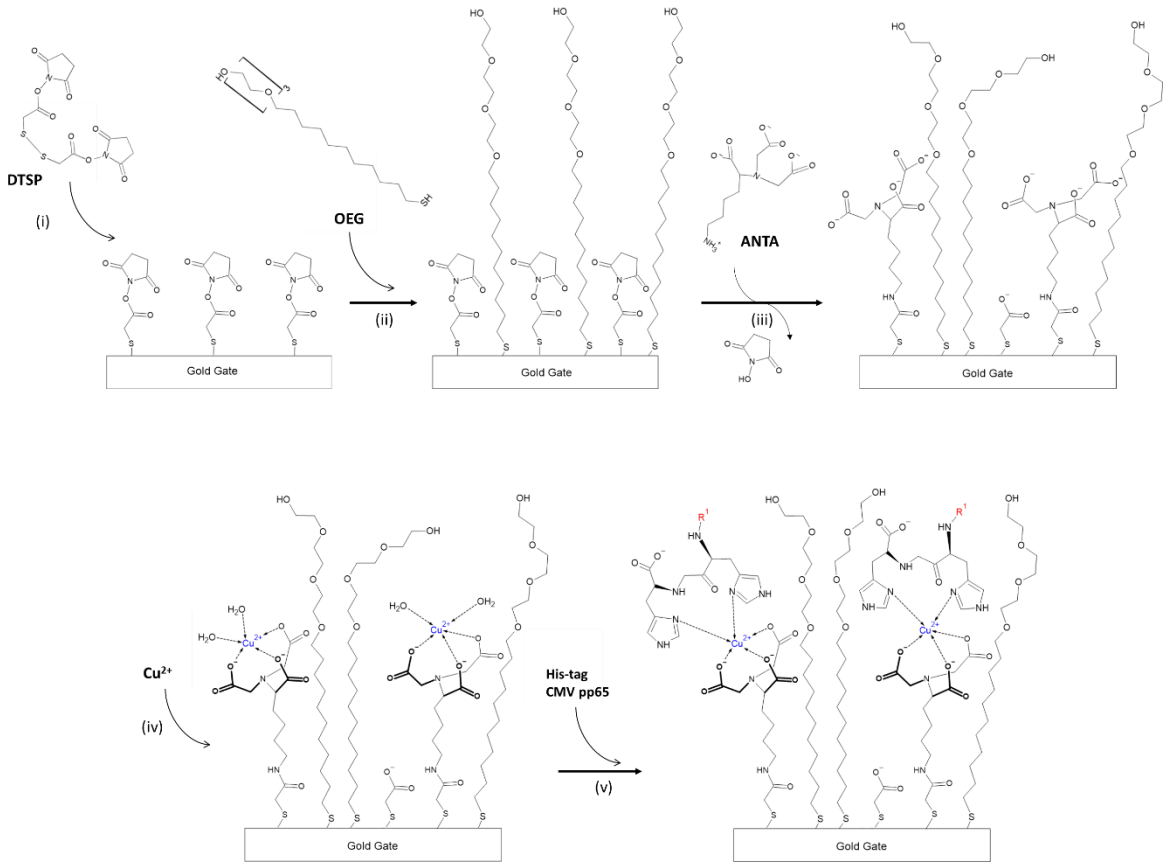

Figure 2.8. Schematic drawing of the gate functionalization procedure from step (i) to step (v). Here it is depicted the metal ion Cu^{2+} interacting with the poly-Histidine of the CMV pp65.

2.2 OPTICAL CHARACTERIZATION

Surface plasmon resonance (SPR) sensors have been extensively employed in the study of biomolecular interactions and for sensing, due to their high sensitivity, label-free detection, non-invasive measurement, and real-time analysis, among others. SPR sensors operate based on their sensitivity to alterations in the refractive index of the surrounding media, thereby enabling the detection of medium to large-sized molecules, which can generate significant changes in refractive index. The two most common configurations used are **prism SPR sensor** and **Fiber Optic SPR** (FO SPR). Furthermore, a common practice is the implementation of **surface plasmon-enhanced fluorescence spectroscopy** (SPFS) to SPR when seeking for the detection of smaller analytes.

2.2.1 FO SPR

The FO SPR sensor was first proposed by R.C. Jorgenson in 1992.[55] The main advantages of FO SPR is its high sensitivity, the amenability for miniaturization, its ease of integration, and fast response. The FO probes were prepared by Prof. Wolfgang Knoll's group at the Austrian Institute of Technology (AIT), and were prepared to be used as SPR substrates by sputtering 50 nm of gold on the fiber surface.[56] White light was guided to the fiber tip, where it coupled

to surface plasmons within the optically active section at the end of the tip. Consequently, the light was back-reflected inside at the gold-coated cross section of the fiber tip and measured by a spectrometer. The obtained spectra were normalized to measurements of the tip in air, and processed using dedicated LabView software.[57] In **Figure 2.9** the FO SPR setup is depicted.

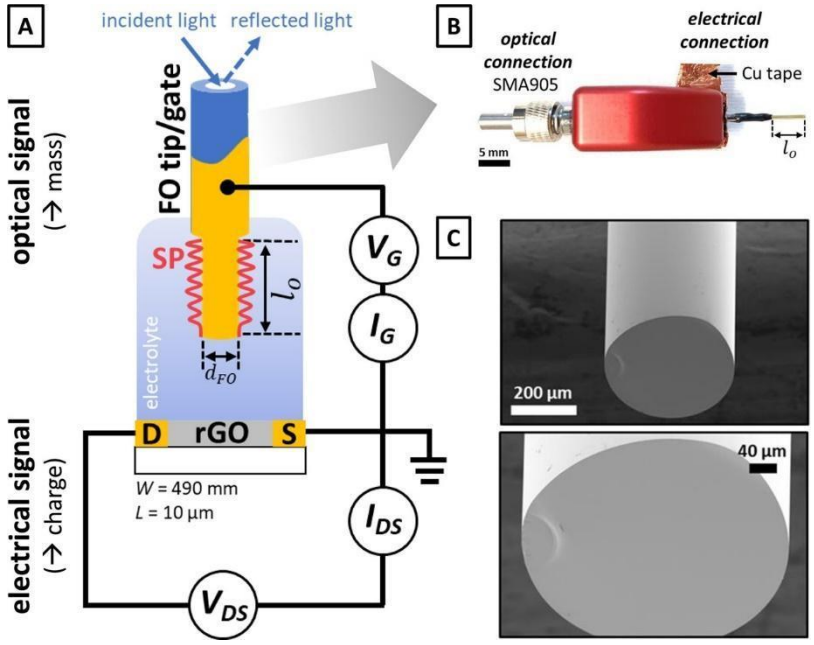

Figure 2.9. A) Schematic representation of the FO SPR setup, in this case it includes the combined electrical and optical setup. **B)** combined optical and electrical connection to the FO probe. **C)** Scanning Electron Microscopy (SEM) images of the FO tip. This figure is reproduced from Hasler et al.,[56] this is the exact equipment and FO probes used for the optical characterization.

This technique was used for the monitoring of the gate functionalization. The first step was the modification of the gate with different molecules, depending on the specific sensor under development, i.e. with the SAM: MUA:MCH for IL-6 sensor, biotin-OEG:OEG for IL-1β sensor, and with the metal-chelating group lysine nitrilotriacetic acid (ANTA) immobilized on the gold for anti-CMV Ab sensor. The functionalization proceeds as explained above for each system, with washing steps with 1x PBS (x2) by immersion in between steps. The measurements were performed in 1x PBS as electrolyte, in real-time, and without labels. The optical signal is presented as a shift of the resonance wavelength (λ_{SPR}) which corresponds to the minimum of the dip in the back-reflected spectrum. The shift of the resonance wavelength corresponds to local refractive index changes, associated to the molecular mass of the absorbed molecules at the gold surface/electrolyte interface. To normalize the sensor response, the optical signal is divided by the sensitivity (S_B) of each sensor obtained from a calibration curve by exposing the sensor to increasing concentrations of sucrose, yielding a shift in refractive

index units (RIU). From this value we can estimate the biolayer thickness by dividing the ΔRIU by the factor *f*, which is is the coefficient obtained from the simulations that correlates the shift in RIU with the thickness of the adsorbed layer. From the analysis of the shift of λ_{SPR}, one can estimate the surface mass density (Γ).

$$\Gamma = d_p(n_p - n_s)\left(\frac{\partial_n}{\partial_c}\right)^{-1} \quad (2.1)$$

where d_p is the biolayer thickness (derived from the λ_{SPR} using a simulated calibration curve as explained in elsewhere[56]), n_p and n_s are the refractive index of the biolayer and the electrolyte, respectively, and $\frac{\partial_n}{\partial_c}$ is the coefficient relating the changes in the refractive index to the layer formation that is typically established to be 0.2 $mm^3\ mg^{-1}$ for biolayers.[58] The application of this equation yields a surface mass coverage in terms of ng cm^{-2}, and such value can be transformed into molecules cm^{-2} taking into consideration the protein molecular weight and the Avogadro number. The resulting values are presented for each system in their corresponding chapters.

2.2.2 SPFS

As mentioned before, SPR biosensors can be applied for the detection of large and medium size molecules, able to produce a measurable change of the refractive index. However, when it comes to small molecules, especially at very low concentrations, it is necessary to implement complementary techniques. Surface Plasmon-enhanced Fluorescence Spectroscopy (SPFS) enhances the SPR sensitivity of the biosensor by several orders of magnitude, since the fluorescence signal is increased due to the surface plasmon-enhanced intensity of the electromagnetic field on the SPR surface.[59,60] The implementation of SPFS to SPR is performed in the Kretschmann configuration, depicted in **Figure 2.10**, where the "Plasmonic biochip" is a LSFN9 glass slides with 2 nm Cr and 50 nm Au by evaporation, the "PMT" is the fluorescence detector (SPFS), and the "R(t,θ)" is the SPR signal.

This optical technique was used for the validation of the gate functionalization for IL-1β detection. FO SPR has proven to be a very useful technique for monitoring the different gate functionalization strategies since it is sensitive to medium and large molecules, we were able to monitor the adsorption of antibodies (150 kDa), NA (60 kDa), and CMV pp65 (65 kDa). However, when it comes to sensing small analytes, this label-free technique lacks sensitivity. We used SPFS for monitoring the IL-1β detection (Chapter 4), since the attempts with FO SPR were not successful. Measurements were performed in a flow-cell of approximately 12 μL volume. The flow was accomplished by using a peristaltic pump at 0.5 mL min^{-1} flow rate. In

the case of the SPFS readout, the emitted fluorescence from the sensors was collected through the flow-cell and filtered at a specific wavelength (λ=633). The fluorescence intensity is given as counts per second (cps). In this configuration, the SPR is set at a fixed angular scan, measuring the changes in reflectivity R(θ) upon mass adsorption, which is then transformed into changes in refractive index units (RIU).

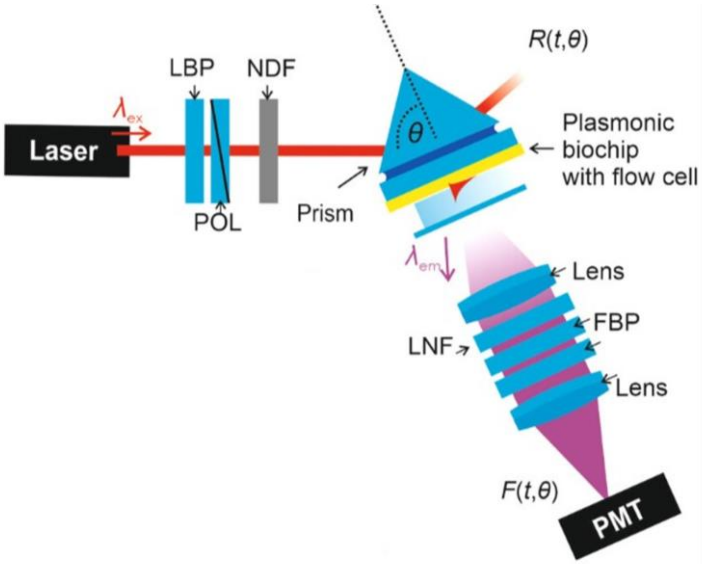

Figure 2.10. Schematic representation of the SPR/SPFS optical setup. Adapted from Schmidt K. et al.[60]

The setup measures simultaneously the SPR and SPFS signal. It started from the already functionalized sensor chip with the biotin-OEG:OEG SAM, then it was assembled into the microfluidics and the SPR/SPFS setup. The functionalization was monitored only by SPR, in absence of fluorophores, therefore without fluorescence signal. The sensing part of the experiment was designed as a sandwich assay, where we have the capture antibody anti-IL-1β Ab, then it is exposed to the analyte IL-1β, and finally the complex Ab-analyte is exposed to the fluorochrome-labelled detection antibody. As a control, before exposing the sensor chip to the analyte, it was exposed to the detection antibody in absence of IL-1β, to test the sensor selectivity. Then, the sensor was exposed to increasing concentrations of IL-1β, followed by a fixed concentration of the detection antibody (2μg mL^{-1}) to ensure surface saturation. The corresponding results are provided in Chapter 4.

2.3 ELECTROCHEMICAL CHARACTERIZATION

Electrochemical techniques such as electrochemical impedance spectroscopy, cyclic voltammetry, chronoamperometry, chronopotentiometry, and electrochemical microscopy, are applied for the study of heterogeneous chemical reactions, such as electrode transfer, and to investigate both the properties of electrode/solution interfaces properties as well as the

electrochemical properties of redox active molecules in solution. Therefore, these techniques can be used in the field of energy conversion and storage, corrosion, sensors and biosensing applications.[61]

2.3.1 Cyclic Voltammetry

Cyclic voltammetry (CV) is a widely utilized and powerful electrochemical technique that is frequently employed for the study of electroactive species either immobilized on or diffusing to an electrode surface. As such, it can be also used for investigating interfacial phenomena at an electrode surface and bulk properties of material on electrodes.[62] A typical three-electrodes setup (**Figure 2.11 A**) includes a working electrode (WE), which is an electrical conductor, usually platinum, gold, mercury, or glassy carbon; reference electrode (RE), typically Ag/AgCl; and counter electrode (CE), often a platinum wire. The potentiostat is the measurement instrument, it controls the applied potential to the WE vs. the RE, while compensating the cell resistance and measures the current flowing between the WE and the CE. The output of the CV is a plot where the measured current is expressed as a function of the applied potential. When working with solutions containing electroactive species, together with high concentrations of an inert electrolyte (i.e., KCl) to reduce the cell resistance, the species can undergo redox reactions according to the applied potential. When the scan potential is negative (cathodic), the species can be reduced at the WE, while at positive potentials (anodic), the species are oxidized. These processes lead to the presence of the corresponding cathodic and anodic peaks in the cyclic voltammograms (**Figure 2.11 B**).[62–64] For electrochemical reversible electron transfer processes, the peak current (ip) is given by the Randles-Sevcik equation:

$$i_p = (2.69 \times 10^5) v^{1/2} A D^{\frac{1}{2}} C_0 \qquad (2.2)$$

where, v is the scan rate, A is the WE area, D is the redox active species diffusion coefficient, and C_0 is the redox active species concentration in the bulk solution.[62] Since the i_p is directly proportional to the electrode area, any changes on the electrode surface can be monitored by CV.

During this work, we used CV for monitoring the gold surface functionalization. We used the gate electrode as WE, Ag/AgCl as RE and a platinum wire as CE. The redox probe of choice was 5mM $K_3[Fe(CN)_6]$ solution and the supporting electrolyte was typically 1M KCl. Measurements were performed using a CH Instrument potentiostat 760c model at room temperature.

2.3.2 Electrochemical Impedance Spectroscopy

Electrochemical Impedance Spectroscopy (EIS) is a widely used technique because it allows the study and comprehension of electrochemical processes occurring at the electrified interface. EIS excites the electrochemical system at different frequencies upon the application of a small-amplitude potential. The response of the system to this perturbation, namely the current or potential, is measured to calculate a transfer function that represents the electrochemical Impedance (Z) of the electrochemical cell. Z is a complex number which is dependent on frequency, comprising a real component Z', the resistance, and an imaginary part Z'', the reactance (**Figure 2.11 C**).[61,65] This technique can be either faradaic EIS (*f*-EIS) working with a redox probe in solution or immobilized on the working electrode, or non-faradaic EIS (*nf*-EIS), in the absence of redox species. Both techniques have been extensively used to realize biosensors. The *f*-EIS detection mechanism relies on sensing the redox reaction occurring at the electrode/electrolyte "interfacial layer" upon the application of small direct current (DC) perturbation. The response can be quantified as changes in the charge transfer resistance (R_{ct}) and changes in impedance (Z) due to a perturbation of the equilibrium potential as consequence of adsorption of molecules at the electrode surface. Meanwhile, the *nf*-EIS measures changes in the double layer capacitance (C_{dl}) value as a result of the insulating properties of the biolayer bearing the biorecognition unit on the electrode surface, and its response to the analyte binding.[66]

One of the main advantages of EIS is the possibility of studying several electrochemical processes from one single measurement, unlike other electrochemical techniques such as CV. It is clear that both techniques are complementary and the choice of which one to use will depend on the system one wants to characterize. For instance, during this work we used *f*-EIS to monitor the gate functionalization after the total passivation with SAM (step 1 in most of the protocols here used), since the CV would not be able to provide more information after the electrode full coverage; in this case we used $[Fe(CN)_6]^{3-}/[Fe(CN)_6]^{4-}$ as redox couple. Additionally, we used *nf*-EIS to investigate the contribution of the analyte IL-6 to the sensor surface in terms of changes in capacitance (Chapter 3). Measurements were performed in a two-electrodes electrochemical setup, using Pt wire as CE/RE and the functionalized gold gate as WE and 50 mM Phosphate Buffer solution (pH 7.4) as electrolyte. The *nf*-EIS was acquired by applying a fixed potential of +100 mV *vs.* Pt, with an amplitude of 5 mV. In order to better quantify the *nf*-EIS response, the complex capacitance (C) have to be determined from the high impedance values by means of:

$$C = -\frac{Z''}{\omega|Z|^2} - \frac{Z'}{\omega|Z|^2} \quad (2.3)$$

where $\omega = 2\pi f$.

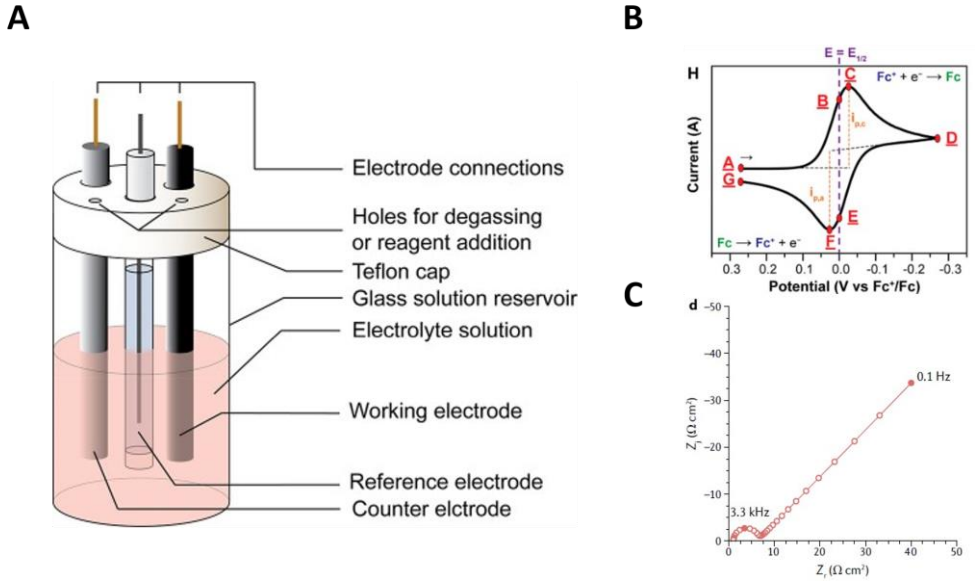

Figure 2.11. A) Schematic representation of an electrochemical cell. **B)** typical CV duck shape, showing the cathodic and anodic current peaks. **C)** Typical Nyquist plot of EIS measurements. A) and B) were adapted from Elgrishi N. *et al.*,[64] and C) was adapted from Wang S. *et al.*[61]

2.4 ELECTRICAL CHARACTERIZATION

EGOTs electrical characterization typically encompasses two sets of measurements: 1) The **transfer curves** (I_{DS} *vs.* V_{GS} with V_{DS}=constant), from which one can determine the following figures of merit: the threshold voltage (V_{th}), ON/OFF ratio, and the transconductance (g_m). 2) The **output curves** (I_{DS} *vs.* V_{DS} with V_{GS}=constant), which provide information about the transistor regime, and help choosing the right V_{DS} at which to record the transfer curves, according to whether one wants to operate the devices in the linear or saturation regime. One might also consider the leakage current (I_{GS} *vs.* V_{GS}) as a needed characterization measurement to ensure that its magnitude is negligible compared to the drain current (at least by two orders of magnitude).[67] Inspection of the gate current can yield information on redox processes possibly taking place at the gate electrode.

During this work, electrical measurements were performed inside a Faraday cage that is earth grounded, protecting the device from light due to possible optical sensitivity and minimizing the background electrical noise. The measurement instrumentation was the source-measurement unit (SMU) Agilent B291224 (California, U.S.A.), this instrument works with high-resolution (up to10 fA/100 nV) and low-noise. The SMU can simultaneously apply

potential between the Gate and Source (V_{GS}), and between the Drain and Source (V_{DS}) through two independent channels. It can also record the current from each channel (I_{GS} and I_{DS}) using custom-designed software. The drain, source and gate electrodes were connected using high-precision spring-probe contacts. The electrical setup is shown in **Figure 2.12**. The transfer curves were recorded by sweeping the gate potential (V_{GS}), controlling parameters such as scan rate, aperture, delay per step, among others, with the software, and by keeping a fixed drain potential (V_{DS}).

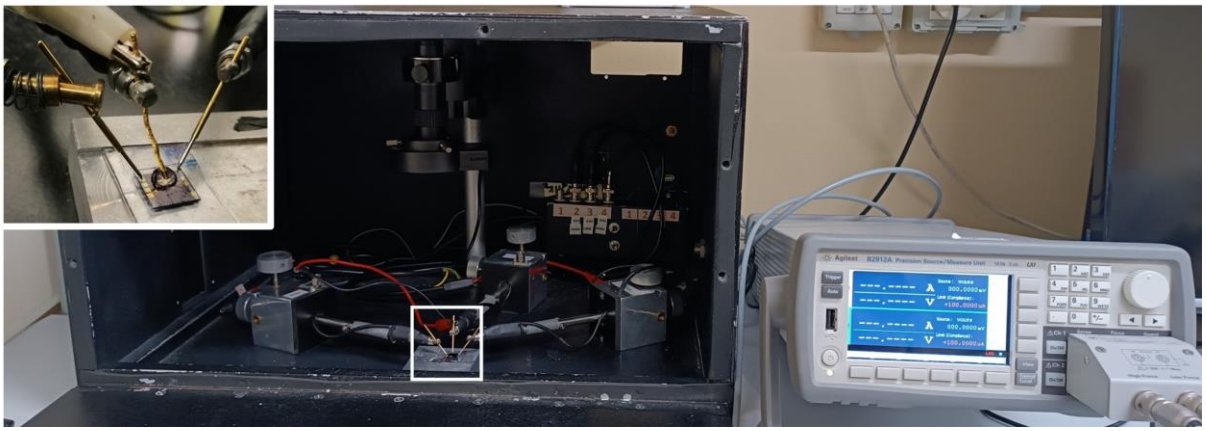

Figure 2.12. Electrical measurement instrument SMU (right) and Faraday cage (left). In the inlet a zoom of the device with its electrical connections.

The electrolyte of choice was either 50 mM Phosphate Buffer solution (pH 7.4) or 1x PBS (pH 7.4), emulating the physiological conditions, and it was contained in a Polydimethylsiloxane (PDMS) static cell, except for the I *vs.* time measurements for the OECT-based biosensor for the detection of anti-CMV pp65 (Chapter 5), in which measurements were performed in a flow-cell with the integration the sensing device into the microfluidics. For sensing measurements, the electrolyte was containing the target analyte for *in situ* detection.

The microfluidics used in Chapter 5 were produced by our collaborators Fabio Biscarini and Pierpaolo Greco at the Italian Institute of Technology (IIT, Ferrara) and University of Ferrara, respectively. These double sided adhesive microfluidic chambers had a thickness of 245 μm, having a 7 μm PET layer in between the two bi-adhesive layers. The adhesive material was chosen from the plethora of health care materials, taking into consideration its adhesive strength. The flexible microfluidics were produced by laser ablation. The design encompasses a 6.5 mm^2 window for the square gate electrode in the middle, and two holes, one at each side of the gate, for the inlet and outlet connectors (**Figure 2.13 A**). The electrolyte was flowed using a peristaltic pump at 10 rpm, the electrical connection together with the tubings are shown in **Figure 2.13 B**.

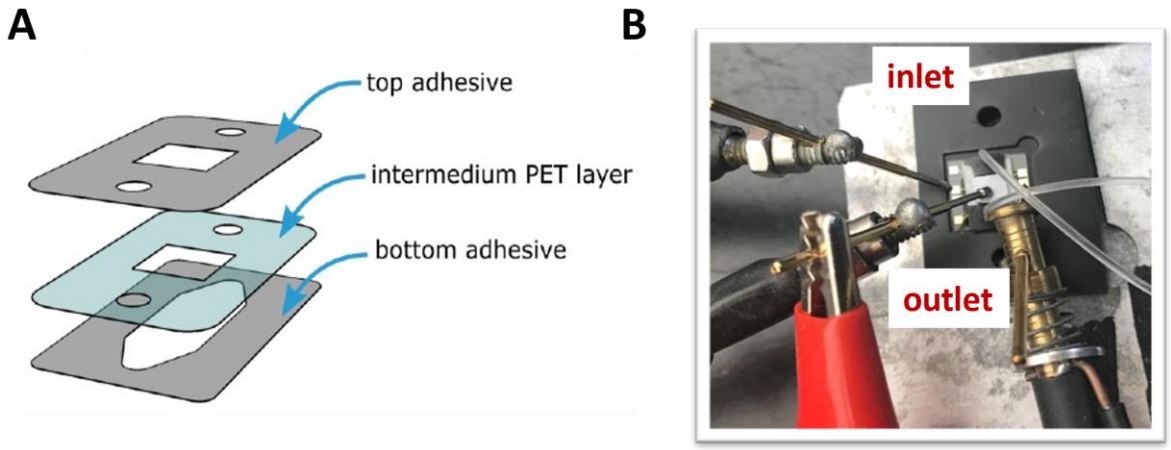

Figure 2.13. A) Flexible adhesive microfluidics design, adapted from Parkula V.[68] **B)** Assembled microfluidics with the electrical connections and the peristaltic pump tubings.

2.5 REFERENCES

[1] K. Kim, H. Yoo, E. K. Lee, *Polymers (Basel).* **2022**, *14*.

[2] S. Giannini, J. Blumberger, *Acc. Chem. Res.* **2022**, *55*, 819.

[3] J. Rivnay, S. Inal, A. Salleo, R. M. Owens, M. Berggren, G. G. Malliaras, *Nat. Rev. Mater.* **2018**, *3*.

[4] S. H. Kim, K. Hong, W. Xie, K. H. Lee, S. Zhang, T. P. Lodge, C. D. Frisbie, *Adv. Mater.* **2013**, *25*, 1822.

[5] J. E. Anthony, J. S. Brooks, D. L. Eaton, S. R. Parkin, *J. Am. Chem. Soc.* **2001**, *123*, 9482.

[6] C. D. Sheraw, T. N. Jackson, D. L. Eaton, J. E. Anthony, *Adv. Mater.* **2003**, *15*, 2009.

[7] P. Cosseddu, S. Lai, M. Barbaro, A. Bonfiglio, *Appl. Phys. Lett.* **2012**, *100*.

[8] M. M. Payne, S. R. Parkin, J. E. Anthony, C. Kuo, T. N. Jackson, **2005**, 4986.

[9] S. K. Park, S. Member, J. E. Anthony, T. N. Jackson, IEEE Electron Device Lett. **2007**, 28, 877.

[10] Y. Diao, B. C. K. Tee, G. Giri, J. Xu, D. H. Kim, H. A. Becerril, R. M. Stoltenberg, T. H. Lee, G. Xue, S. C. B. Mannsfeld, Z. Bao, *Nat. Mater. 2013 127* **2013**, *12*, 665.

[11] G. Giri, E. Verploegen, S. C. B. Mannsfeld, S. Atahan-Evrenk, D. H. Kim, S. Y. Lee, H. A. Becerril, A. Aspuru-Guzik, M. F. Toney, Z. Bao, *Nat. 2011 4807378* **2011**, *480*, 504.

[12] K. W. Chou, H. U. Khan, M. R. Niazi, B. Yan, R. Li, M. M. Payne, J. E. Anthony, D.-M. Smilgies, A. Amassian, *J. Mater. Chem* **2014**, *2*, 5681.

[13] Q. Zhang, F. Leonardi, S. Casalini, I. Temiño, M. Mas-Torrent, *Sci. Rep.* **2016**, *6*, 1.

[14] N. Lago, M. Buonomo, S. Imran, R. Bertani, N. Wrachien, M. Bortolozzi, M. G. Pedersen, A. Cester, *IEEE Electron Device Lett.* **2018**, *39*, 1401.

[15] D. T. James, J. M. Frost, J. Wade, J. Nelson, J. S. Kim, *ACS Nano* **2013**, *7*, 7983.

[16] C. Y. Lo, Y. Wu, E. Awuyah, D. Meli, D. M. Nguyen, R. Wu, B. Xu, J. Strzalka, J. Rivnay, D. C. Martin, L. V. Kayser, *Polym. Chem.* **2022**, *13*.

[17] G. Heywang, F. Jonas, *Adv. Mater.* **1992**, *4*, 116.

[18] Y. Wen, J. Xu, *J. Polym. Sci. Part A Polym. Chem.* **2017**, *55*, 1121.

[19] F. Jonas, J. T. Morrison, *Synth. Met.* **1997**, *85*, 1397.

[20] S. Zhang, P. Kumar, A. S. Nouas, L. Fontaine, H. Tang, F. Cicoira, *APL Mater.* **2015**, *3*, 14911.

[21] K. Tang, W. Miao, S. Guo, *ACS Appl. Polym. Mater.* **2021**, *3*, 1436.

[22] S. L. Bidinger, S. Han, G. G. Malliaras, T. Hasan, *Appl. Phys. Lett.* **2022**, *120*.

[23] Y. Cao, G. Yu, C. Zhang, R. Menon, A. J. Heeger, *Synth. Met.* **1997**, *87*, 171.

[24] L. Groenendaal, F. Jonas, D. Freitag, H. Pielartzik, J. R. Reynolds, *Adv. Mater.* **2000**, *12*, 481.

[25] J. Li, Y. Zhao, H. S. Tan, Y. Guo, C. A. Di, G. Yu, Y. Liu, M. Lin, S. H. Lim, Y. Zhou, H. Su, B. S. Ong, *Sci. Rep.* **2012**, *2*, 1.

[26] R. J. Kline, M. D. McGehee, E. N. Kadnikova, J. Liu, J. M. J. Fréchet, M. F. Toney, *Macromolecules* **2005**, *38*, 3312.

[27] J. Rivnay, L. H. Jimison, J. E. Northrup, M. F. Toney, R. Noriega, S. Lu, T. J. Marks, A. Facchetti, A. Salleo, *Nat. Mater.***2009**, *8*, 952.

[28] H. N. Tsao, D. Cho, J. W. Andreasen, A. Rouhanipour, D. W. Breiby, W. Pisula, K. Müllen, *Adv. Mater.* **2009**, *21*, 209.

[29] M. Socol, N. Preda, C. Breazu, A. Costas, G. Petre, A. Stanculescu, G. Popescu-pelin, A. Mihailescu, G. Socol, *Nanomater.***2020**, *10*, 2366.

[30] Y. Zhang, X. Yao, Y. Cui, *IEEE Sensors Lett.* **2023**, *7*.

[31] M. Higashinakaya, T. Nagase, H. Abe, R. Hattori, S. Tazuhara, T. Kobayashi, H. Naito, *Appl. Phys. Lett.* **2021**, *118*, 103301.

[32] R. Giridharagopal, J. Guo, J. Kong, D. S. Ginger, *ACS Appl. Mater. Interfaces* **2021**, *13*, 34616.

[33] Y. Zhang, Q. Zeng, Y. Shen, L. Yang, F. Yu, *ACS Appl. Mater. Interfaces* **2020**, *12*, 56216.

[34] T. T. K. Nguyen, T. N. Nguyen, G. Anquetin, S. Reisberg, V. Noël, G. Mattana, J. Touzeau, F. Barbault, M. C. Pham, B. Piro, **2018**.

[35] H. Xu, Y. Jiang, J. Li, B. S. Ong, Z. Shuai, J. Xu, N. Zhao, *J. Phys. Chem. C* **2013**, *117*, 6835.

[36] L. Shaw, Z. Bao, *Isr. J. Chem.* **2014**, *54*, 496.

[37] Y. Diao, L. Shaw, Z. Bao, S. C. B. Mannsfeld, *Energy Environ. Sci.* **2014**, *7*, 2145.

[38] J. Park, S. Lee, H. H. Lee, *Org. Electron.* **2006**, *7*, 256.

[39] "Spin Coating: Complete Guide to Theory and Techniques | Ossila," can be found under https://www.ossila.com/en-eu/pages/spin-coating, **n.d.**

[40] R. G. Larson, T. J. Rehg, in *Liq. Film Coat.*, Springer, Dordrecht, **1997**, pp. 709–734.

[41] G. De Luca, ab Emanuele Treossi, A. Liscio, J. M. Mativetsky, L. Mons Scolaro, V. Palermo, P. Samor ı, **n.d.**.

[42] D. Bharti, I. Varun, S. P. Tiwari, *Device Res. Conf. - Conf. Dig. DRC* **2016**, *2016-Augus*, 4.

[43] B. Burtscher, P. A. Manco Urbina, C. Diacci, S. Borghi, M. Pinti, A. Cossarizza, C. Salvarani, M. Berggren, F. Biscarini, D. T. Simon, C. A. Bortolotti, *Adv. Healthc. Mater.* **2021**, *2100955*.

[44] A. C. Donahue, M. Albitar, in *Recognit. Recept. Biosens.*, **2010**, pp. 221–248.

[45] E. K. Wujcik, H. Wei, X. Zhang, J. Guo, X. Yan, N. Sutrave, S. Wei, Z. Guo, *RSC Adv.* **2014**, *4*, 43725.

[46] F. Torricelli, D. Z. Adrahtas, Z. Bao, M. Berggren, F. Biscarini, A. Bonfiglio, C. A. Bortolotti, C. D. Frisbie, E. Macchia, G. G. Malliaras, I. McCulloch, M. Moser, T.-Q. Nguyen, R. M. Owens, A. Salleo, A. Spanu, L. Torsi, *Nat. Rev. Methods Prim.* **2021**, *1*.

[47] J. W. Lee, S. J. Sim, S. M. Cho, J. Lee, *Biosens. Bioelectron.* **2005**, *20*, 1422.

[48] E. Macchia, K. Manoli, B. Holzer, C. Di Franco, M. Ghittorelli, F. Torricelli, D. Alberga, G. F. Mangiatordi, G. Palazzo, G. Scamarcio, L. Torsi, *Nat. Commun. 2018 91* **2018**, *9*, 1.

[49] E. P. Diamandis, T. K. Christopoulos, *Clin. Chem.* **1991**, *37*, 625.

[50] M. Berto, E. Vecchi, L. Baiamonte, C. Condò, M. Sensi, M. Di Lauro, M. Sola, A. De Stradis, F. Biscarini, A. Minafra, C. A. Bortolotti, *Sensors Actuators, B Chem.* **2019**, *281*, 150.

[51] K. Solodka, M. Berto, D. Ferraro, C. Menozzi, M. Borsari, C. A. Bortolotti, F. Biscarini, M. Pinti, *Adv. Mater. Interfaces* **2022**, *9*.

[52] *Bioconjugate Techniques*, **1997**.

[53] F. Giess, M. G. Friedrich, J. Heberle, R. L. Naumann, W. Knoll, *Biophys. J.* **2004**, *87*, 3213.

[54] D. H. and S. A. Hochuli E., *J. Chromatogr.* **1987**, *411*, 177.

[55] R. C. Jorgenson, S. S. Yee, *Sensors and Acruofors* **1993**, *8*, 213.

[56] R. Hasler, C. Reiner-Rozman, S. Fossati, P. Aspermair, J. Dostalek, S. Lee, M. Ibáñez, J. Bintinger, W. Knoll, *ACS Sensors* **2022**, *7*, 504.

[57] A. T. Reiner, N. G. Ferrer, P. Venugopalan, R. C. Lai, S. K. Lim, J. Dostálek, *Analyst* **2017**, *142*, 3913.

[58] G. E. Perlmann, L. G. Longsworth, *J. Am. Chem. Soc.* **1948**, *70*, 2719.

[59] J. Dostálek, W. Knoll, *Biointerphases* **2008**, *3*, FD12.

[60] K. Schmidt, S. Hageneder, B. Lechner, B. Zbiral, S. Fossati, Y. Ahmadi, M. Minunni, J. L. Toca-Herrera, E. Reimhult, I. Barisic, J. Dostalek, *ACS Appl. Mater. Interfaces* **2022**, *14*, 55017.

[61] S. Wang, J. Zhang, O. Gharbi, V. Vivier, M. Gao, M. E. Orazem, *Nat. Rev. Methods Prim.* **2021**, *1*.

[62] B. J. F. Rusling, S. L. Suib, *Adv. Mater.* **1994**, *6*, 922.

[63] P. T. Kissinger, W. R. Heineman, *J. Chem. Educ.* **1983**, *60*, 702.

[64] N. Elgrishi, K. J. Rountree, B. D. McCarthy, E. S. Rountree, T. T. Eisenhart, J. L. Dempsey, *J. Chem. Educ.* **2018**, *95*, 197.

[65] B. Y. Chang, S. M. Park, *Annu. Rev. Anal. Chem.* **2010**, *3*, 207.

[66] C. Ibau, M. Md Arshad, S. C. Gopinath, M. M. Nuzaihan, M. Fathil, S. Arina Shamsuddin, **2020**.

[67] D. Gamota, J. Paul Brazis, *IEEE Std 1620-2008 (Revision IEEE Std 1620-2004) - Redline* **2008**, 1.

[68] V. Parkula, Organic Electronic Transistors for Biosensing, University of Modena and Reggio Emilia, **2018**.

3 IL-6 BIOSENSOR

This chapter describes and demonstrates the successful development of an EGOT-based biosensor for the detection of cytokine IL-6. In this study, we have demonstrated the applicability of these devices for thermodynamic analyses, wherein we have introduced a binding model, Frumkin isotherm, which has not been previously employed for describing biological systems, but highly corresponds with our data. This work has been published in P. A. Manco Urbina, M. Berto, P. Greco, M. Sensi, S. Borghi, M. Borsari, C. A. Bortolotti, F. Biscarini. *"Physical insights from the Frumkin isotherm applied to electrolyte gated organic transistors as protein biosensors" J. Mater. Chem. C* 2021, *9*, 10965.[1]

3.1 INTRODUCTION

3.1.1 Interleukin-6

Interleukin-6 (IL-6) is a small glycoprotein of 21-26 kDa and is one of the most relevant cytokines involved in the inflammatory response. IL-6 is a central mediator in the immune system, embracing a wide range of effects within the integrated immune response, with a pivotal role in immunocompetence.[2-4] Upon examining the role of IL-6, it is evident that one of its defining characteristics is pleiotropism - the ability to exhibit multiple biological functions. IL-6 was first identified in the 1970s as a soluble protein produced by T cells, triggering the differentiation of B cells into antibodies-producing cells. In the following years, several proteins with different biological activities were identified and cloned, to be then all recognized as the same protein, IL-6, highlighting its several biological effects.[5,6] IL-6 has both pro- and anti-inflammatory effects (**Figure 3.1**), participating in the innate immune response by triggering the secretion of chemokines to attract monocytes and/or macrophages to the target tissue and initiating the inflammatory response, as well as for its role in the activation and secretion of the acute phase proteins. Unlike many cytokines, IL-6 can act on distant cells via trans-signaling; a mechanism that is triggered by the ADAM17 protease under inflammatory conditions.[3] The physiological levels of IL-6 are around 1-5 pg mL^{-1}, which can be increased several thousand-fold in pathological conditions, even reaching the range of μg mL^{-1} in the case of lethal sepsis.[3,7] This has made IL-6 a good warning indicator of inflammatory processes, being considered a potential biomarker for several inflammation-related diseases such as cancer, autoimmune diseases, Alzheimer's disease, atherosclerosis, cardiovascular disorders, depression, gastrointestinal diseases, sepsis, aging, and infectious diseases such as the most recent COVID-19, as well as for treatment monitoring.[8]

Many of the above-mentioned diseases are inflammatory and age-related pathologies. As explained in Chapter 1, inflammaging is an age-related increase of pro-inflammatory mediators in the elderly, which is a risk factor for several diseases. Longitudinal studies have proved that IL-6, together with C-reactive protein (CRP), are good predictors of physical and cognitive performance, as well as of mortality in the elderly.[9–11] That is why it has been chosen as one of the targets for the development of ageing-biomarkers sensor during this work.

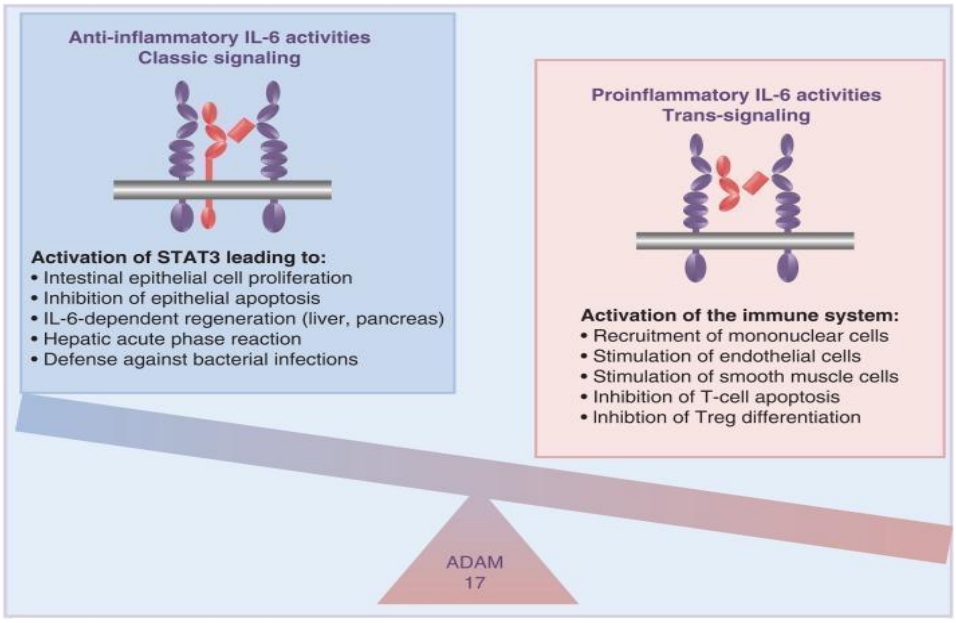

Figure 3.1. IL-6 pro- and anti-inflammatory activities. Classical *vs.* Trans-signalling and its implications in IL-6 bioactivity during inflammation.[3]

Although the scientific evidence supports the importance of an accurate quantification of this protein in the clinical context, it is still challenging since the physio-pathological levels of this cytokine are in the pM range, affected by dynamic secretion processes, and short half-lives. The current standard techniques for the detection of this protein and the many other cytokines are based on the optical immunosensors Enzyme-linked Immunosorbent Assay (ELISA) and Luminex. These techniques feature a typical limit of detection (LOD) of below 1 pg mL^{-1} (0.05 pM) and 20 pg mL^{-1} (1 pM) respectively.[12] Despite being very robust and reliable techniques, they require labeling, expensive equipment, trained personnel, relatively large sample volumes, and in addition they are quite time consuming. Therefore, there is still the need to develop biosensors with high sensitivity and selectivity for real-time monitoring of cytokines in biological samples, with the possibility to be implemented in the Point-of-Care (PoC) testing.

3.1.2 EGOT Family

Electrolyte Gated Organic Transistors (EGOTs) are rapidly emerging as an alternative to these techniques for their outstanding amplification capabilities of small biological signals. They feature many advantages such as operability in a liquid environment, biocompatibility and label-free sensing, fast response, and user-friendly with the possibility to be implemented at the Point-of-Care (PoC) testing.[13–17] The EGOT family encompasses two sub-classes: Electrolyte Gated Field Effect Transistor (EGOFET) and Organic Electrochemical Transistor (OECT), depicted in **Figure 3.2**. The working principle of both architectures is based on the

mix of ionic (electrolyte) and electric (OSC) responses to the bias applied between the gate and source and drain and source electrodes.[14,16,18–21] EGOTs have been widely used for analytical purposes as potentiometric biosensors, where the analyte is usually quantified in terms of concentration-dependent changes in the drain current (I_{DS}).[22–25] EGOT-based biosensors are endowed with biorecognition capabilities by immobilizing the biorecognition unit (e.g., antibodies, aptamers, among others) either at the gate or OSC interface. Since both interfaces are capacitively coupled, any changes in the electrochemical potential at the gate/electrolyte interface will lead to the modulation of the I_{DS}, therefore, the binding event will be transduced into an electrical signal.[18] Regarding specifically to OECTs, they have been largely preferred as amperometric sensors, where the analyte undergoes a redox reaction generating (directly or via a mediator) a faradaic current that is proportional to the analyte concentration.[16,21,26,27]

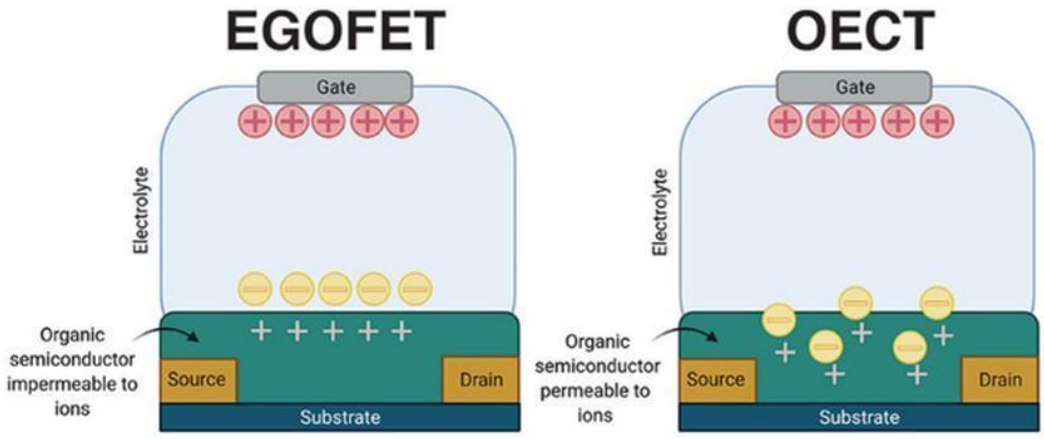

Figure 3.2. Schematic representation of EGOFET (left) and OECT (right) showing the OSC permeability to ions penetration.[18]

3.2 EGOT DEVELOPMENT

3.2.1 Transistor Fabrication

The architectures of choice were EGOFET and OECT, which were fabricated on quartz substrates featuring interdigitated drain and source electrodes, as previously described in Chapter 2.1. For the fabrication of EGOFET, the chosen TPs had a channel width/length (W/L) of 2000, whereas the one for OECT fabrication had a W/L of 50. The substrates were first cleaned following the next protocol: i) a first rinse with acetone to remove the photoresist layer and gently drying with nitrogen flow, ii) then a washing step in hot acetone (70 °C for 10 minutes), and iii) a final washing step in piranha solution (H_2SO_4:H_2O_2 1:1) for 1 minute at 150 °C, followed by iv) abundant rinsing with water and drying in nitrogen flow. The OSC used for the EGOFET fabrication was the small crystal TIPS-Pentacene diluted in hexane:toluene (20:80) solvent, deposited by spin coating at 600 rpm for 15 seconds and cured

in a solvent vapor rich environment at 60 °C for 30 minutes. The OECT was fabricated using the well-known polymer PEDOT:PSS, prepared adding 0.2 % of 3-(glycidyloxypropyl)trimethoxysilane (glymo) and 5 % of dimethyl sulfoxide, and finally diluted in water (1:5); the solution was then spin coated at 500 rpm for 3 seconds, followed by 2000 rpm for 20 seconds, and cured at 120 °C for 45 minutes.

3.2.2 Gate Functionalization

In order to endow the EGOT with biorecognition capabilities, the gold gate electrode was functionalized with anti-IL-6 antibodies by exploiting the carbodiimide crosslinker chemistry, described in more detail in Chapter 2.1.4. First, the gold wire was cleaned by immersion in 2.5 M KOH at 130 °C for 4 hours, followed by abundant rinsing with water, and then a final immersion in concentrated H_2SO_4 at 220 °C for 2 hours. The clean gate was abundantly rinsed with water and dried under nitrogen flow. Next, the gate functionalization protocol proceeded as follows: i) gate incubation in a mix of 11-mercaptoundecanoic acid: 6-mercaptohexanol (MUA:MCH 1:3) in ethanol for the formation of a first biolayer of SAM with terminal carboxylic groups, ii) immersion in 200 nM N-(3-dimethylaminopropyl)-N'-ethylcarbodiimide hydrochloride (EDC) and 50 mM N-hydroxysuccinimide (NHS) in water for 30 minutes, iii) gate incubation in 0.1 mg mL^{-1} anti-IL-6 antibody in 50 mM Phosphate Buffer pH 7.4 for one hour, iv) then in 0.5 M ethanolamine (ETA) in phosphate buffer for 30 minutes, v) and a final incubation step in 0.1 mg mL^{-1} bovine serum albumin (BSA) in phosphate buffer for 30 minutes. In the case of OECT-based sensors, this last step included 0.05% Tween20 in the BSA solution. The whole functionalization process was performed at room temperature (RT). The final device is illustrated in **Figure 3.3**.

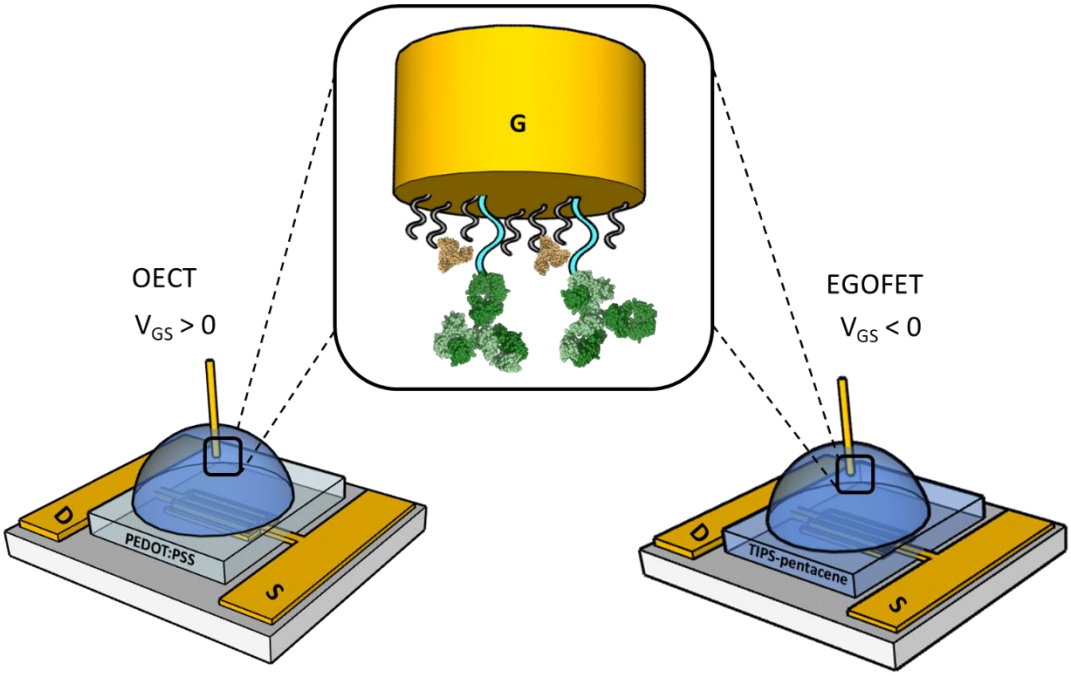

Figure 3.3. Schematic representation of the OECT and EGOFET architectures for IL-6 Detection. In the box on the top is zoomed in the gate functionalization.

3.2.3 Optical Validation of Functionalization Process

The gate functionalization was monitored by FO-SPR (Chapter 2). These experiments were performed in collaboration with Professor W. Knoll's group at the Austrian Institute of Technology (AIT). The real-time monitoring started with the FO functionalized with the mixed MUA:MCH SAM in 1x PBS, as can be seen in **Figure 3.4**. The optical signal is presented as a shift of the resonance wavelength (λ_{SPR}), this corresponds to changes on local refractive index, associated to molecular mass of the adsorbed biolayer on the gold surface. Measurements were performed in real-time, and through data analysis we can estimate the surface mass density (Chapter 2, eq. 2.1). The average of 4 experiments yielded surface coverage ϑ values of 261.7 ± 7.1 ng cm^{-2} for anti-IL-6 antibody, equivalent to $1.05(\pm 0.03) \times 10^{12}$ molecules cm^{-2}. The FO-SPR proved that this functionalization strategy has good reproducibility and is in line with that has been previously reported in the literature where ϑ ranges from 200 to 500 ng cm^{-2}.[28,29]

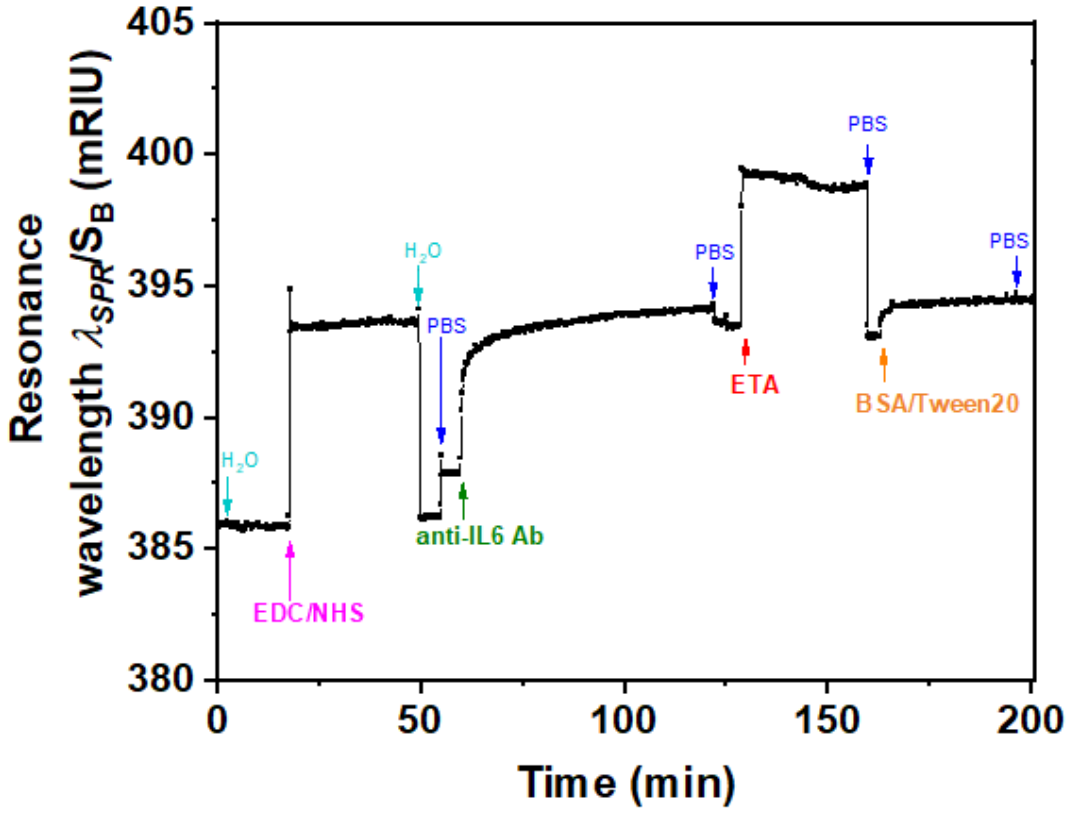

Figure 3.4. SPR kinetics for the gate functionalization starting from the FO already functionalized with the mixed SAM MUA:MCH. Experiments were performed first using H_2O as electrolyte, then moving to 1x PBS from the antibody step.

3.3 BIOSENSOR RESPONSE

3.3.1 Transfer Curves

The functionalized gold electrodes were used to gate both EGOFET and OECT devices operated as IL-6 biosensors, i.e. exposed to increasing concentrations of the target analyte, IL-6, in 50mM phosphate buffer solution pH 7.4, containing a constant concentration of 0.1mg mL^{-1} BSA (and 0.05 % Tween20 in the case of OECT-based biosensor). BSA was included to mimic the albumin concentration typically found in human plasma sample undergoing a 1:400 dilution. Electrical measurements were performed inside a Faraday cage with an Agilent B2912A Source Measure Unit by applying a sweeping gate-source potential (V_{GS}) and a fixed drain-source potential (V_{DS}). In the case of EGOFET, V_{GS} sweeping potential was from -0.1 V to -0.6 V, and in the case of OECT, V_{GS} was varied from -0.2 V to 0.4 V. Since both channel materials are p-type semiconductors, holes are the charge carriers, therefore a negative V_{DS} is required: we applied V_{DS}= -0.2 V in both cases. Before the sensing experiment, we assessed

the device stability by repeatedly acquiring transfer curves until stabilization, i.e. until the last five transfer curves recorded were superimposable.

Figure 3.5 displays the typical responses of OECT (**A**) and EGOFET biosensor (**B**) to increasing concentration [IL-6]. In both device architectures the drain current increases with increasing [IL-6], as a consequence of the specific binding of IL-6 to the antibodies immobilized on the gate electrode. This behavior was consistently observed in all the five devices that were characterized for each architecture.

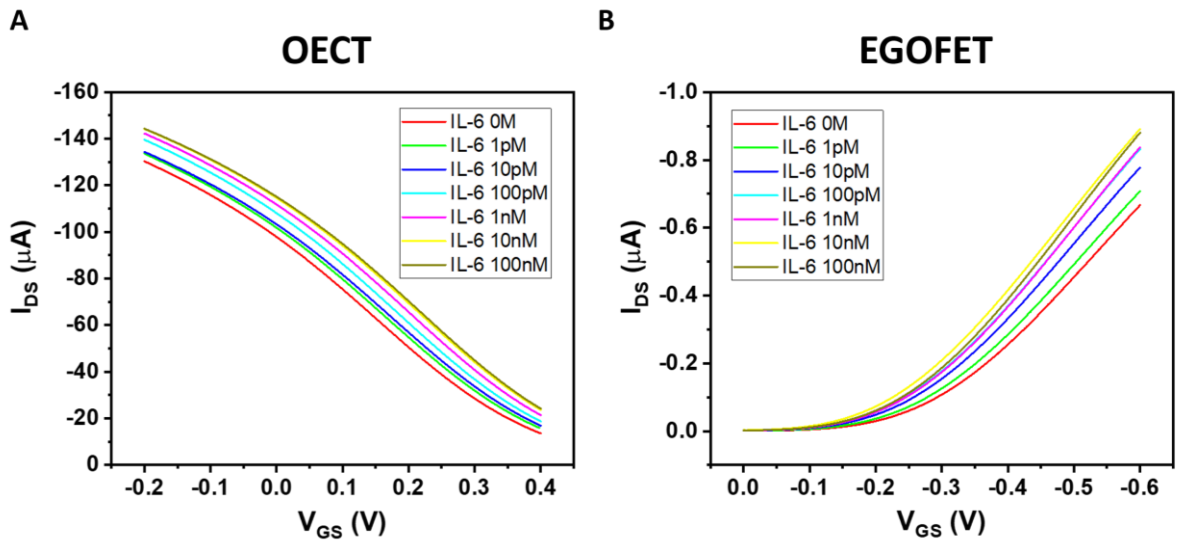

Figure 3.5. Transfer characteristics of EGOT-based biosensor upon exposure to increasing concentrations of IL-6 in 50mM phosphate buffer solution, containing a constant concentration (0.1 mg mL^{-1}) of BSA (in the case of OECT it also contained 0.05 % (v/v) Tween20). Electrical measurements were performed in a Faradaic cage with a sweeping gate voltage from -0.2 V to 0.4 V and from 0 to -0.6 V in the case of OECT **(A)** and EGOFET **(B)**, respectively. In both cases, the drain voltage was kept constant at -0.2 V.

The observed current increase is in line with previously reported OECT-based detection of IL-6.[24] We explain the observed current shift in **Figure 3.5** upon IL-6 biorecognition with an intuitive physical-chemical argument based on the changes of the potential drop at the gate/electrolyte and electrolyte/channel interfaces upon IL-6 binding. We treat the mixed mercaptoundecanoic/6-mercaptohexanol SAM and the protein layer (made either of Anti-IL-6 or Anti-IL-6/IL-6) as continuous in-series dielectric layers, hence a linear decay of the potential with the distance occurs across each layer. In the diffuse layers, one outside the protein layer at the gate and the other at the electrolyte/channel interface, the potential decays exponentially following Gouy-Chapman model.

The IL-6 molecule is expected to be negatively charged at the pH under the present experimental conditions (*vide infra*). Therefore, binding of an IL-6 molecule to its antibody

will lower the electrochemical potential of the electrolyte yielding a smaller potential drop across the electrolyte/channel interface. This is equivalent to the application of a more negative potential difference between gate and source, which would increase the charge carrier density in the channel. As a consequence, in OECT more IL-6 binds the gate electrode, more current in the channel is output as the result of less de-doping of PEDOT:PSS. The same argument, although with reverted potential at the gate electrode, holds for EGOFET as the decrease of electrochemical potential of the electrolyte due to IL-6 binding to the protein layer yields a more negative potential at the electrolyte/OSC channel and hence to a current increase due to increased "doping". Albeit its simplicity, our explanation provides a first useful hint from the experimental observation of the change of the transfer curves upon exposure to a target analyte: the net charge (negative if current increases, else positive if current decreases) that is built at the protein layer upon adsorption.

Measurements of capacitance by non-faradaic electrochemical impedance spectroscopy (*nf*-EIS, explained in more detail in Chapter 2.3.2) were performed to assess the capacitance contribution of the analyte binding to the gate surface. These measurements were performed in a two-electrodes set-up, using Pt wire as counter/reference electrode and 10mM phosphate buffer pH 7.4 as electrolyte. The non-faradaic electrochemical impedance spectroscopy was acquired by applying a fixed potential of +100 mV *vs.* Pt, with an amplitude of 5 mV, and converted into complex capacitance using the equation 2.3 (Chapter 2.3.2), adapted from C. Ibau *et al.*[30] **Figure 3.6** displays the changes in complex capacitance, showing an increase in the capacitance in the presence of IL-6 with respect to the same surface not exposed to the cytokine, in accordance with an increase of negative charge induced by the binding of IL-6 to the surface

We point out that the net charge of the target analyte cannot be the only determinant to the shifts in the potential drop upon target binding: the nature of the biorecognition unit (e.g. its charge, electrostatic potential, solvation sphere, dipole moment) the presence of a self-assembled monolayer on the gate as well as the device channel can also play a role, albeit we disregard it here.

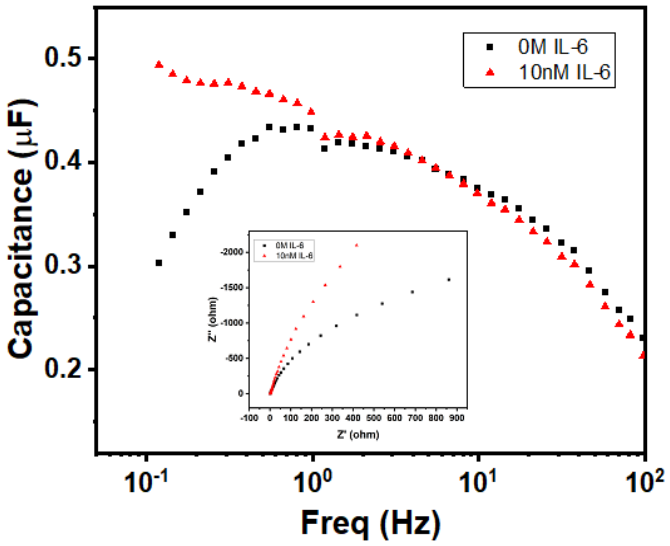

Figure 3.6. Complex capacitance of the gate electrode, at 0 M (black) and 10 nM IL-6 (red), determined by non-faradic electrochemical impedance spectroscopy. In the inset the relative Nyquist plot. The measurements were performed in 10 mM PBS pH 7.4, applying a potential of +100 mV *vs.* Pt electrode, with an amplitude of 5 mV.

3.3.2 Response Quantification

We now construct the dose curves at any V_{GS} value by calculating the signal *S*, corresponding to the current change normalized by the current in the absence of analyte, vs the concentration *c* of the target analyte. In **Figure 3.7 A**, we show two examples of the dose curve, one $S(c, V_{GS} = +0.3\ V)$ for OECT (black squares), as this V_{GS} value lies close to the maximum transconductance region in **Figure 3.5A**; the other $S(c, V_{GS} = -0.3\ V)$ for EGOFET (red circles), as V_{GS} lies in the sub-threshold region that yields the largest signal *S viz.* where the sensor exhibits the highest sensitivity.[23,31–33] Both dose curves exhibit monotonic trends *vs. c* then tends to saturate for *c* greater than 10 nM. Thus, our biosensors respond across four orders of magnitude of *c*, from 1 pM to 10 nM, these values being within the significant patho-physiological range.

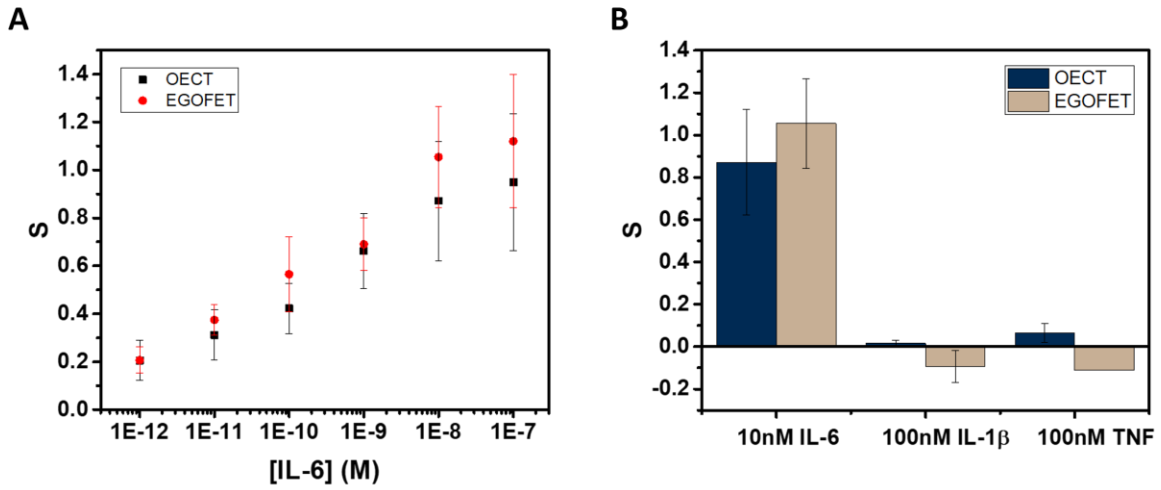

Figure 3.7. A) Dose curve for OECT (black squares) and EGOFET (red circles) at V_{GS} values of +0.4 V and -0.3 V, respectively, and at a fixed V_{DS} = -0.2 V. **B)** Histogram comparing the sensor response to the analyte and to other two possible interfering cytokines, IL-1β and TNFα.

3.3.3 Control Experiments

To assess the selectivity of both EGOFET and OECT biosensors, we performed control experiments by exposing gate electrodes functionalized with anti-IL-6 antibodies to a high concentration (100 nM) of two potentially interfering cytokines, namely IL-1β and TNF-α. The results displayed in **Figure 3.7 B**, show that the signal *S* for non-specific targets is about ten times lower than that for 10 nM IL-6. One way to safely estimate the limit of detection (LOD) comes from the control, by taking its average signal and adding three times the standard deviation. In this work, we took the average of TNF-α signal since it gave the highest signal for both architectures, this yielded in LOD of 0.3 pM and 0.04 pM for OECT and EGOFET, respectively.

3.4 BINDING MODELS

In this section, we want to introduce the different adsorption isotherm models that were used to analyze the data in terms of dose curves. The use of these adsorption isotherm models can help us to shed light on the thermodynamic aspects of the phenomena occurring at the gate/electrolyte interface. In general terms, an adsorption isotherm is a curve that describes the universal phenomenon of the transfer of a substance from a mobile phase (liquid or gas) to a solid phase at a constant temperature and pH. The adsorption equilibrium constant can be defined as the ratio between the amount of adsorbate in the solid phase and the remaining in the mobile phase.

The analysis of these isotherms can provide information about the adsorption mechanism, the surface properties such as the maximum adsorption capacitance, as well as the affinity of the adsorbent.[34,35]

Here we introduce the two most common isotherms applied to biosensing, Langmuir and Hill isotherms, as well as the Frumkin isotherm, which, until our knowledge, has never been applied before to the interpretation of antigen binding to a surface-immobilized antibody.

3.4.1 Langmuir Isotherm

Langmuir isotherm is one of the most used isotherms, even within the organic electronics community. It was proposed in 1916 by Irving Langmuir to describe the adsorption of gases onto activated carbon surfaces.[36] This model explains a simple adsorption process that disregards the influence of interactions between the adsorbed molecules. Essentially, each binding site (adsorbent) can bind one molecule, with equal affinity, constant enthalpies and activation energies, and with no steric impedance, all of them independent of the number of bound molecules.[34,37]

Based on this assumption, the Langmuir isotherm can be expressed as:

$$S \propto \theta = \frac{K_a c}{1+K_a c} \tag{3.1a}$$

That can be recast as:

$$K_a c = \frac{\theta}{(1-\theta)} \tag{3.1b}$$

where S is the measured signal, explained above, which can be transformed into surface coverage (ϑ), K_a is the equilibrium constant, and c is the free target species concentration.

We point out that, differently from the common practice especially adopted in biochemistry, being K_a dimensionless, the concentration c in Eq. (3.1a) and following, must be normalized by $[c^\circ] = 1$ M, *i.e.* $c = [c]/[c^\circ]$. Thus, the fitting of the dose curve yields a quantification of the affinity of the recognition group towards the target through the value of K_a, and hence gives an indication of the specificity of the sensing device.

3.4.2 Hill Isotherm

Hill isotherm is a 2-parameter equation isotherm. Although initially developed to describe the (anti)cooperative binding between molecules in solution, it can be applied to the adsorption of a species onto a homogeneous solid phase. In this regard, the adsorption of a molecule could affect, positively or negatively, the adsorption of the following molecules.[38,39] The non-linear form is written as:

$$S \propto \theta = \frac{{K_a}^{\alpha} c^{\alpha}}{1+{K_a}^{\alpha} c^{\alpha}} \quad (3.2a)$$

That can be recast as:

$${K_a}^{\alpha} c^{\alpha} = \frac{\theta}{(1-\theta)} \quad (3.2b)$$

which is very similar to Eq (3.1), Langmuir isotherm, but includes the Hill parameter α, which determines the cooperativity of the binding event: α>1, positive cooperativity, α=1, no cooperativity (Langmuir situation), α<1, negative cooperativity.[40]

Hill isotherm is strictly heuristic and care should be taken when the interpretation of α values in terms of (anti)cooperative binding events is given for α (smaller) larger than 1. A more consistent justification for the adequacy of Hill model can be given by invoking multiple equilibria involving probe, target and the bound pair. Indeed, it was shown that the exponent α = 1 (corresponding to a Langmuir-like process) can decrease down to 0.5,[41] or even take values α > 1.[42,43] Therefore, the Hill isotherm disguises intertwined multiple equilibria that may synergically either increase or decrease the dependence on the concentration.

3.4.3 Frumkin Isotherm

The Frumkin isotherm is well-known in the electrochemistry community, but it has not been applied yet to organic electronics. It was originally proposed to describe the adsorption of molecules on electrified interfaces, taking into consideration the interaction among the adsorbed molecules.[44,45] It is expressed as:

$$K_a c = \frac{\theta}{(1-\theta)} e^{-g'\theta} \quad (3.3)$$

the Frumkin parameter *g'* is proportional to $\delta\Delta G^{\circ}_{ads}/\delta\theta$ which relates the change of the free energy ΔG°_{ads} due to the binding event. This Frumkin parameter correlates with the attractive or repulsive forces between the adsorbed target-probe pairs, which is expressed in terms of *g'* positive or negative, respectively. Consequently, when *g'*>0, the attractive interactions lead to an increase in ϑ with increasing concentrations with respect to the case where lateral interactions are negligible, whereas when *g'*<0, the repulsive interactions lead to a smaller increase of ϑ with increasing concentration than in the absence of solute-solute lateral interactions. Finally, when *g'* equals to zero, there are no electrostatic interactions and Frumkin turns into the Langmuir model.[40,45]

3.5 BINDING THERMODYNAMIC ANALYSIS

3.5.1 Hill and Langmuir models

It is now convenient, for the sake of aligning the discussion to the isotherms introduced above, to renormalize the signal S to its plateau value, that we term S_{max}. For this, we assume that S_{max} lies 5% above the experimentally observed maximum. We chose this as plateau value to make our dataset to fall into a representative 95% of the whole statistical set. Then, we calculate the coverage θ as the ratio $\theta = S/S_{max}$, thus transforming the dose curve S *vs.* [IL-6] into the θ *vs.* c curve.

We compare the different isotherm models by fitting θ *vs.* c data from both OECT and EGOFET with Langmuir (Eq. 3.1a) and Hill (Eq3.2a) models. Then, we reverse the scheme and fit c *vs.* θ with Langmuir (Eq. 3.1b), Hill (Eq. 3.2b) and Frumkin (Eq. 3.3) isotherms. We are aware that the reverse fitting strictly holds provided the relative errors on θ and c are comparable.[46] We assess the models being used by means of the reduced χ^2, *viz.* χ^2 divided by the number of degrees of freedom which is the number of data minus the number of fitting parameters. The results are shown in **Figure 3.8** top and reported in **Tables 3.1a** and **3.1b**.

Langmuir isotherm, either as from Eq. 3.1a (continuous blue line in **Figure 3.8 A** and **B)** and Eq. 3.1b (dotted blue line in **Figure 3.8 A** and **B**), does not yield a satisfactory fitting both with OECT (**Figure 3.8 A**) and EGOFET (**Figure 3.8 B**), which hints to the fact that the simple assumption behind this model of independent adsorption events does not hold in the present experiment. We tried to use the Hill equation instead, which turns out to fit much better our experimental data, especially for OECTs, when used in the form 3.2a (continuous black line in **Figure 3.8 A** and **B**), whereas does not fit adequately in the form 3.2b (dotted black line in **Figure 3.8 A** and **B**) unless one of the two fitting parameters is held constant. This implies that the χ^2 function from Eq. 2b is ill-behaving, as it will disregard the residuals from the smallest concentrations. This occurrence is common to most of the fits c *vs.* θ because the concentration data span four orders of magnitude and the weight of the largest values is predominant. In order to overcome this numerical artifact, we perform the fitting of ln c *vs.* θ (**Figure 3.8** bottom). This scheme yields a better balanced fit with Hill equation (dashed black lines in **Figure 3.8 C** and **D**), whereas the Langmuir fit still reveals to be inadequate (dashed blue lines in **Figure 3.8 C** and **D**).

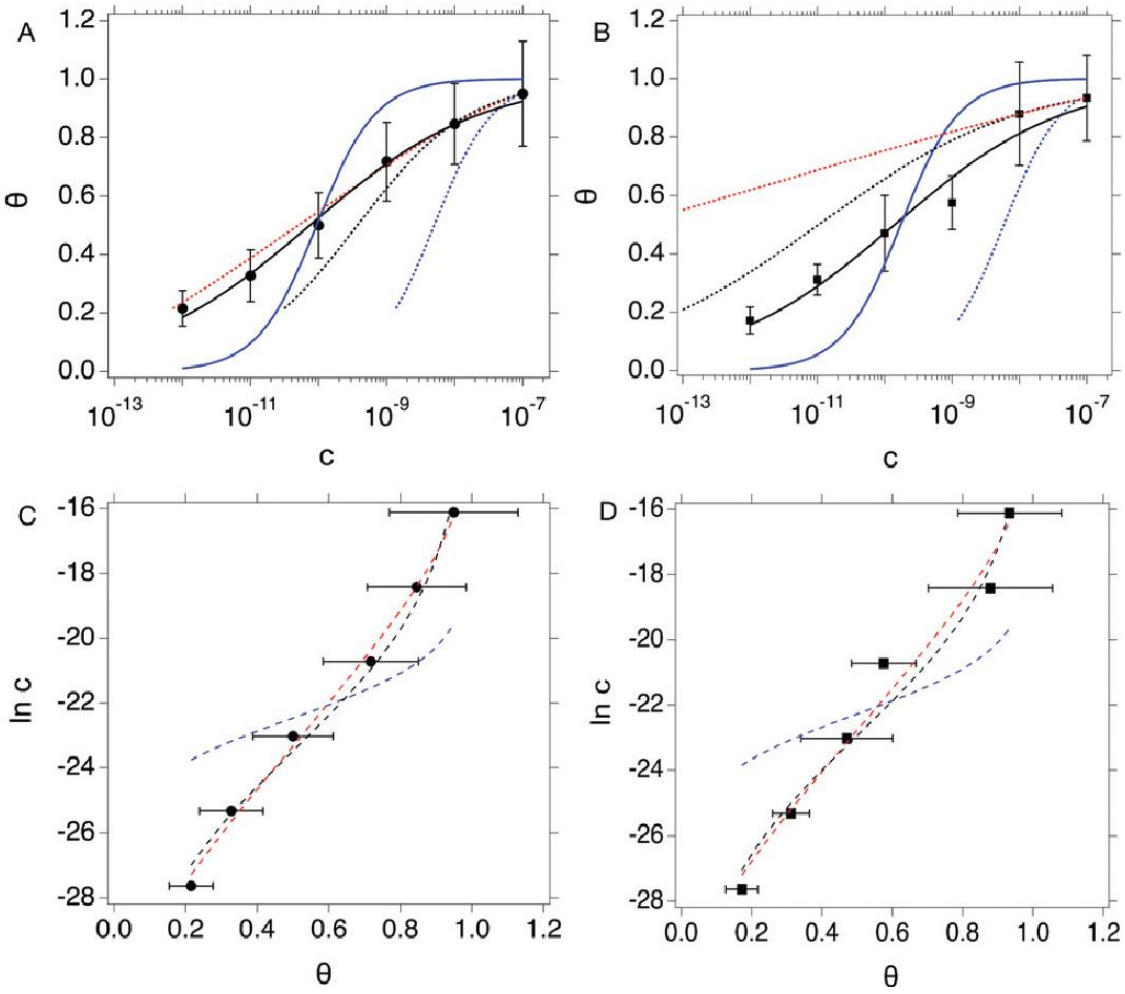

Figure 3.8. Dose curve plots expressed as θ *vs. c* for OECT **(A)** and EGOFET **(B)**. Continuous blue and black lines are fit to the Langmuir (Eq (3.1a)) and Hill (Eq (3.2a)) isotherms. Dotted blue, black and red lines are fit of the *c vs.* θ plot to the Langmuir (Eq (3.1b)), Hill (Eq (3.2b)) and Frumkin (Eq (3.3)) isotherms. Dose curve plots expressed as ln *c vs.* θ plots for OECT **(C)** and EGOFET **(D)**. Dashed blue, black and red lines are fit to the Langmuir, Hill and Frumkin isotherms. Error bars represent the associated standard error of the mean SEM.

Figure 3.8.

A further consideration concerns the result of fitting with Hill isotherm, that yields Hill exponent α values well below 0.5. Specifically, fitting θ *vs. c* with Eq. 3.2a yields α=0.344 (± 0.019) for OECT and α=0.341 (± 0.045) for EGOFET; fitting ln *c vs.* ϑ from the logarithm of Eq. 3.2b yields α=0.368(± 0.021) for OECT and α=0.382(± 0.034) for EGOFET. Such a small α value would be interpreted as the result of highly anti-cooperative binding event, and lead to extremely low $K_H = K_a^{\alpha}$ values ($K_H = 3.0 \times 10^4$ and 2.3×10^4 for OECT and EGOFET, respectively). We contend that these values hardly apply to a physically-sound description of surface-bound antibody and its antigen.

Table 3.1. (a) Best fit parameters for OECT (see Fig. 3.8 A and C) with estimated errors (in parenthesis) and estimator of goodness-of-fit. (b) Best fit parameters for EGOFET (see Fig. 3.8 B and D) with estimated errors (in parenthesis) and estimator of goodness-of-fit.

	Langmuir	Hill	Reverse Langmuir	Reverse Hill	Reverse Frumkin	Reverse Lang-muir logarithmic	Reverse Hill logarithmic	Reverse Frumkin logarithmic
(a)								
K_a (10^{12})	1.08 (±0.70) × 10^{-2}	1.35 (±0.22) × 10^{-2}	2.01 (±0.21) × 10^{-4}	2.70 (±0.42) × 10^{-3}	3.5771 (± 0.37)	5.7 (±6.4) × 10^{-3}	1.58 (±0.39) × 10^{-2}	1.44 (±0.49)
α	N/A	0.344 (±0.019)	N/A	0.523 (±0.014)	N/A	N/A	0.368 (±0.021)	N/A
g'	N/A	N/A	N/A	N/A	−10.38 (± 0.11)	N/A	N/A	−9.34 (±0.52)
Reduced χ^2	0.0316	0.0006	1.0206 × 10^{-16}	0.434 × 10^{-18}	1.3667 × 10^{-20}	7.5503	0.3075	0.1149
(b)								
K_a (10^{12})	5.80 (±4.26) × 10^{-3}	7.16 (±2.72) × 10^{-3}	1.70 (±0.31) × 10^{-4}	9.66 (±1.88) × 10^{-2}	1.34 (± 1.1) × 10^{8}	4.75 (±5.30) × 10^{-3}	9.19 (±3.34) × 10^{-3}	6.09 (±1.69) × 10^{-1}
α	N/A	0.342 (±0.045)	N/A	0.287 (±0.006)	N/A	N/A	0.382 (±0.034)	N/A
g'	N/A	N/A	N/A	N/A	−30.0 (±0.9)	N/A	N/A	−8.71 (±0.45)
Reduced χ^2	0.0393	0.0034	2.898 × 10^{-16}	2.3752 × 10^{-19}	2.5964 × 10^{-19}	7.4581	0.7356	0.5765

3.5.2 Frumkin Isotherm

In order to assess whether one's dataset exhibits Frumkin-like behaviour, it is common practice to fit the linearized data $ln\left[\frac{\theta}{c(1-\theta)}\right] = lnK_a + g'\theta$ to obtain the parameters K_a and g' from the intercept and slope of the best fit line. In the following, we perform non-linear fitting of *c vs.* θ directly from Eq. 3.3 keeping both K_a and g' free variational parameters. The best fit curves are also shown in **Figure 3.8 A** and **B**. We notice that the fit of the OECT data is excellent (dotted red line in **Figure 3.8 A**), whereas the fitting of EGOFET data (dotted red line in **Figure 3.8 B**) exhibits the bias towards the higher concentrations like Hill model. For EGOFET, it is necessary to perform the fitting of the *ln(c) vs.* θ to converge properly (dashed red lines in **Figure 3.8 A** and **B**).

We now comment on the values of the fitting parameters obtained from Frumkin equation. First, we discuss the association constant K_a. For OECT at V_{GS} = +0.3 V, we find K_a = 3.58(± 0.37) x10^{12}, whereas by fitting the logarithmic form of Eq. 3.3, we obtain K_a = 1.44(± 0.49) x10^{12}. For EGOFET at V_{GS} = -0.3 V, the fit converges to physically sound values of the parameters only for the logarithmic form Eq. 3.3 for K_a = 6.09(± 1.69) x10^{11}. The association constant values are in line with, though slightly higher, for IL-6 binding to antibodies.[47–49]

From now on, we discuss only the values obtained from the logarithmic form of eq. 3 which resulted into the most stable fitting functional. Converting K_a values into free energy of binding as:

$$-RTln(K_a) = \Delta G°(V_{GS}) = \Delta G°_b + \Delta G°_e(V_{GS}) \qquad (3.4)$$

yields $\Delta G°$ = -69(±1) kJ/mol and -67(±1) kJ/mol for OECT and EGOFET.[50–52] We infer that the reverted logarithmic fitting with Frumkin isotherm yields K_a values more consistent than those obtained with the Hill model.

Since the association constant depends on V_{GS}, we analyse its behaviour at different voltage values. In **Figure 3.9 A** we overlay the K_a values extracted from *ln(c) vs.* θ for OECT (V_{GS} values from -0.1 V to 0.4 V, red squares) and those extracted for EGOFET (V_{GS} values from -0.3 V to -0.6 V, red circles).

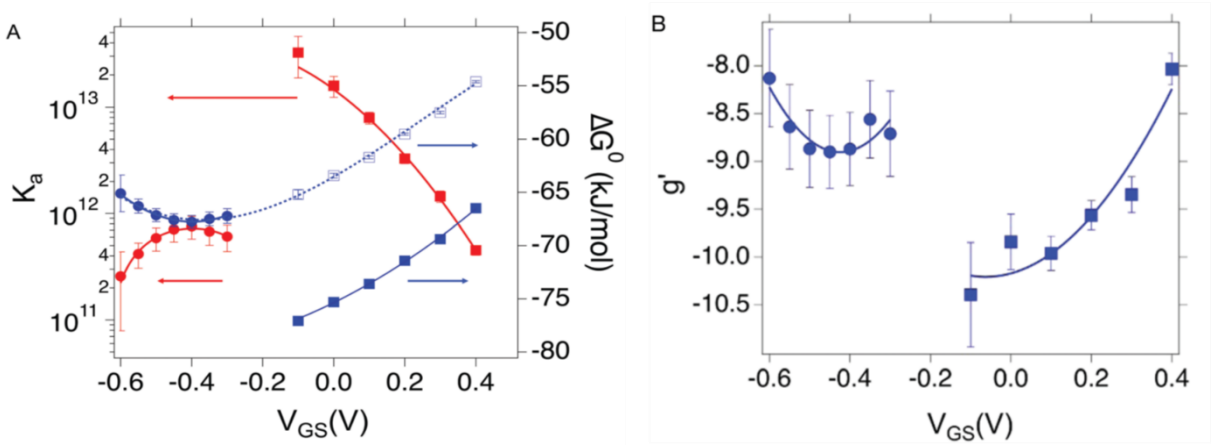

Figure 3.9. A) The dependence of K_a, represented by red squares and red circles respectively for OECT and EGOFET, as well as its corresponding $\Delta G°$, denoted by blue solid squares and blue circles for OECT and EGOFET, respectively, were analyzed with respect to V_{GS}. **B)** The dependence of g', represented by blue squares and blue circles for OECT and EGOFET, respectively, was studied as a function of V_{GS}. In both panels, the continuous lines were determined by fitting a parabolic function to each dataset, where the dotted blue line in panel A is the best fit with Eq (3.5). The error bars in the figures represent the estimated errors from the best fit of the *ln(c) vs.* θ curves at each V_{GS} value.

Remarkably, in OECTs K_a values span two decades in a V_{GS} range as small as 0.5 V, whereas in EGOFET, K_a changes only four times in a V_{GS} range of 0.3 V. A simple explanation is that for EGOFET in the relevant voltage range the electrode remains in a region of electroneutrality (or modest charge and/or dipole build up), while in OECT the charge/dipole build up is substantial thus making the V_{GS} effects more sizable. In support of this argument, we notice that a vertical translation of the OECT K_a values in the logarithmic scale (hence a re-scaling by a constant factor in the linear scale) would lead to alignment of the two branches (red circles and empty squares) into a continuous variation *vs.* V_{GS}.

We rationalize this by converting the K_a values into the association free energy $\Delta G°$ shown as blue markers on the right axis of **Figure 3.9 A**. The gap between the two branches (full circles and full squares) in the proximity of V_{GS} = -0.2 V is accounted by a constant offset of the association free energy values of the OECT. We ascribe this offset to the different chemical potentials that the gate electrode takes in the EGOFET and OECT respectively. Indeed, an upward vertical displacement of the OECT data (full blue squares) by a vertical shift of +13 kJ mol^{-1} yields the branch with empty blue squares and makes a global polynomial fit of $\Delta G°$ (dotted blue curve in **Figure 3.9 A**) suitable for interconnecting the whole data set. The rank three of the polynomial hints to charge and dipole build up, accompanied by a dependance of the interfacial capacitance from V_{GS}:

$$\Delta G°(V_{GS}) = \Delta G_b^{\circ} + \delta Q(V_{GS} - V_0) + \delta C(V_{GS} - V_0)^2 + \delta(\frac{dC}{dV_{GS}})(V_{GS} - V_0)^3 \qquad (3.5)$$

Here V_0 is the internal voltage, characteristic of the bound antibody/antigen pair, and accounts for the electrostatic contributions to the free energy in the absence of an external applied voltage. We take it as the minimum of the fitted curve that lies in the proximity of -0.4 V. We find that the (intrinsic) binding contribution is ΔG_b° -67.6 ±0.1 kJ mol^{-1}, the charge build up is δQ=-2.2±0.6 kC mol^{-1}, the capacitance build up is δC= 38.7±3.0 kF mol^{-1}, and the change of capacitance $\delta(dC/d\ V_{GS})$= -19.9 ±3.2 kF V^{-1} mol^{-1}. Simple calculations, shown in **Figure 3.10**, allow us to assess that the dominant contribution to the electrostatic free energy comes from the capacitance, although around the electroneutrality point at -0.4 V the dominant contribution is the charge build up.

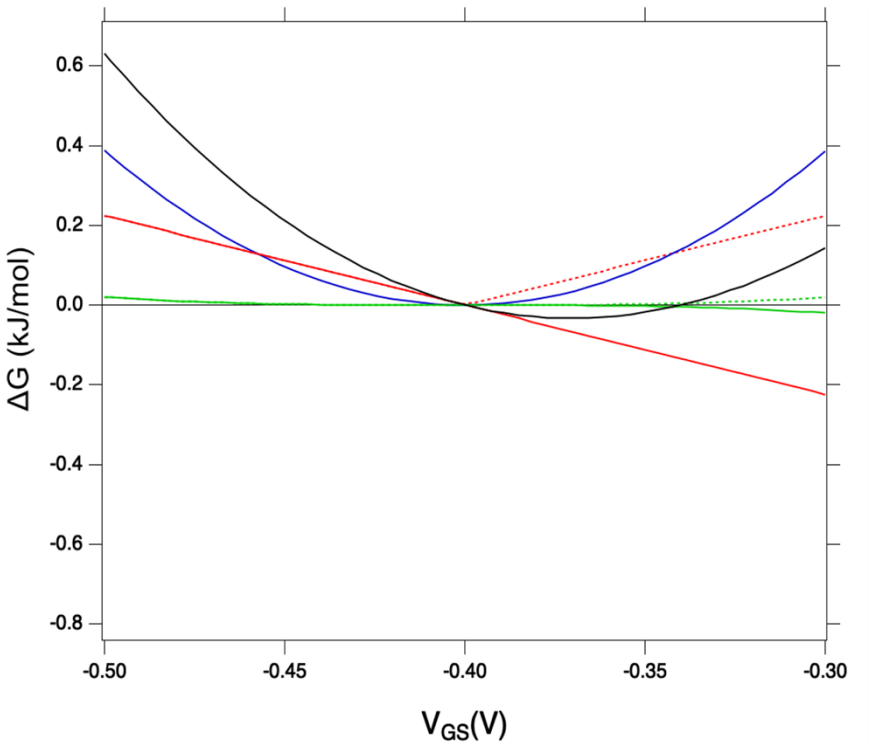

Figure 3.10. Contributions to the total (black line) electrostatic free energy: charge contribution (continuous red line, dotted red line is the corresponding absolute value); capacitance contribution (continuous blue line) and change in capacitance dC/dV_{GS} (continuous green line, dotted green line is the corresponding absolute value).

We discuss now the Frumkin factor *g'*, which accounts for the changes in the standard free energy of adsorption $\Delta G°$ caused by molecules getting adsorbed on the surface. From the fit of the logarithm of Eq. 3.3 we obtain the following *g'* values: -9.34 (± 0.19) and -8.71 (± 0.45) for OECT and EGOFET, respectively. In **Figure 3.9 B** we show the trend of *g' vs.* V_{GS} for OECT and EGOFET. The *g'* values of OECT vary more rapidly *vs.* V_{GS} between -8 and -11, whereas in EGOFET they exhibit a parabolic trend in the proximity of -8. Once again, an upward vertical offset of the OECT data will bring the experimental data onto one continuous curve (data not shown).

To the best of our knowledge, the Frumkin model has not been applied yet to elucidate the thermodynamics of antibody/antigen binding, therefore no reference values can be found in the literature. Yet, the magnitude of the *g'* value found here is in line, though slightly higher, with those reported in the literature for organic molecules. Since $g' = -\Delta\mu_{int}/RT$, negative *g'* values correspond to a positive $\Delta\mu_{int}$ where $-\Delta\mu_{int}$ is the interaction potential between adsorbed species. Thus, adsorption is disfavored as θ increases, due to the presence of repulsive interactions between adsorbed species, either steric or electrostatic, or both.

We stress how the Frumkin model here, despite its simplicity, successfully accounts for the emergence of intermolecular repulsions between the bound antigen/antibody pairs. The result is that the effective association free energy ΔG°_{eff} increases (becomes more positive) with respect to its standard value $\Delta G°$:

$$\Delta G^{\circ}_{eff}(V_{GS},\theta) = \Delta G^{\circ}(V_{GS}) - RTg'(V_{GS})\theta$$
$$= \Delta G^{\circ}(V_{GS}) + \mu_{int}(V_{GS})\theta \qquad (3.6)$$

ΔG°_{eff} corresponds to what is typically termed the apparent standard free energy when describing adsorption on electrified interfaces.[53–55]

To reconciliate the apparent difference between the OECT and EGOFET datasets, we estimate the effective binding constant that we define as:

$$K_{a,eff}(V_{GS},\theta) = K_a(V_{GS})exp\,[g'(V_{GS})\theta] \qquad (3.7)$$

Eq. 3.7 governs the equilibrium at a given V_{GS} and θ. In **Figure 3.11 A** we show the top view as contour plot of $\log_{10}[K_{a,eff}(V_{GS},\theta)$ for the two device architectures. The values span four and six decades for EGOFET and OECT, respectively, starting from about 10^{11} and 10^{13} (almost 10^{14}) at low surface coverage (as in **Figure 3.9**) down to 10^{8} in both cases when θ approaches 1. One appreciates that $K_{a,eff}$ is largest at low θ (thus making the device sensitivity highest) and decreases by one order of magnitude as θ tends to 2/|g'| ~ 0.2-0.3. This implies that the sensor, whether is OECT or EGOFET, loses sensitivity due to the electrostatic repulsions of the adsorbed IL-6 already at a few tens percent coverage. We point out that the θ =0 values in Eq. (3.7) tend to $K_a(V_{GS})$, that is the association constant that would be predicted by the Langmuir fit in the range of the experimental dataset where the lateral interactions represented by g' are negligible. A last observation is that the two device architectures have a different sensitivity at low θ values, while they exhibit comparable $K_{a,eff}$ for large θ values. Noticeably, for large θ values the dependence of $K_{a,eff}$ on V_{GS} is damped especially for EGOFET.

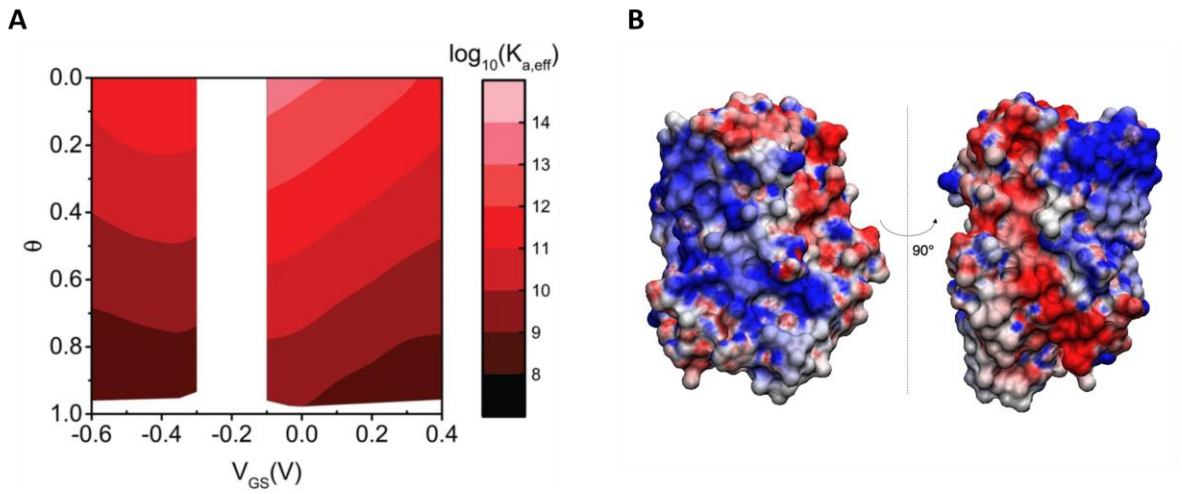

Figure 3.11. A) Contour plot of the effective binding constant as Log10 ($K_{a,eff}$) as a function of θ and V_{GS} for EGOFET (left strip) and OECT (right strip). **B)** Calculated electrostatic potential for IL-6 mapped on its molecular surfaces. Potential values lower than -5 kT e^{-1} are colored in red, potential values higher than +5 kt e^{-1} are depicted in blue.

To discuss the sign of the *g'* parameter, we start from the consideration that in our case the characteristic length scale of the sensing interface is much larger (several nm) of that of the classical systems treated with the Frumkin isotherm (water and small molecules, *viz.* a few Å). Therefore, we cannot invoke the competition between adsorbate and the water molecules forming a monolayer at the electrode/electrolyte interface. Moreover, in our gate electrode, the presence of a mixed SAM, and the further immobilization of the antibodies, moves the first hydration layer further outwards from the electrode surface. We then expect that the interaction between the charged surface and the water dipoles are much weaker here than in the case of adsorption of species at a bare electrified surface. Therefore, in our case, we propose that the charges present on the protein surface (target, probe, and their complex), and the intermolecular interactions between them are responsible for the observed sign of *g'* as well as its dependence on the gate potential.

From inspection of the three-dimensional structure of IL-6 (PDB code: 1 ALU), it is apparent that several residues with charged side chains are present. By running a structure-based prediction of their protonation state using the PropKa server,[56] we predict that all the Glu and Asp residues are surface exposed and likely deprotonated to yield a negative charge, while all Arg and Lys in the sequence, whose sidechains are most likely positively charged, are also exposed to the surface. Estimation of the protein isoelectric point (pI) with different web servers yields pI values around 6.2 and a predicted net protein charge at physiological pH of about -2.

We also calculated the surface electrostatic potential for IL-6 (see **Figure 3.11 B**) where the calculated surface potential of IL-6 is shown. It is apparent that the location of the charged and polar aminoacidic side chains yields regions of markedly positive (larger than 5 kT e^{-1}) and negative (smaller than -5 kT e^{-1}) electrostatic potential on the protein surface rather than an even distribution. We also estimated the protein dipole moment using a dedicated web server[57] and found a value of 385 Debye that is close to the average dipole moment that was estimated for more than 14000 unique chains deposited in the Protein Data Bank (543(± 420) Debye). Our analyses indicate that IL-6 is negatively charged at the operational pH, resulting from a constellation of charged side chains exposed to the solvent, and that it also bears a large dipole moment. These arguments support the possible relevance of electrostatic interactions between adsorbed IL-6 molecules in contributing to *g'*.

3.6 CONCLUSIONS

In this chapter, we assessed IL-6 biosensors operating with the same gate and different architectures, viz. OECT and EGOFET, for transduction of the biorecognition. In both cases we demonstrated the successful detection of IL-6 in the physio pathological concentration range, which span from pM to nM. The devices also proved to be very sensitive, with LOD below 1pM and with a very specific response to the analyte, shown in the control experiments. However, OECTs featuring PEDOT:PSS as OSC may have a higher potential for implementation as biosensors. PEDOT:PSS have been widely studied and commercialized, proving to have excellent electrical performance and high stability in water. Additionally, based on our experience, OECTs based PEDOT:PSS were more reproducible in terms of electrical performance than EGOFETs based on TIPS-Pentacene, which has proved to be more affected by changes in environmental conditions. For this work, could not use detergent Tween20 in the electrolyte for measurements with EGOFET because TIPS-Pentacene was sensitive to it, showing a worsening of the electrical performance after exposure to a Tween20-containing solution, unlike PEDOT:PSS.

We demonstrated that the Frumkin isotherm well describes the dose curves obtained by either EGOFET or OECT biosensors operating with functionalized gate. Albeit by eye the fitting result appears comparable to Hill isotherm, a more careful analysis carried out for the IL-6/anti-IL-6 pair of this work show that Frumkin provides better estimators of good fit than Hill, with the same number of variational parameters, and largely overcomes the performance of Langmuir.

A clear advantage of Frumkin isotherm is that it provides a clear physical view of the competing or synergic phenomena that affect the biorecognition at the gate electrode of either OECT and EGOFET sensors, in terms of coverage-dependent interactions of the adsorbed pairs. In the present work, repulsions between adsorbed IL-6 molecules were identified as the main source of competing interaction that led to negative values of the Frumkin parameter *g'*.

An important consequence is that, differently from Hill isotherm, Frumkin isotherm yields reliable values of the association constant, in line with literature data from independent techniques, and envisions a "decrease of specificity and sensitivity" by the sensor as the effective binding constant decreases exponentially with coverage.

On the one hand, the results give us confidence for using this model in the quantitative studies of the thermodynamics of recognition. Since the data were acquired under static conditions at the equilibrium state for each concentration, mass transport was not taken into account. The analysis of free energy carried out with Frumkin unifies the results obtained either by OECT and EGOFET. Since the gate functionalization is the same for both architectures, this suggests that the response of the sensors, that we fit to the Frumkin model, is genuinely due to events taking place at the gate/electrolyte interface. We highlight that in the limit of low coverage the Frumkin model provides the response predicted by Langmuir's, and hence retains a consistent description of equilibria, which instead is not explicitly defined in Hill's.

On the other hand, application of Frumkin isotherm allows us to estimate the effective range of coverage viable for sensing in terms of the Frumkin parameter. Our analysis suggests that the (absolute) value of *g'* can be used as a guideline for the tailoring of the gate functionalization, mainly targeting the areal density of recognition sites that keeps the effective binding constant as close as possible to the maximum value. This implies that it is neither necessary nor optimal to seek for achieving a probe coverage of the electrode close to unity, and that strategies of probe dilution" on the electrode may be effective in order to minimize $|g'|$ when this is negative. The Frumkin parameter may indeed be a viable estimator for comparing different functionalization strategies.

3.7 REFERENCES

[1] P. A. Manco Urbina, M. Berto, P. Greco, M. Sensi, S. Borghi, M. Borsari, C. A. Bortolotti, F. Biscarini, J. Mater. Chem. C 2021, 9, 10965.

[2] M. Kopf, M. F. Bachmann, B. J. Marsland, Nat. Rev. Drug Discov. 2010, 9, 703.

[3] S. Rose-John, Cold Spring Harb. Perspect. Biol. 2018, 10.

[4] T. Tanaka, M. Narazaki, T. Kishimoto, 2014, 6, 1.

[5] S. Kang, M. Narazaki, H. Metwally, T. Kishimoto, J. Exp. Med. 2020, 217, 1.

[6] T. Kishimoto, K. Ishizaka, J Immunol 1975, 114, 585.

[7] F. Schaper, S. Rose-John, Cytokine Growth Factor Rev. 2015, 26, 475.

[8] C. Liu, D. Chu, K. Kalantar-Zadeh, J. George, H. A. Young, G. Liu, Adv. Sci. 2021, 8.

[9] M. Cesari, B. W. J. H. Penninx, M. Pahor, F. Lauretani, A. M. Corsi, G. R. Williams, J. M. Guralnik, L. Ferrucci, Journals Gerontol. - Ser. A Biol. Sci. Med. Sci. 2004, 59, 242.

[10] R. Varadhan, W. Yao, A. Matteini, B. A. Beamer, Q. L. Xue, H. Yang, B. Manwani, A. Reiner, N. Jenny, N. Parekh, M. Daniele Fallin, A. Newman, K. Bandeen-Roche, R. Tracy, L. Ferrucci, J. Walston, Journals Gerontol. - Ser. A Biol. Sci. Med. Sci. 2014, 69 A, 165.

[11] M. Puzianowska-Kuźnicka, M. Owczarz, K. Wieczorowska-Tobis, P. Nadrowski, J. Chudek, P. Slusarczyk, A. Skalska, M. Jonas, E. Franek, M. Mossakowska, Immun. Ageing 2016, 13, 1.

[12] W. De Jager, H. Te Velthuis, B. J. Prakken, W. Kuis, G. T. Rijkers, Clin. Diagn. Lab. Immunol. 2003, 10, 133.

[13] M. Berggren, A. Richter-Dahlfors, Adv. Mater. 2007, 19, 3201.

[14] L. Torsi, M. Magliulo, K. Manoli, G. Palazzo, Chem. Soc. Rev. 2013, 42, 8612.

[15] J. Rivnay, R. M. Owens, G. G. Malliaras, Chem. Mater. 2014, 26, 679.

[16] X. Strakosas, M. Bongo, R. M. Owens, J. Appl. Polym. Sci. 2015, 132, 41735.

[17] D. T. Simon, E. O. Gabrielsson, K. Tybrandt, M. Berggren, Chem. Rev. 2016, 116, 13009.

[18] B. Burtscher, P. A. Manco Urbina, C. Diacci, S. Borghi, M. Pinti, A. Cossarizza, C.

Salvarani, M. Berggren, F. Biscarini, D. T. Simon, C. A. Bortolotti, Adv. Healthc. Mater. 2021, 2100955.

[19] D. Wang, V. Noël, B. Piro, Electronics 2016, 5.

[20] P. Lin, F. Yan, P. Lin, F. Yan, Adv. Mater 2012, 24, 34.

[21] A.-M. Pappa, O. Parlak, G. Scheiblin, P. Mailley, A. Salleo, R. M. Owens, n.d..

[22] C. Scandurra, K. Björkström, L. Sarcina, A. Imbriano, C. Di Franco, R. Österbacka, P. Bollella, G. Scamarcio, L. Torsi, E. Macchia, K. Björkström, R. Österbacka, L. Torsi, E. Macchia, G. Scamarcio, D. Bari, A. Moro, B. 70125, I. E. Macchia, C. Scandurra, L. Sarcina, A. Imbriano, C. Di Franco, P. Bollella, Adv. Mater. Technol. 2023, 8, 2201910.

[23] M. Berto, C. Diacci, R. D'Agata, M. Pinti, E. Bianchini, M. Di Lauro, S. Casalini, A. Cossarizza, M. Berggren, D. Simon, G. Spoto, F. Biscarini, C. A. Bortolotti, Adv. Biosyst. 2018, 2, 1700072.

[24] D. Gentili, P. D'Angelo, F. Militano, R. Mazzei, T. Poerio, M. Brucale, G. Tarabella, S. Bonetti, S. L. Marasso, M. Cocuzza, L. Giorno, S. Iannotta, M. Cavallini, J. Mater. Chem. B 2018, 6, 5400.

[25] J. Yu, A. Yang, N. Wang, H. Ling, J. Song, X. Chen, Y. Lian, Z. Zhang, F. Yan, M. Gu, Nanoscale 2021, 13, 2868.

[26] C. Liao, C. Mak, M. Zhang, H. L. W Chan, F. Yan, C. Liao, C. Mak, M. Zhang, H. L. W Chan, F. Yan, Adv. Mater. 2015, 27, 676.

[27] M. Galliani, C. Diacci, M. Berto, M. Sensi, V. Beni, M. Berggren, M. Borsari, D. T. Simon, F. Biscarini, C. A. Bortolotti, Adv. Mater. Interfaces 2020, 7.

[28] J. Buijs, J. W. T. Lichtenbelt, W. Norde, J. Lyklema, Colloids Surfaces B Biointerfaces 1995, 5, 11.

[29] C. Zhou, J.-M. Friedt, A. Angelova, K.-H. Choi, W. Laureyn, F. Frederix, L. A. Francis, A. Campitelli, Y. Engelborghs, G. Borghs, 2004.

[30] C. Ibau, M. Md Arshad, S. C. Gopinath, M. M. Nuzaihan, M. Fathil, S. Arina Shamsuddin, 2020.

[31] M. Berto, S. Casalini, M. Di Lauro, S. L. Marasso, M. Cocuzza, D. Perrone, M. Pinti, A. Cossarizza, C. F. Pirri, D. T. Simon, M. Berggren, F. Zerbetto, C. A. Bortolotti, F.

Biscarini, Anal. Chem. 2016, 88, 12330.

[32] C. Diacci, M. Berto, M. Di Lauro, E. Bianchini, M. Pinti, D. T. Simon, F. Biscarini, C. A. Bortolotti, Biointerphases 2017, 12.

[33] X. P. A. Gao, G. Zheng, C. M. Lieber, Nano Lett. 2010, 10, 547.

[34] K. Y. Foo, B. H. Hameed, Chem. Eng. J. 2010, 156, 2.

[35] J. Wang, X. Guo, Chemosphere 2020, 258, 127279.

[36] I. Langmuir, J. Am. Chem. Soc. 1918, 40, 1361.

[37] H. Swenson, N. P. Stadie, Langmuir 2019, 35, 5409.

[38] A. V. Hill, J. Physiol. 1910, 40, iv.

[39] L. K. Koopal, W. H. van Riemsdijk, J. C. M. de Wit, M. F. Benedetti, J. Colloid Interface Sci. 1994, 166, 51.

[40] R. Saadi, Z. Saadi, R. Fazaeli, N. E. Fard, Korean J. Chem. Eng. 2015, 32, 787.

[41] M. Selvaraj, P. Greco, M. Sensi, G. D. Saygin, N. Bellassai, R. D'Agata, G. Spoto, F. Biscarini, Biosens. Bioelectron. 2021, 182.

[42] M. Berto, S. Casalini, M. Di Lauro, S. L. Marasso, M. Cocuzza, D. Perrone, M. Pinti, A. Cossarizza, C. F. Pirri, D. T. Simon, M. Berggren, F. Zerbetto, C. A. Bortolotti, F. Biscarini, Anal. Chem. 2016, 88, 12330.

[43] S. Goutelle, M. Maurin, F. Rougier, X. Barbaut, L. Bourguignon, M. Ducher, P. Maire, Fundam. Clin. Pharmacol. 2008, 22, 633.

[44] A. Frumkin, Zeitschrift für Phys. Chemie 1925, 116U, 466.

[45] M. Mozaffari Majd, V. Kordzadeh-Kermani, V. Ghalandari, A. Askari, M. Sillanpää, Sci. Total Environ. 2022, 812.

[46] W. H. Press, S. a Teukolsky, W. T. Vetterling, B. P. Flannery, Numerical Recipes: The Art of Scientific Computing, 2007.

[47] E. Alfinito, M. Beccaria, M. Ciccarese, Biosensors 2020, 10.

[48] C. Blanchetot, N. De Jonge, A. Desmyter, N. Ongenae, E. Hofman, A. Klarenbeek, A. Sadi, A. Hultberg, A. Kretz-Rommel, S. Spinelli, R. Loris, C. Cambillau, H. De Haard, J. Biol. Chem. 2016, 291, 13846.

[49] S. Shaw, T. Bourne, C. Meier, B. Carrington, R. Gelinas, A. Henry, A. Popplewell, R. Adams, T. Baker, S. Rapecki, D. Marshall, A. Moore, H. Neale, A. Lawson, MAbs 2014, 6, 773.

[50] J. P. Landry, Y. Ke, G.-L. Yu, X. D. Zu, J. Immunol. Methods 2015, 417, 86.

[51] B. C. Braden, W. Dall'Acqua, E. Eisenstein, B. A. Fields, F. A. Goldbaum, E. L. Malchiodi, R. A. Mariuzza, F. P. Schwarz, X. Ysern, R. J. Poljak, Pharm. Acta Helv. 1995, 69, 225.

[52] H. J. Gould, B. J. Sutton, A. J. Beavil, R. L. Beavil, N. McCloskey, H. A. Coker, D. Fear, L. Smurthwaite, Annu. Rev. Immunol. 2003, 21, 579.

[53] B. E. Conway, E. Gileadi, Can. J. Chem. 1964, 42, 90.

[54] R. Parsons, Trans. Faraday Soc. 1958, 54, 1053.

[55] E. Blomgren, J. O. M. Bockris, J. Phys. Chem. 1959, 63, 1475.

[56] M. H. M. Olsson, C. R. SØndergaard, M. Rostkowski, J. H. Jensen, J. Chem. Theory Comput. 2011, 7, 525.

[57] C. E. Felder, J. Prilusky, I. Silman, J. L. Sussman, Nucleic Acids Res. 2007, 35, W512.

4 Il-1β Biosensor

This chapter describes and demonstrates the successful development of an EGOT-based biosensor for the detection of cytokine IL-1β. In this study, we investigate other parameters apart from the typical change in drain current, introducing threshold voltage and transconductance to gain insight into the sensing and transduction mechanism in EGOTs.

4.1 INTRODUCTION

4.1.1 IL-1β

IL-1β is a heterodimeric small protein (17 kDa) that belongs to the family of IL-1 cytokines. This protein is involved in many biological processes, with a main role in generating and maintaining the inflammatory response, often acting in combination with cytokines IL-6 and TNF-α. Like many other cytokines, one of the hallmark characteristics of this protein is pleiotropism, which refers to featuring several biological activities. Among these biological activities, the three more relevant are the induction of proinflammatory proteins, hematopoiesis, and immune cell differentiation. The mature form of IL-1β is obtained only after the cleavage of the pro-IL-1β protein, triggered by an inflammatory mediator.[1–3] The circulating levels of this protein under physiological conditions are very low, below 20 pg mL^{-1} (∼1 pM).[4,5] Since IL-1β is involved in the signaling pathway of nearly every organ system of the body, its production is tightly controlled and can be easily deregulated by a wide range of disease processes.[3] Consequently, it has been associated with a wide range of autoimmune[6,7] and inflammatory[8,9] diseases, as well as with obesity, being especially involved in the development of low-grade systemic inflammation characteristic of this condition.[10–13] The longitudinal "The InCHIANTI study" have associated elevated levels of IL-1β with two specific clinical conditions, Congestive Heart Failure (CHF) and Angina.[1] This study investigates the factors responsible for the physical deterioration in the elderly population in the surroundings of Florence, and its association with the chronic low-grade inflammation that occurs with aging, named Inflammaging.[14] Since IL-1β is mainly involved in the inflammatory response and is implicated in several diseases associated with the inflammatory process, it is a promising biomarker of inflammaging. This is the reason why it has been selected for the development of aging-biomarkers sensors during this thesis.

The current standard techniques for the detection of cytokines in circulation, among them IL-1β, are based on optical immunosensors Enzyme-linked immunosorbent assay (ELISA) and Flow cytometry-based technologies. Both techniques rely on antibody-antigen interaction, and on colorimetric reaction to quantitatively determine the specific analyte, featuring a typical limit of detection (LOD) of below 1 pg mL^{-1} (0.05 pM) and 20 pg mL^{-1} (1 pM) respectively.[15] Despite their inherent robustness and reliability, they require a relatively large volume of biological sample, expensive equipment, specialized personnel, and labelling. These disadvantages hamper their implementation at the Point-of-Care (PoC) testing and as portable devices.

4.1.2 DPP-DTT EGOT-based biosensors

Electrolyte-gated organic transistors (EGOTs) are a type of organic thin-film transistors that are operated aqueous media. They are three terminal devices that consist of a drain (D) and source (S) electrodes connected by an organic semiconductor (OSC) material forming the channel, which in turn is connected to the third electrode, the gate (G) through the electrolyte. Within the EGOT family we can find two main architectures, Electrolyte Gated Organic Field Effect Transistors (EGOFET), and Organic Electrochemical Transistors (OECT), which differ in the OSC (im)permeability to the ions from the electrolyte. The operation of EGOTs involves the formation of electric double layers along the gate/electrolyte and channel/electrolyte interfaces in the case of EGOFET and across the whole OSC for OECTs.[16–18] This allows EGOT devices to operate at low voltages and with a fast response, consequently the can be used for real-time monitoring working with the biological samples as electrolyte, and with very high sensitivity due to its outstanding capabilities of amplification of small biological signals. All these feature make EGOT a robust alternative strategy for sensing.[19–23]

During this work, the OSC material was the polymer Poly[3,6-bis(5-thiophen-2-yl)-2,5-bis(2-octyldodecyl)pyrrolo[3,4-c]pyrrole1,4(2H,5H)-dione-2,2'-diyl-alt- thieno[3,2-b]thiophen-2,5-diyl] (**DPP-DTT**). Electrical characterization of OFET devices using DPP-DTT as OSC showed very high hole mobility values in saturation regime (up to 10.5 cm^2 V^{-1} s^{-1}) and ON/OFF ratio above 10^6.[24] This polymer film is apparently permeable to ions,[25] therefore the EGOT devices based on this material could be classified as OECTs, and some examples of DPP-DTT-based EGOTs in the literature do classify them as such.[25,26] However, we can also find EGOT-based sensors based on DPP-DTT categorized as EGOFETs.[27–29] There is no agreement in the bioelectronics community about whether the devices would be EGOFETs or OECTs. To avoid any confusion here we will refer to these devices simply as EGOTs. Independently to their classification, the devices were used as potentiometric biosensors in the present study. Consequently, DPP-DTT was chosen as OSC for this biosensor because of its excellent electrical properties, as mentioned above, and its stability over time even in complex solutions, such as cell culture media[27]: within this respect, DPP-DTT performs better than previously used TIPS-Pentacene.

4.2 EGOT FABRICATION

4.2.1 Transistor fabrication

The EGOTs were fabricated on a Micrux substrate featuring interdigitated drain and source electrodes, as previously described in Chapter 2.1.1, with a channel width/length (*W/L*) of

49000. The substrates were first cleaned using an ultrasonication bath in 3 steps: i) 15 minutes in 1% Hellmanex II, ii) 15 minutes in water, and iii) 15 minutes in ethanol. In between baths, the substrates were rinsed 3 times with water. Before OSC deposition, TPs were rinsed with ethanol and dried under N_2 flow. 5 mg mL^{-1} DPP-DTT was deposited on the substrate by spin coating at 2000 rpm for 2 minutes and cured in the oven at 140 °C for 45 minutes. Devices were stored immersed in 50 mM Phosphate Buffer solution (pH 7.4) until use.

4.2.2 Gate Functionalization

The second part of developing a biosensor is endowing it with biorecognition capabilities. Here, we worked with a gold wire as a gate electrode, where the biorecognition moieties were immobilized. The strategy of choice exploits the strong biotin/avidin affinity, described in more detail in Chapter 2.1.4. First, the gold wire was cleaned by immersion in 2.5M KOH at 130 °C for 4 hours, followed by abundant rinsing with water, and then a final immersion in concentrated H_2SO_4 at 220 °C for 2 hours. The clean gate was abundantly rinsed with water and dried under nitrogen flow. The gate functionalization was performed following the next protocol: i) gate incubation in a mix of biotinlylated OEG:OEG (1:9) in ethanol for the formation of a first biolayer of SAM exposing biotin headgroups, ii) incubation in 2 μM Neutravidin (NA) in 1x PBS pH 7.4 for 20 minutes, iii) gate incubation in 0.1 mg mL^{-1} anti-IL-1β biotinylated antibody in 1x PBS for 40 minutes, iv) and a final incubation step in 0.1 mg mL^{-1} bovine serum albumin (BSA) in 1x PBS containing 0.05 % Tween20. The whole functionalization process was performed at room temperature (RT).

4.2.3 Characterization of Functionalization Process

4.2.3.1 Optical Characterization

Fiber optic surface plasmon resonance (FO-SPR) has been used to monitor the functionalization process in real-time (see Chapter 2 for more details on this technique). These experiments were performed in collaboration with Professor W. Knoll's and Professor Jakub Dostalek's group at the Austrian Institute of Technology (AIT). The real-time monitoring started with the FO functionalized with the mixed biotin-OEG:OEG SAM in 1x PBS, as can be seen in **Figure 4.1**. We chose this architecture for the optical characterization since the functionalization of FO mimics the setup conditions used for the gold wire functionalization. The optical signal is presented as a shift of the resonance wavelength (λ_{SPR}), corresponding to changes in the local refractive index, which in turn is associated with the molecular mass of the adsorbed biolayer on the gold surface. Measurements were performed in real-time under static conditions, monitoring the functionalization process in 1x PBS electrolyte. In between

steps, the FO was washed twice by immersion in the buffer solution. The buffer baseline before and after each functionalization step was taken for calculating the optical signal. From the data analysis, we can estimate the surface mass density (see Chapter 2, eq. 2.1). The average of 5 experiments yielded surface coverage θ values of 301.9 ± 5.8 ng cm^{-2} for NA, equivalent to $2.66(\pm 0.41) \times 10^{12}$ molecules cm^{-2}, and 268.8 ± 4.9 ng cm^{-2} for anti-IL-1β Ab, equivalent to $1.45(\pm 0.36) \times 10^{12}$ molecules cm^{-2}. These Ab values are in the same range as the ones obtained by the mixed MUA:MCH SAM used for IL-6 detection and are in line with those reported in the literature using different functionalization strategies (with values ranging from 4 to 8×10^{11} molecules cm^{-2}).[30–32] The FO-SPR has therefore proved to be a valuable tool for characterizing gate functionalization.

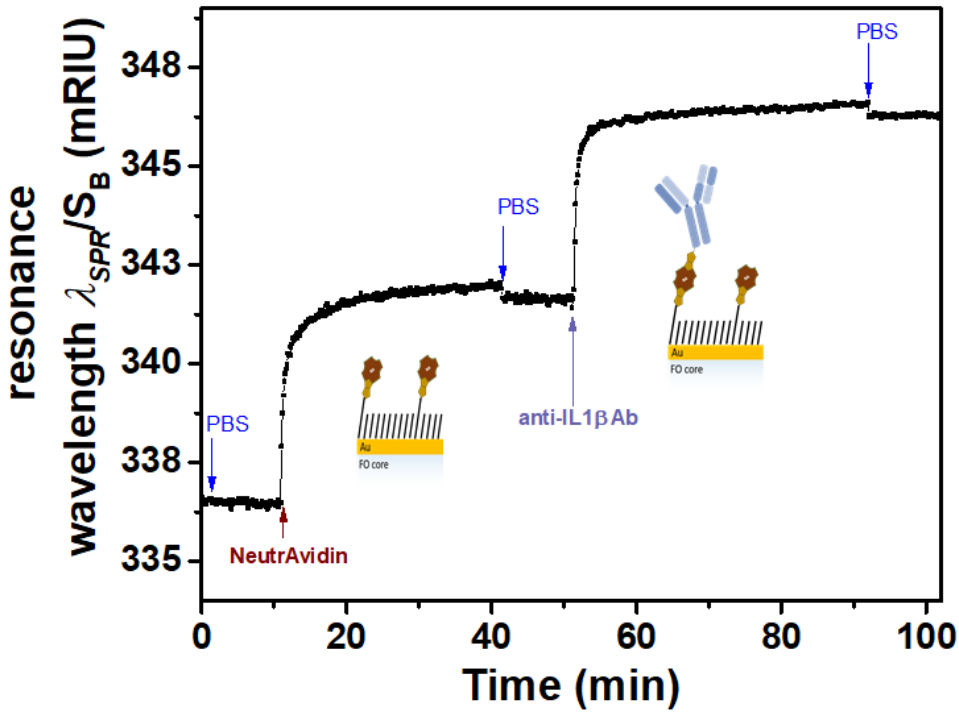

Figure 4.1. SPR curves monitoring the FO functionalization in 1x PBS, showing step (ii), NA binding, and step (iii), anti-IL-1β Ab binding in real-time.

Before integrating the sensing electrode into the EGOT device, we tested the sensing capabilities of the functionalized surface by means of Surface Plasmon-Enhanced Fluorescence Spectroscopy (SPFS). This technique overcomes the sensitivity issues of SPR for the detection of small molecules, by using fluorescence labelling in a classical sandwich assay configuration (capture antibody – target analyte – detection antibody). Moreover, when used in combination with SPR, the fluorescence signal is increased due to the surface plasmon-enhanced intensity of the electromagnetic field on the SPR surface, providing SPFS with high sensitivity.[33,34]

Measurements were performed in a flow-cell of approximately 12 μL with 0.5 mL min^{-1} flow rate. The SPR and SPFS signals were simultaneously recorded, as can be seen in **Figure 4.2 A**, where the black line corresponds to the SPR measurement and the blue line corresponds to the SPFS measurement. The graph is divided into three blocks. The first block is the gate functionalization: here we only obtained SPR signal since no fluorophore was used for monitoring fluorescence output. We can clearly observe three binding curves that correspond to the three functionalization steps: (ii) Neutravidin, (iii) anti-IL-1β Ab, and (iv) BSA/Tween20. The second block corresponds to a control previous to the titration. Here we exposed the sensing surface to the fluorochrome-labelled detection antibody (2 μg mL^{-1} in 1x PBS). As we can see in the graph, there is no fluorescence signal for the control experiment, proving the anti-fouling properties of the functionalization matrix. In a first attempt, we were not using any extra anti-fouling molecules, such as BSA or Tween20, and we observed some non-specific binding by SPFS (data not shown). Conversely, once a final step consisting of incubation in antifouling BSA/Tween20 mixture was added to the protocol, we could observe a specific response to the analyte and absence of non-specific response in the control experiments. In the third block the titration is shown in real time. We can observe how the SPR is not sensitive enough to detect such a small protein, even at its highest concentration. By contrast, SPFS shows high sensitivity to the analyte, and is able to detect even the smallest concentration explored, namely 10 pM. The analysis of the fluorescence signal (**Figure 4.2 B**) shows a Langmuir-type behaviour (Eq. 4.1), yielding an equilibrium dissociation constant $K_D = (6.1 \pm 0.7) \times 10^{-9}$, with a limit of detection (LOD) of 100 pM, which was computed as the $NSR_0 + 3\sigma$, where NSR_0 is the average signal from the blank (absence of the analyte) and σ is its standard deviation. The Langmuir equation can be expressed in terms of NSR signal as:

$$NSR = NSR_{max} \frac{K_A c}{(1+K_A c)} \qquad (4.1)$$

where *NSR* stands for the normalized sensor response, K_A is the equilibrium association constant, and *c* is the analyte concentration.

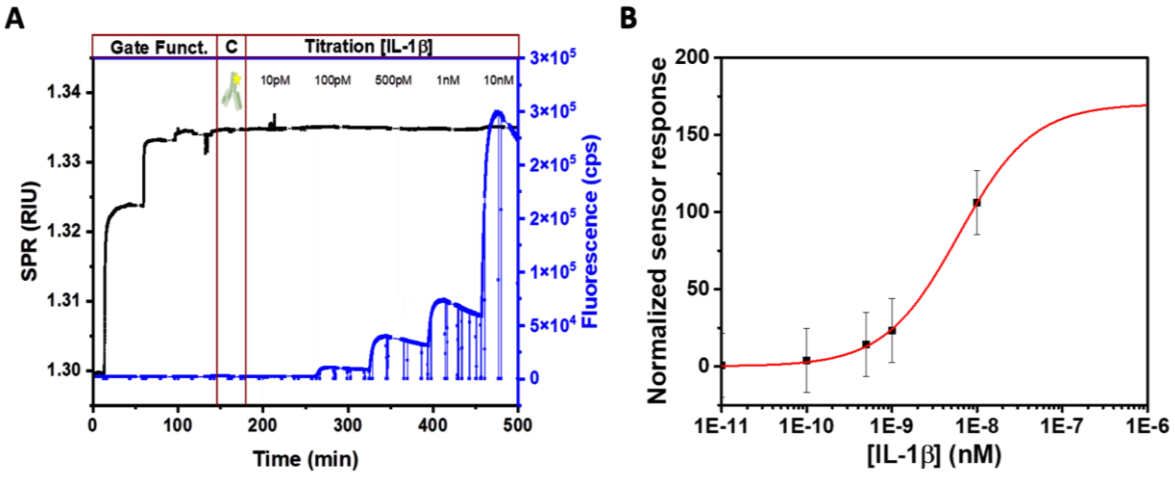

Figure 4.2. A) SPR/SPFS titration curves for IL-1β binding in 1x PBS containing 0.1% BSA and 0.05% Tween20. The left Y axis corresponds to the SPR signal (black) and the right Y axis corresponds to the SPFS signal (blue). The plot is divided in three blocks: Gate functionalization, control experiment, and IL-1β titration. **B)** SPFS-based dose curve, displaying *NSR vs.* c. The Langmuir fit is represented as a red line. The error bars correspond to the maximum deviation.

4.2.3.2 Electrochemical Characterization

The functionalization process was also followed using electrochemical techniques, explained in more detail in Chapter 2.3. The chemisorption of the mixed SAM was monitored by cyclic voltammetry (CV) and faradaic electrochemical impedance spectroscopy (*f*-EIS), as shown in **Figure 4.3**. From the CV (in the inlet) we can observe the successful full coverage of the gate electrode after overnight incubation in the mixed SAM, as witnessed by a complete blockage of the electron exchange between the redox probe ($[Fe(CN)_6]^{3-}/[Fe(CN)_6]^{4-}$) in solution with the electrode. The subsequent functionalization steps were only monitored by *f*-EIS; the CV could not be used to investigate the whole functionalization process as a consequence of the well-formed SAM completely covering the electrode.

The Nyquist plots allow us to monitor the step-by-step sequential functionalization process, displaying an increase in both real and imaginary components of impedance following each functionalization step, as a proof of the immobilization of the neutravidin (NA), the anti-IL-1β antibody (Ab) and the BSA/Tween20. I would like to highlight here the importance of using an extra passivation layer besides the OEG; indeed, the adsorption of BSA/Tween20 onto the gate proves that OEG alone, in this case, is not sufficient as an anti-fouling compound. This goes in line with what has been observed before with the optical characterization. The results here presented are examples of the typical electrochemical response, which has been recorded for every individual experiment.

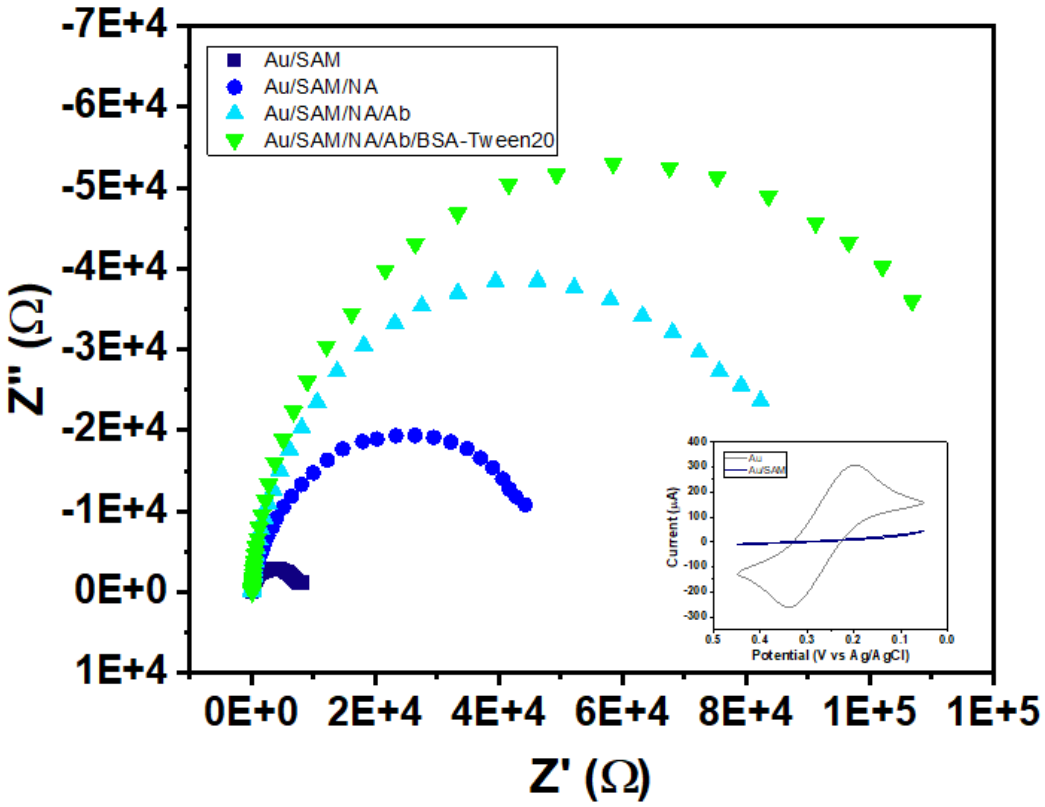

Figure 4.3. Electrochemical characterization of the functionalization procedure. The Nyquist plot shows the impedance recorded after each functionalization step, starting from the SAM formation. In the inset the CVs before and after SAM chemisorption are shown. Measurements were performed in a three-electrode setup, in 5 mM $K_3[FE(CN)_6]$ and 1 M KCl. Au stands for bare gold electrode, SAM for the mixed biotin-OEG:OEG SAM, NA for neutravidin, Ab for anti-IL-1β antibody, BSA-Tween20 for the last passivation step with BSA and Tween20.

4.3 BIOSENSOR RESPONSE

4.3.1 Transfer Curves

After a thorough characterization of its functionalization, the polycrystalline gold electrode was integrated into the EGOT architecture as a gate. We performed the detection of IL-1β *in situ* by exposing the sensor to increasing concentrations of the analyte from 10 pM to 200 nM in 1x PBS, pH 7.4.

Electrical measurements were performed inside a Faraday cage with an Agilent B2912A Source Measure Unit by applying a sweeping gate-source potential (V_{GS}) from 0 V to -0.7 V, and a fixed drain-source potential (V_{DS}) of -0.1 V. First, we assessed the transistors stability in two steps: (i) Preconditioning by recording 15 continuous transfer curves three times, changing the 1x PBS electrolyte every time. (ii) Stabilization by recording 5 transfer curves every 10

minutes, changing buffer in between measurements. We considered that the device had reached stability once the recorded transfer curves could be superimposed.

A typical response of a DPP-DTT based EGOT device to increasing IL-1β concentration is provided in **Figure 4.4**; a monotonic increase in the drain current (I_{DS}) at all gate voltages explored could be observed with increasing concentrations of IL-1β. The current increase is rather small in the pM regime, and much more marked when switching to the nM range. Such behaviour has been observed in 4 independent experiments, indicating satisfactory consistency and robustness of the device response to the target analyte.

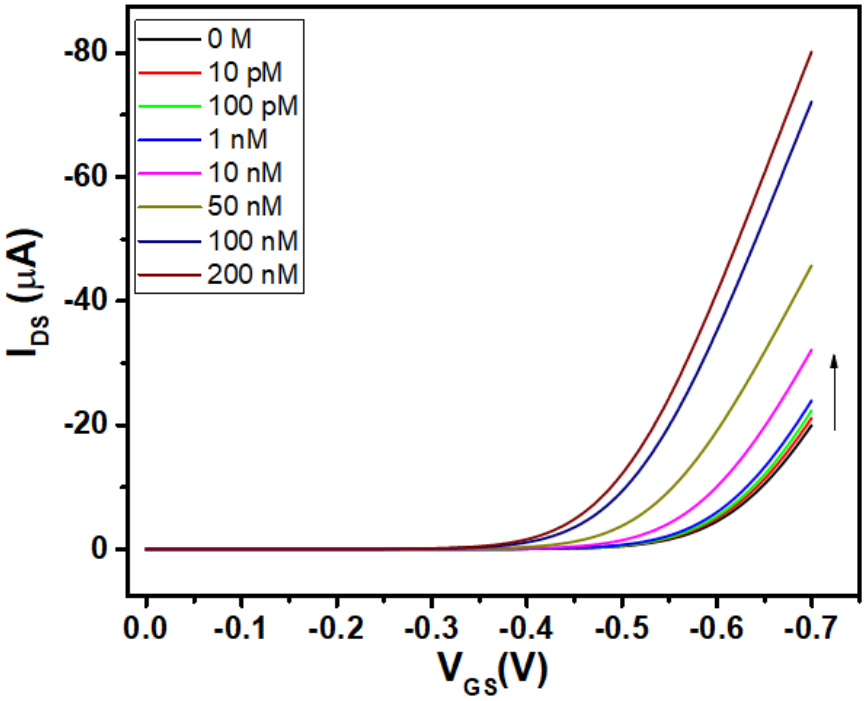

Figure 4.4. Transfer characteristics of DPP-DTT EGOT-based biosensor upon exposure to increasing concentrations of IL-1β in 1x PBS pH 7.4, with target analyte concentration ranging from 10 pM to 200 nM, as reported in the legend.

Changes in I_{DS} resulting from the IL-1β binding can be explained as a consequence of the modification of the electrochemical potential at the gate/electrolyte and channel/electrolyte interfaces, owing to the capacitive coupling of the gate to the channel. In order to understand the transduction mechanism, the immobilization matrix (the mixed SAM) and the protein layer (NA/antibody or NA/antibody/analyte complex) are treated as dielectric layers connected in series, leading to a linear reduction in potential across each layer from the electrode surface. Moreover, according to the Gouy-Chapman model, an exponential decay in potential at the protein layer/electrolyte interface and at the electrolyte/channel interface takes place.

Taking all this into consideration, one might argue that the increase in I_{DS} due to the binding of IL-1β suggests an enhancement of the EDL capacitance. Since the gate and the channel are capacitively coupled, an increment in gate capacitance is transduced into an increase in charge carriers density, explaining the obtained shift in drain current after the analyte binding at the same V_{GS}. For instance, after the sensor exposure to 100 nM IL-1β, the drain current values were triplicated under the same measurement conditions, attributing such change to the analyte binding.

4.3.2 Response quantification

The biosensor response was quantitatively analyzed by means of a dose curve, which was constructed by plotting changes in the device parameters as a function of the analyte concentration. The plotted change in current, named signal (*S*), can be expressed as $S = (I_{DS[c]} - I_{DS[0]})/I_{DS[0]}$ where $I_{DS[c]}$ is the drain current value at the target concentration and $I_{DS[0]}$ is the drain current value in the absence of the analyte, both taken at a given V_{GS} value. For the analysis of the sensor response, the signal was extracted at $V_{GS} = V_{th}$ in the absence of the analyte, as this gate voltage value corresponds to the region where the device showed the highest sensitivity.[35,36] It is noteworthy that V_{th} values fluctuate within a narrow range of 60 mV, when comparing different devices. The resulting dose curve can be seen in **Figure 4.5**, where the data exhibit a monotonically increasing trend as the concentrations of IL-1β increase. At the lowest concentrations (10 and 100 pM) the sensor response is very small in magnitude, almost superimposing to that at IL-1β=0 M, for. It is apparent that a sensor response is significantly distinct from that of the blank from the 1 nM concentration value, with a steep increase from 10 nM to 100 nM, and the trend almost reaching saturation levels at concentrations above 200 nM. Therefore, the active range where the sensor responds spans about two orders of magnitude in the nM range.

In **Figure 4.5** we can see that Langmuir isotherm yields a satisfactory fit to our data with the following equation:

$$S = Smax\frac{K_a c}{1+K_a c} \qquad (4.2)$$

where *S* is the measured signal, K_a is the equilibrium association constant, and *c* is the molecule concentration expressed in molarity. The fitting results yielded a $K_D = (4.4 \pm 0.4) \times 10^{-8}$. This value is about one order of magnitude higher than that obtained by SPFS; this is probably to be ascribed to the fact that the polycrystalline gold surfaces used in the SPFS and EGOT configuration are different. Nevertheless, both values fall reasonably close in the nM range,

which is slightly higher than the typical values for mouse monoclonal Ab. Some difference in the magnitude of K_D is to be expected for different approaches, especially when comparing affinity constants derived from binding curves using solid-surface immobilized antibodies and those from antibodies and analytes in solution.[37,38] Additionally, the LOD resulted in 1 nM, which was calculated as described before for the SPFS experiment. Importantly, although SPFS enables a lower LOD than the EGOT-based assay, ithe is crucial to highlight that EGOTs provide a response to the analyte concentration in a label-free scheme, unlike SPFS that requires fluorescence-labelling to reach higher sensitivity.

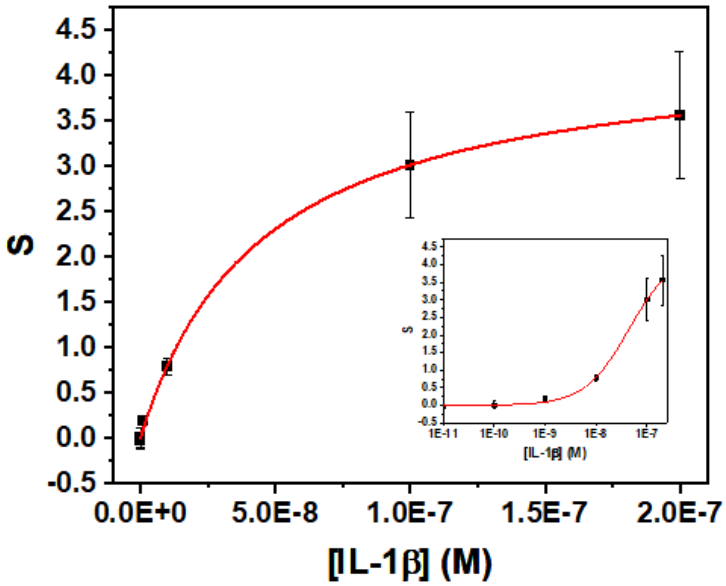

Figure 4.5. Dose curve S *vs.* molar concentration of IL-1β at $V_{GS} = V_{th}$ and V_{DS} = -0.1 V. In the inset, the dose curve in lin/log scale is provided. Solid red line represents the fit of the Langmuir binding model to the data, the data points correspond to the average of 4 independent experiments and the error bars represent the standard error of the mean (*SEM*).

We compared the sensitivity of both optical and electrical sensors, by taking the first derivative of the Langmuir fitting for each dose curve *N(S)R vs.* [IL-1β]. The difference in sensitivity is shown in **Figure 4.6**: we can clearly observe that SPFS (blue line) reaches its highest sensitivity in the pM range, while EGOT (black line) is most sensitive at the nM concentration range. From this analysis, we can also infer that SPFS is more than one order of magnitude more sensitive than EGOT biosensor. In both cases, the sensitivity peaks at the lowest investigated concentration values and decreases at the highest concentrations because the sensor response saturates.

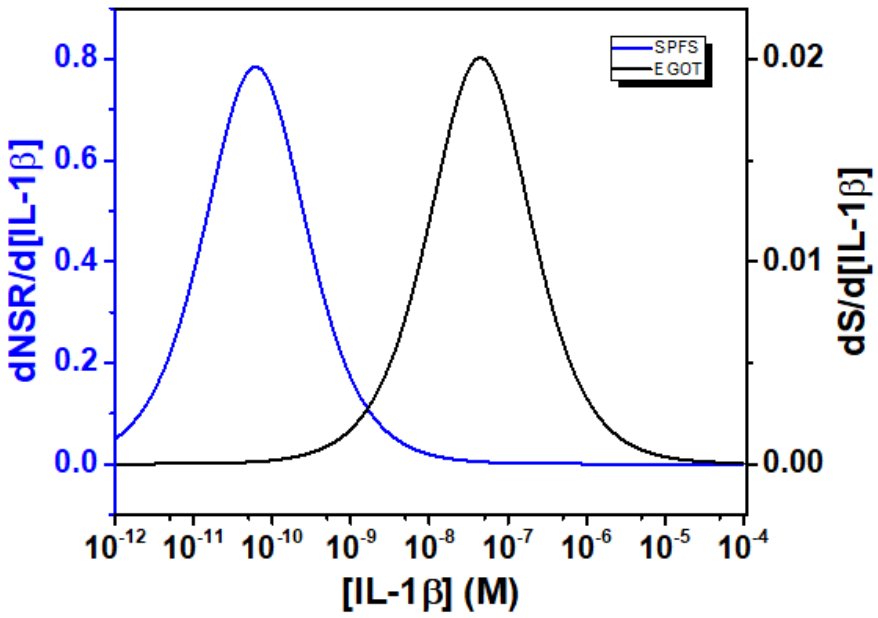

Figure 4.6. Comparison of sensitivity of SPFS and EGOT-based biosensors for the detection of IL-1β.

Measuring the sensor response in terms of changes in I_{DS} is the simplest and most straightforward way since it could be monitored in real-time (Chapter 5) and in principle, it does not require recording full transfer curves and further analysis of the device response. However, EGOTs are devices of a multiparametric nature. Thus, an examination of parameters beyond changes in I_{DS} can provide significant insights into the device response. **Figure 4.7** shows the device response in terms of threshold voltage (V_{th}) shift. The trend closely mirrors the response in terms of *S*, with V_{th} being shifted towards more positive values as the analyte concentration increases, with the largest shift of about 100 mV being observed for [IL-1β] = 200 nM. Thus, the binding event has a "doping" effect on the OSC, where a lower in magnitude gate bias is needed to turn the device ON, most likely as a consequence of a binding-induced shift of the electrochemical potential of the gate electrode.

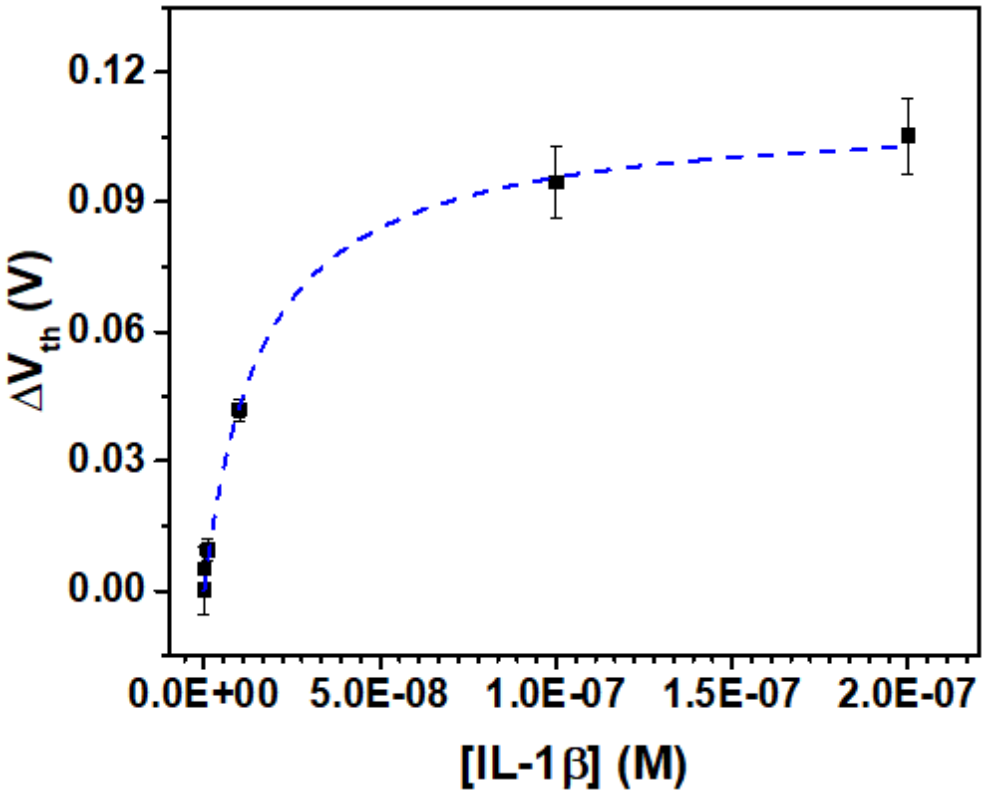

Figure 4.7. Dose curves expressed in terms of threshold voltage V_{th} as function of [IL-1β]. The data points represent the average of 4 independent experiments with their respective SEM (error bars), the dashed blue line is a guide for the eye.

4.3.3 Control Experiments

The device selectivity was tested by exposing the IL-1β EGOT-based biosensor to increasing concentrations of two possible interfering proteins, namely cytokine IL-6 and bovine serum albumin (BSA). IL-6 is another pro-inflammatory cytokine which could also be present in increased concentrations under pathological conditions. Albumin is a component of plasma and other biological samples, typically present in high concentrations (3.5-5 g dL^{-1}).[39] In this case the response was quantified by means of change in I_{DS} as a function of analyte concentration, and it is presented in **Figure 4.8**, comparing the non-specific response observed in the control experiments to the IL-1β signal. It is apparent that at lower concentrations (pM), where the EGOT biosensor is basically not responding to the target analyte, the non-specific signal corresponding to the control targets is basically indistinguishable from the specific one. On the contrary, when reaching the nM range, the signal from both non-specific targets is markedly lower in magnitude than the specific signal. Moreover, at [IL-1β] equal to or higher than 100 nM, besides being about 10 times smaller in magnitude, the drain current change from

the non-specific response goes in the opposite direction with respect to the specific signal, as a consequence of a decrease of I_{DS} with increasing non-specific target concentration.

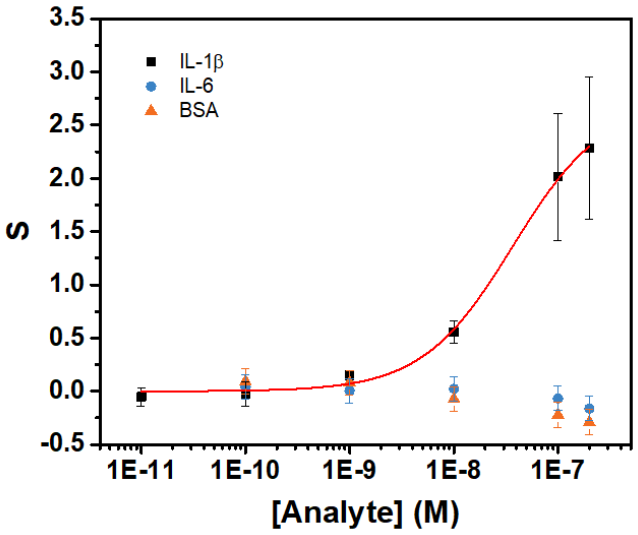

Figure 4.8. Dose curve comparing the sensor response to the target analyte IL-1β and to the control analytes, IL-6 and BSA. Here we are presenting the average of two experiments for each control analyte, with the maximum deviation as error bars.

From the Langmuir isotherm analysis and the control experiments, even taking into consideration the small but still non negligible non-specific response of the sensor, we can confirm that the sensor successfully detected IL-1β in the nM concentration range, with little non-specific response. The results from our label-free EGOT-based biosensor are encouraging, considering that SPFS requires labelling and a more sophisticated and expensive equipment, complicating its translation from the laboratory bench to the clinical practice. However, since IL-1β is a protein that is detectable in circulation only during pathological conditions and at concentrations in the pM range, this sensor still requires some optimization to decrease the LOD and increase its sensitivity in the physio-pathological range, and render the device a great alternative for its application with biological samples and its future implementation at the point-of-care (PoC) testing.

Clearly, the binding capabilities of the biorecognition molecule is a limiting factor. For further optimization, one can look for higher-affinity moieties; within this respect, there is a growing interest in engineering antibodies with very high affinity for IL-1β, that when used as sensing unit for optical biosensors enable the corresponding devices to reach LODs as low as 200 to 300 fM.[40] For other biomarkers, EGOT-based biosensors using other biorecognition molecules such as nanobodies, affimers, other peptides, aptamers, and even molecularly

imprinted polymers (MIP) have also been reported.[41] Alternatively, another possibility to decrease the LOD of EGOT-based sensors is to modify its architecture. A remarkable example is provided by the single molecule detection by Luisa Torsi's group,[42] which took advantage of millimiter-sized gates to reach a LOD of 10 zM. This is just an example of the many other successful transistors featuring very low LOD for the detection of proteins and genomic markers, extensively reviewed by E. Macchia and co-workers.[43] From their work, it is apparent that one the keys for the device remarkably low LOD is the use of a large gate electrode area, where the sensing ability does not only account for the large number of binding sites, but also for the electronic amplification characteristic of FET along with a network of collaborative electrostatic effects in a domino-like propagation effect at the sensing matrix. Another strategy could be optimizing the number of bioreceptors on the gate surface, taking into consideration the possible interactions between the probe/target couples that become relevant with increasing number of binding sites. Additionally, the LOD for this kind of devices is also affected by the stability of the transfer curves recorded with the blank (see section 4.3.2 Response quantification), as the fluctuations of the measured current generate the background signal. Hence, with a more thoroughly standardized OSC deposition process, it could be possible to lower the LOD.

4.4 CONCLUSION

In this chapter we assessed the detection of IL-1β with an EGOT-based biosensor by using a gate electrode functionalized with anti-IL-1β antibodies. We demonstrated the successful detection of cytokine IL-1β in the nM range, with a LOD of 1nM, proving its specificity when testing the device against possible interfering proteins. This is the first time an EGOT-based biosensor has been developed for the detection of IL-1β without the use of labels. However, the sensor does not meet the sensitivity features required for the detection of IL-1β under physio-pathological conditions, since the circulating levels of the cytokine are in the pM concentration range. The adoption of some strategies for its optimization is needed, such as implementing a biorecognition moiety with higher affinity for the analyte or working on improving the device architecture.

The monitoring of changes of additional device parameters, such as V_{th}, together with the most widely used signal S deriving from drain current changes, provides information about the sensing transduction mechanism. From the analysis of V_{th}, we could infer that the binding of the analyte to its antibody yields an increase in I_{DS} as a consequence of the shift of the

electrochemical potential of the gate electrode Considering all this together, EGOT devices are a very promising tool for simple, real-time, label-free sensing, which nevertheless in the present case need to be further optimized to meet the target requirements in terms of sensitivity and specificity.

4.5 REFERENCES

[1] A. Di Iorio, L. Ferrucci, E. Sparvieri, A. Cherubini, S. Volpato, A. Corsi, M. Bonafè, C. Franceschi, G. Abate, R. Paganelli, *Cytokine* **2003**, *22*, 198.

[2] Z. Dembic, *The Cytokines of the Immune System. In The Role of Cytokines in Disease Related to Immune Response*, Academic Press, **2015**.

[3] M. Kopf, M. F. Bachmann, B. J. Marsland, *Nat. Rev. Drug Discov.* **2010**, *9*, 703.

[4] N. Qian, X. Chen, S. Han, F. Qiang, G. Jin, X. Zhou, J. Dong, X. Wang, H. Shen, Z. Hu, *J. Cancer Res. Clin. Oncol.* **2010**, *136*, 709.

[5] M. Zhan, B. Xu, L. Zhao, B. Li, L. Xu, Q. Sun, J. Zhang, Z. Zhang, H. Chu, *Can. Respir. J.* **2018**.

[6] S. zhen Mai, C. jun Li, X. ying Xie, H. Xiong, M. Xu, F. qin Zeng, Q. Guo, Y. fang Han, *Int. Immunopharmacol.* **2018**, *58*, 103.

[7] I. Zaaber, S. Mestiri, H. Hammedi, H. Marmouch, S. Mahjoub, B. B. H. J. Tensaout, K. Said, *Immunol. Invest.* **2016**, *45*, 284.

[8] N. Motamedi Rad, M. Rezaeishahmirzadi, S. Shakeri, M. R. Abbaszadegan, M. Shekari, *Iran. J. Public Health* **2018**, *47*, 1364.

[9] P. Pani, I. Tsilioni, R. McGlennen, C. A. Brown, C. E. Hawley, T. C. Theoharides, E. Papathanasiou, *J. Periodontal Res.* **2021**, *56*, 501.

[10] M. Akdis, S. Burgler, R. Crameri, T. Eiwegger, H. Fujita, E. Gomez, S. Klunker, N. Meyer, L. O'Mahony, O. Palomares, C. Rhyner, N. Quaked, A. Schaffartzik, W. Van De Veen, S. Zeller, M. Zimmermann, C. A. Akdis, *J. Allergy Clin. Immunol.* **2011**, *127*, 701.

[11] L. Behboudi, M. Eizadi, *Jundishapur J. Chronic Dis. Care* **2017**, *6*.

[12] M. F. Manica-Cattani, L. Bittencourt, M. I. U. Rocha, T. D. Algarve, L. C. Bodanese, R. Rech, M. M. Machado, G. F. F. Santos, M. G. V. Gottlieb, C. H. A. Schwanke, J. E. C. Piccoli, M. F. F. Duarte, I. B. M. Cruz, *Mol. Cell. Endocrinol.* **2010**, *314*, 84.

[13] C. M. O'Neill, C. Lu, K. L. Corbin, P. R. Sharma, S. B. Dula, J. D. Carter, J. W. Ramadan, W. Xin, J. K. Lee, C. S. Nunemaker, *Endocrinology* **2013**, *154*, 3077.

[14] C. Franceschi, M. Bonafè, S. Valensin, F. Olivieri, M. De Luca, E. Ottaviani, G. De Benedictis, *Ann. N. Y. Acad. Sci.* **2000**, *908*, 244.

[15] W. De Jager, H. Te Velthuis, B. J. Prakken, W. Kuis, G. T. Rijkers, *Clin. Diagn. Lab. Immunol.* **2003**, *10*, 133.

[16] J. Rivnay, S. Inal, A. Salleo, R. M. Owens, M. Berggren, G. G. Malliaras, *Nat. Rev. Mater.* **2018**, *3*.

[17] S. H. Kim, K. Hong, W. Xie, K. H. Lee, S. Zhang, T. P. Lodge, C. D. Frisbie, *Adv. Mater.* **2013**, *25*, 1822.

[18] F. Torricelli, D. Z. Adrahtas, Z. Bao, M. Berggren, F. Biscarini, A. Bonfiglio, C. A. Bortolotti, C. D. Frisbie, E. Macchia, G. G. Malliaras, I. McCulloch, M. Moser, T. Q. Nguyen, R. M. Owens, A. Salleo, A. Spanu, L. Torsi, *Nat. Rev. Methods Prim.* **2021**, *1*.

[19] M. Berggren, A. Richter-Dahlfors, *Adv. Mater.* **2007**, *19*, 3201.

[20] L. Torsi, M. Magliulo, K. Manoli, G. Palazzo, *Chem. Soc. Rev.* **2013**, *42*, 8612.

[21] J. Rivnay, R. M. Owens, G. G. Malliaras, *Chem. Mater.* **2014**, *26*, 679.

[22] X. Strakosas, M. Bongo, R. M. Owens, *J. Appl. Polym. Sci.* **2015**, *132*, 41735.

[23] D. T. Simon, E. O. Gabrielsson, K. Tybrandt, M. Berggren, *Chem. Rev.* **2016**, *116*, 13009.

[24] J. Li, Y. Zhao, H. S. Tan, Y. Guo, C. A. Di, G. Yu, Y. Liu, M. Lin, S. H. Lim, Y. Zhou, H. Su, B. S. Ong, *Sci. Rep.* **2012**, *2*, 1.

[25] R. Giridharagopal, J. Guo, J. Kong, D. S. Ginger, *ACS Appl. Mater. Interfaces* **2021**, *13*, 34616.

[26] B. Schmatz, A. W. Lang, J. R. Reynolds, B. Schmatz, A. W. Lang, J. R. Reynolds, *Adv. Funct. Mater.* **2019**, *29*, 1905266.

[27] Y. Zhang, Q. Zeng, Y. Shen, L. Yang, F. Yu, *ACS Appl. Mater. Interfaces* **2020**, *12*, 56216.

[28] K. Chennit, N. Delavari, S. Mekhmoukhen, R. Boukraa, L. Fillaud, S. Zrig, N. Battaglini, B. Piro, V. Noël, I. Zozoulenko, G. Mattana, *Adv. Mater. Technol.* **2023**, *8*, 2200300.

[29] T. T. K. Nguyen, H. V Tran, T. T. Vu, S. Reisberg, V. Noël, G. Mattana, M. C. Pham, B. Piro, *Biosens. Bioelectron.* **2019**, *127*, 118.

[30] F. Giess, M. G. Friedrich, J. Heberle, R. L. Naumann, W. Knoll, *Biophys. J.* **2004**, *87*, 3213.

[31] B. Holzer, K. Manoli, N. Ditaranto, E. Macchia, A. Tiwari, C. Di Franco, G. Scamarcio, G. Palazzo, L. Torsi, *Adv. Biosyst.* **2017**, *1*.

[32] L. Sarcina, G. F. Mangiatordi, F. Torricelli, P. Bollella, Z. Gounani, R. Österbacka, E. Macchia, L. Torsi, *Biosensors* **2021**, *11*, 1.

[33] J. Dostálek, W. Knoll, *Biointerphases* **2008**, *3*, FD12.

[34] Y. Wang, A. Brunsen, U. Jonas, J. Dostálek, W. Knoll, *Anal. Chem.* **2009**, *81*, 9625.

[35] M. Berto, S. Casalini, M. Di Lauro, S. L. Marasso, M. Cocuzza, D. Perrone, M. Pinti, A. Cossarizza, C. F. Pirri, D. T. Simon, M. Berggren, F. Zerbetto, C. A. Bortolotti, F. Biscarini, *Anal. Chem.* **2016**, *88*, 12330.

[36] X. P. A. Gao, G. Zheng, C. M. Lieber, *Nano Lett.* **2010**, *10*, 547.

[37] C. Bonazza, J. Zhu, R. Hasler, R. Mastrogiacomo, P. Pelosi, W. Knoll, *Sensors (Switzerland)* **2021**, *21*, 1.

[38] J. P. Landry, Y. Ke, G.-L. Yu, X. D. Zhu, *J. Immunol. Methods* **2015**, *417*, 86.

[39] A. Sheinenzon, M. Shehadeh, R. Michelis, E. Shaoul, O. Ronen, *Int. J. Biol. Macromol.* **2021**, *184*, 857.

[40] A. M. Owyang, H. Issafras, J. Corbin, K. Ahluwalia, P. Larsen, E. Pongo, M. Handa, A. H. Horwitz, M. K. Roell, M. Haak-Frendscho, L. Masat, *MAbs* **2011**, *3*, 49.

[41] B. Burtscher, P. A. Manco Urbina, C. Diacci, S. Borghi, M. Pinti, A. Cossarizza, C. Salvarani, M. Berggren, F. Biscarini, D. T. Simon, C. A. Bortolotti, *Adv. Healthc. Mater.* **2021**, *2100955*.

[42] E. Macchia, K. Manoli, B. Holzer, C. Di Franco, M. Ghittorelli, F. Torricelli, D. Alberga, G. F. Mangiatordi, G. Palazzo, G. Scamarcio, L. Torsi, *Nat. Commun.* **2018**, *9*, 1.

[43] E. Macchia, F. Torricelli, P. Bollella, L. Sarcina, A. Tricase, C. Di Franco, R. Österbacka, Z. M. Kovács-Vajna, G. Scamarcio, L. Torsi, *Chem. Rev.* **2022**, *122*, 4636.

5 ANTI-CMV Ab BIOSENSOR

This chapter describes two utilities of OECT biosensors, one for analytical purposes for the detection of anti-CMV antibodies in real-time, and the other is for investigating the kinetics behind the binding event occurring at the sensing interface. Here is also described an elegant and versatile functionalization strategy for biorecognition unit immobilization.

5.1 INTRODUCTION

5.1.1 EGOTs for kinetics analysis

Affinity based biosensors that exploit surface-bound biomolecules as recognition elements for analytes in solution are becoming more important and widely used in clinical diagnostics and drug development studies. In recent years, Electrolyte Gated Organic Transistor (EGOT) devices have emerged as promising candidates for biosensing applications due to their inherent compatibility with biological systems and low-cost fabrication. Importantly, these devices offer the possibility to work label-free and therefore to perform the sensing without the need of secondary reagents to detect recognition/binding of the analytes. Historically, EGTs have been categorized into two distinct groups based on the ionic permeability of the semiconducting material employed. In Electrolyte-Gated Organic Field Effect Transistors (EGOFETs), the ionic interaction occurs solely at the interface between the electrolyte and the semiconductor, because the latter is impermeable to ions from the solution. On the contrary, when ion-permeable semiconductors are employed as channel materials, the ionic-electronic interaction takes place throughout the whole volume of the semiconductor. These devices are generally referred to as Organic Electrochemical Transistors (OECTs). These types of devices can directly translate the analyte-surface interaction into an electrical signal, allowing real-time detection of the binding event. In addition to sensing applications, this feature makes this kind of devices also a useful tool for studying the thermodynamics and binding kinetics of proteins, DNAs, and small molecules binding at the functionalized electrode surfaces.[1–5] Indeed, understanding the dynamic behaviour of the analyte-receptor interactions with the electrode surface is essential for optimizing the sensor performance, sensitivity, and response time.

Furthermore, many recent research efforts have been focused towards increasing the sensitivity and the limit of detection (LOD) reduction of these devices to allow detection of very low analyte concentrations, with reports down to single molecules (zM concentration range) for millimeters-sized devices based on EGOFET architecture.[6,7] In order to achieve such a high sensitivity, the channel or gate electrode functionalization strategies need to produce a high density of surface-bound receptors (~10^{11}–10^{12} sites cm^{-2}) for the target analyte, in order to achieve efficient binding with small sample volumes and low analyte concentrations.[6,8,9] However, when aiming to the study of binding thermodynamics and, especially, binding kinetics, special attention should be taken on the choice of the binding model used to interpret the experimental data.

5.1.2 CMV infection

Human Cytomegalovirus (HCMV) is a common pathogen representing one of the most widespread infections, especially in industrialized countries.[10] As with many other herpesviruses, it causes asymptomatic infection in immunocompetent subjects but can become a life-threatening disease in immunocompromised patients. The virus persists as a chronic infection, alternating between reactivation and latency, leading to constant activation of the immune system, with continuous production of a variety of pro-inflammatory mediators. In the elderly, this constant activation of the adaptive immune response can represent a high risk for all-cause mortality.[11,12] Several studies have reported an association between seropositivity to HCMV and age-related diseases such as cancer,[13–15] cardiovascular diseases,[16–18] neurodegenerative disease,[19] among others. Additionally, longitudinal studies describe infection by HCMV, and its seropositivity, to be part of the "immune risk profile" in the elderly, being a biomarker of several age-related diseases.[11,20] HMCV serological assays are also of great clinical importance when selecting blood donors and organ transplantation.[21]

Among the many viral proteins, Cytomegalovirus phosphoprotein 65 (CMV-pp65) is the major constituent of CMV virions and localizes predominantly to the nucleus after virus penetration and accumulates in both nucleus and cytoplasm as virus matures late in infection. This protein is one of the most immunogenic proteins, being a major target of humoral as well as cellular immune responses during infection, hence the measurement of level of immunoglobulin M and G antibodies in the serum can be used to determine the presence of an acute infection or past infection.[22–25]

In this work, we present an OECT-based biosensor with a flexible and efficient functionalization strategy for the transistor gate electrode. This method exploits the poly-histidine tag technology developed for recombinant proteins as a protein purification method. Upon optimization of the functionalization procedure, we demonstrate that it can be used to prepare a gate electrode with a high density of binding sites for the analyte. As case study, we test this method to fabricate an OECT biosensor for the detection of human cytomegalovirus (CMV) antibodies in solution, by decorating the gate electrode with the CMV-pp65 protein.

5.2 EGOT DEVELOPMENT

5.2.1 Transistor Fabrication

For the OECT-based biosensors, quartz test patterns were used, with 1 cm^2 of total area (as substrates purchased from "Fondazione Bruno Kessler"- FBK, Trento, Italy) with four interdigitated source and drain electrodes pairs, with a width/length ratio (W/L) equal to 50.

Each quartz test patterns was initially rinsed with acetone, in order to remove the photoresist layer, and dried with a gentle nitrogen flow. This step was followed by a cleaning step in piranha solution (98 % w/w H_2SO_4 and 30 % v/v H_2O_2 ratio of 1:1) for 1 minute at 150 °C and rinsed abundantly with water before the PEDOT:PSS deposition. The PEDOT:PSS used was prepared with 0.2% w/w curing agent and 5% w/w of dimethyl sulfoxide (DMSO) and then diluted 200 times in water. The final PEDOT:PSS solution was then sonicated before use for at least 10 minutes, and deposited on the substrate by drop casting, followed by 30 min of thermal curing in the oven at 120 °C.

5.2.2 Gate Functionalization

The gate functionalization strategy was adapted from the procedure reported by Giess F. *et al.*, explained in more detail in Chapter 2.1.4.[26] Our method included an additional step in which the gate electrode was incubated with oligo(ethyleneglycol)-terminated alkanethiols (OEG). The order of OEG addition with respect to the stepwise addition of the other reagents was evaluated by testing three different protocols:

Protocol I:

(i) Overnight incubation in 5 mM DTSP in DMSO.
(ii) Incubation in 100 μM OEG for 30 minutes.
(iii) Incubation in 80 mM ANTA, buffered at pH 9.8, for 2 hours.

Protocol II:

(i) Overnight incubation in 5 mM DTSP in DMSO.
(ii) Incubation in 80 mM ANTA, buffered at pH 9.8, for 2 hours.
(iii) Incubation in 100 μM OEG for 30 minutes.

Protocol III:

(i) Overnight incubation in 5 mM DTSP in DMSO.
(ii) Incubation in 80 mM ANTA, buffered at pH 9.8, for 2 hours.

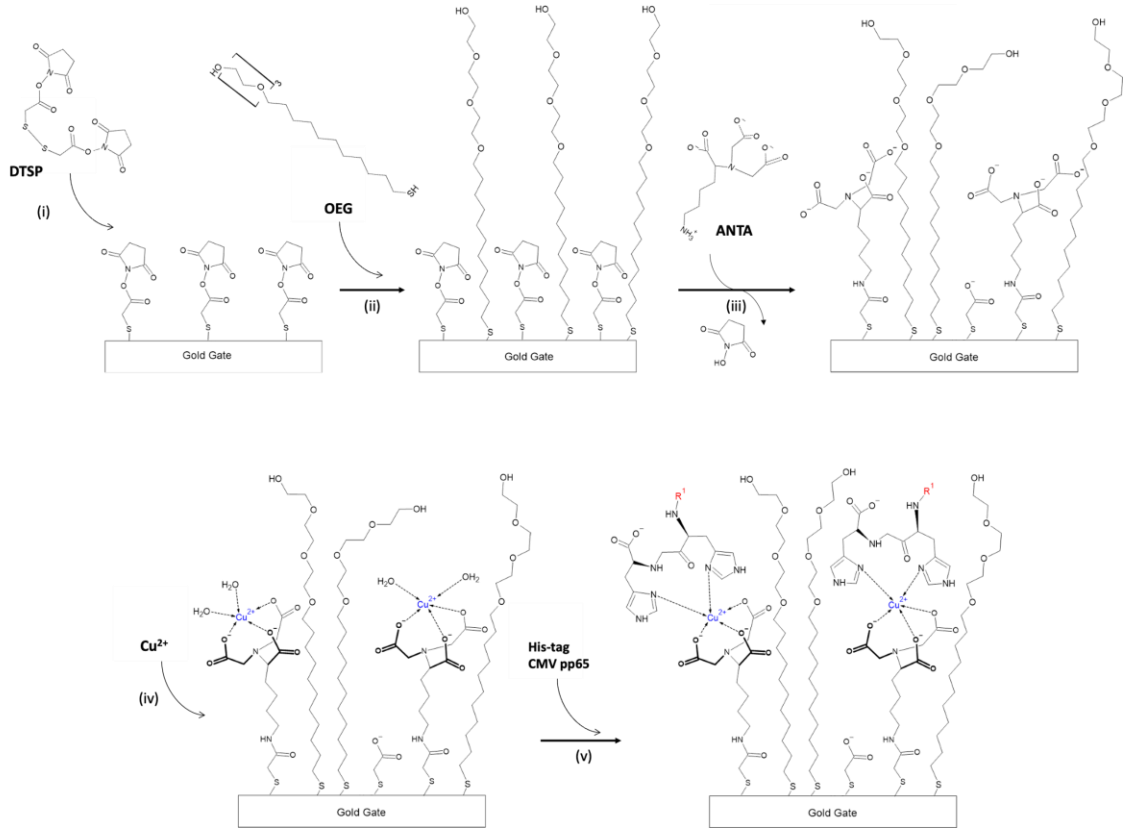

Figure 5.1. Schematic drawing of the gate functionalization procedure *Protocol I* from step (i) to step (v). Here it is depicted the metal ion Cu^{2+} interacting with the poly-Histidine of the CMV pp65 (taken from Chapter 2.1.4).

Eventually, the protocol used in the functionalization of the gate electrode for biosensing experiments was *Protocol I* (**Figure 5.1**), following the next procedure: (i) incubation of the gold electrode in 5 mM 3,3′-dithiodipropionic acid di(N-hydroxysuccinimide ester) (DTSP) in DMSO overnight, followed by (ii) incubation in 100 µM oligo(ethylene glycol)-terminated undecanethiol (OEG) for 30 minutes; (iii) incubation in 80 mM Nα,Nα-bis(carboxymethyl)-L-lysine hydrate (ANTA), pH 9.8, for 2 hours; (iv) incubation in 40 mM $CuSO_4$, in 50 mM acetate buffer pH 5.5 for 30 minutes; (v) incubation in 0.05 mg mL^{-1} His-tag-CMV-pp65 in 50 mM phosphate buffer, pH 7.4 for 3 hours, followed by washing step with buffer and gentle drying with nitrogen. (vi) Final incubation in 0.1 mg mL^{-1} BSA and 0.05% Tween20 in 50 mM phosphate buffer pH 7.4 for 30 minutes, and then the gate was inserted into the microfluidics system. All incubation steps were performed at room temperature.

5.2.3 Electrochemical Characterization of the functionalization process

The gate functionalization was monitored by Cyclic Voltammetry (CV) using a CH Instrument potentiostat 760c model. We performed the measurements in a 3-electrodes setup, using gold wire as the working electrode (WE), platinum wire as the counter electrode (CE), and Ag/AgCl as reference electrode (RE), working in 5 mM $K_3[Fe(CN)_6]$ and 1 M KCl solution, sweeping

the potential between –0.2 V and +0.6 V at a scan rate of 0.050 V s^{-1}. Here, a gold wire was used as working electrode to study the functionalization process.

Upon functionalization of the electrode surface with the OEG/protein layers, the charge transfer resistance between the redox probe and the electrode was increased, which reduced the faradaic current recorded with respect to the bare gold electrode (**Figure 5.2 A**). In the absence of OEG, the amount of surface-bound CMV-pp65 protein is not enough to fully cover the electrode, which results in the presence of faradic peaks in the cyclic voltammetry characterization displaying intensity and peak positions comparable to those recorded for the same surface before protein immobilization. (**Figure 5.2 B**). During the biosensing experiment, these exposed surfaces could lead to non-specific adsorption processes at the bare gold surface, leading to a non-specific response. Conversely, incubation with the OEG effectively passivates the electrode surface in the areas that are not covered by the CMV-pp65, as demonstrated by the large faradaic current reduction (**Figure 5.2 A**).

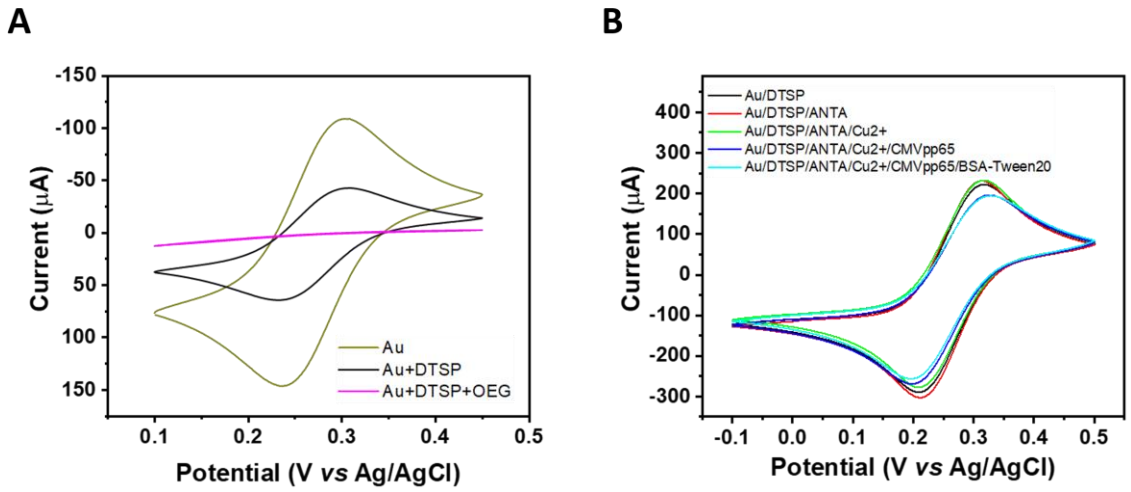

Figure 5.2. Cyclic voltammetry of the functionalized Au electrode using $K_3[Fe(CN)_6]$ as redox probe. **A)** Monitoring surface coverage with OEG (*Protocol I*), **B)** Monitoring surface coverage in the absence of OEG (*Protocol III*).

5.2.4 Optical Validation of Functionalization Process

The gate functionalization was monitored by Fiber optic surface plasmon resonance (FO-SPR), explained in more detail in Chapter 2. These experiments were performed in collaboration with Professor W. Knoll's group from the Austrian Institute of Technology (AIT). The real-time monitoring started from the FO coated with the SAM in 50 mM Phosphate Buffer pH 7.4. In order to optimize the amount of CMV-pp65 attached to the electrode (i.e. optimize the number of binding sites for the anti-CMV Ab), the effect of the OEG on the functionalization process was evaluated by testing three different experimental protocols detailed in the previous section.

To do this, each step of the functionalization process was optically monitored by FO-SPR in real-time as shown in **Figure 5.3**. Recent work demonstrated that plasmonic fiber optic coated with gold could be used to monitor mass changes on the gold surface with high sensitivity, hence making it a suitable alternative to prism used in standard SPR setups.[27] The optical signal detection is based on the detuning of the resonant optical excitation of propagating surface plasmons (SP) at the metal–electrolyte interface due to local refractive index change, which can be associated with mass adsorption at the metal surface.[28,29] Hence, from the FO-SPR time race it is possible to estimate the amount of protein bound to the gold surface in terms of electrode surface coverage (see Chapter 2, eq. 2.1).

The Au-coated FO was initially incubated with 50 mM phosphate buffer, 0.1 mg mL^{-1} BSA, 0.05% w/v Tween 20 at pH 7.4 until reaching a stable optical signal that was taken as baseline. Then, the buffer solution was replaced with a Cu^{2+} solution in order to Cu-load the ANTA, followed by a washing step with buffer and before incubation with a 600 nM His-tagged CMV-pp665 protein solution. At this stage, buffer solution was then used to wash any protein not bound to the Cu^{2+}–ANTA binding sites. The resonance wavelength (λ_{SPR}) shift with respect to the initial baseline is proportional to the amount of CMV-pp665 bound to the surface. The stability and the non-specific adsorption of this layer was then tested by incubation with a 0.1 mg mL^{-1} BSA, 0.05% w/v Tween 20, pH 7.4 solution until equilibration of the optical signal. Washing with clean buffer restores the optical signal obtained at the previous step. Finally, the binding of the anti-CMV antibodies was demonstrated, by incubating the FO with a 100 nM anti-CMV Ab solution, which generated a shift in the λ_{SPR} signal.

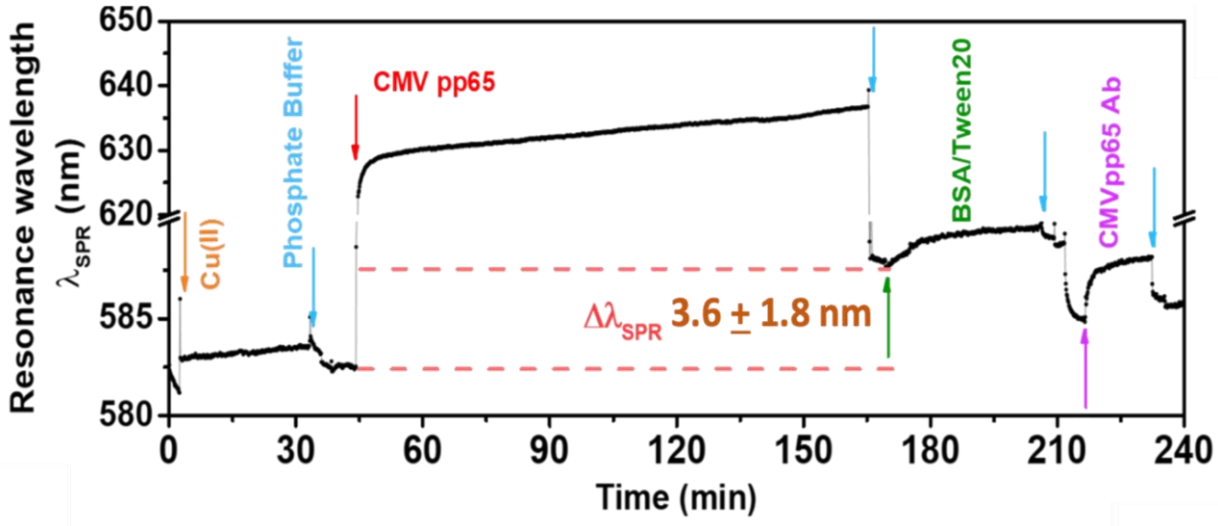

Figure 5.3. SPR kinetics of the gold surface functionalization process. Each reagent injection is represented by coloured arrows.

From the analysis of the shift of the λ_{SPR}, we can estimate the surface mass density (see Chapter 2, eq. 2.1), yielding the following results: a higher coverage is obtained in the absence of the OEG layer (*protocol III*), when compared with both protocols that included the formation of the OEG layer (*protocol I* and *II*), likely because of the steric hindrance due to the long OEG chains. On the other hand, the OEG addition before the incubation with the ANTA (*protocol I*) yielded slightly higher CMV-pp665 surface densities, with respect to changing the addition order of these two reagents (*protocol II*). These results are the average of 3 independent experiments for each protocol, with the corresponding standard error of the mean (SEM).

Eventually, on the basis of these experimental results, *protocol I* was selected to be implemented as gate electrode functionalization strategy for anti-CMV Ab detection with the OECT devices. This protocol yielded an average CMV-pp65 adsorbed density of $(9.5\pm0.3)\times10^{11}$ molecules cm^{-2}, validating the use of this His-tagged based method to achieve high receptor densities of the electrode surface. In fact, this value is similar with the surface coverage reported for other functionalization strategies that yield high receptor densities on the surface and characterized by SPR ($4–8\times10^{11}$ molecules cm^{-2}).[6,9,26,30]

5.2.5 Microfluidics System Setup

After a thorough characterization and optimization of the gate functionalization process, we proceeded with the integration of the functionalized gate and the substrate into a flexible bi-adhesive microfluidics. This microfluidics were designed and produced by our collaborators Fabio Biscarini and Pierpaolo Greco at the Italian Institute of Technology (IIT, Ferrara) and University of Ferrara, respectively. This double sided adhesive microfluidic layer assembles the quartz substrate, where the OSC was deposited onto the interdigitated D and S electrodes, with the silicon gold coated gate into a top-gated configuration.

The initial buffer was 50 mM phosphate buffer pH 7.4 containing 0.1 mg mL^{-1} BSA and 0.05% Tween 20, which flowed through the microfluidics system dispensed by a peristaltic pump, working at 15 μL min^{-1}.

5.2.6 OECT Electrical Characterization

Electrical measurements were performed inside a Faraday cage, using Agilent B2912A Source Measurement Unit (SMU). Using a 50 mM phosphate buffer pH 7.4 solution as gating electrolyte, the electrical performances of the OECT were characterized recording transfer curves by sweeping the gate voltage (V_{GS}) from 0 V to 0.6 V, at a fixed drain voltage (V_{DS}) of –0.2 V (**Figure 5.4**). The results show that even if the gate electrode surface is covered by several layers of different molecules (because of the functionalization procedure), the OECT

device still presents a satisfactory drain current (I_{DS}) modulation as a function of the V_{GS} applied potential. Hence, for the real-time bio-sensing experiment the device was operated at mild applied potentials, with V_{GS} = +0.5 V and V_{DS} = –0.2 V, corresponding to a transconductance (g_m) ≈75 μS.

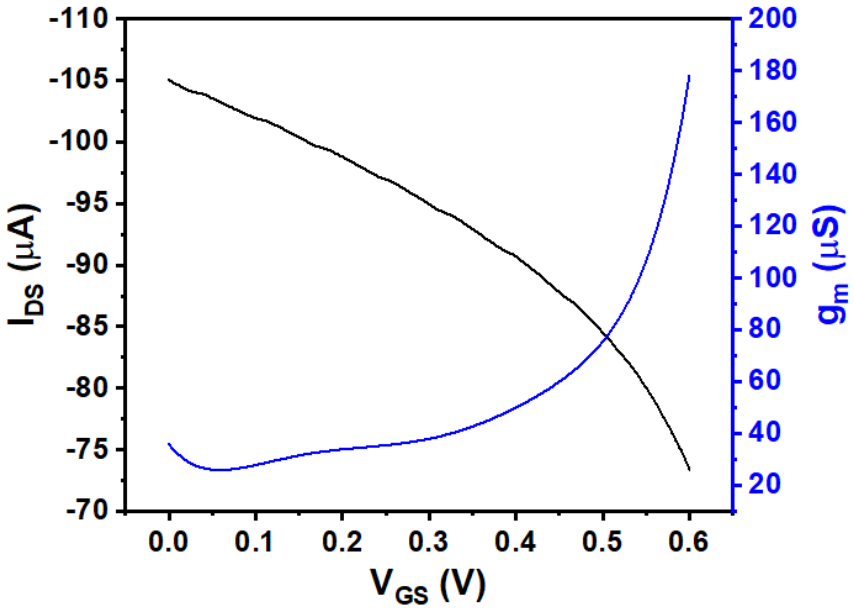

Figure 5.4. Representative transfer curve of the OECT device (black trace), together with the corresponding transconductance curve (blue trace). The measurement was performed in 50 mM phosphate buffer pH 7.4 as electrolyte, with the functionalized gold gate and V_{DS} = –0.2 V.

5.3 BIOSENSOR RESPONSE

5.3.1 Real-time Sensing

The biosensing of the anti-CMV Ab in buffered solutions was performed by continuously monitoring the variations of I_{DS} *vs.* time, at constant V_{DS}= –0.2 V and V_{GS} = +0.5 V, for concentrations ranging from 1 nM to 500 nM of anti-CMV Ab in 50 mM phosphate buffer, 0.1 mg mL^{-1} BSA, 0.05% w/v Tween 20 at pH 7.4. Initially, the device was stabilized by flowing buffer solution through the microfluidic systems, in order to obtain a constant I_{DS} current (baseline); then the device was exposed to increasing concentrations of anti-CMV Ab by injecting the different standard solutions. **Figure 5.5 A** (grey trace) shows a typical response of the OECT sensor, where I_{DS} decreased upon analyte binding over time. After the last standard sample, buffer solution (without analyte) was injected again into the microfluidic system, in order to induce the dissociation of the bound analyte. Indeed, an increase of the current was observed, indicating the reversibility of the binding process, although in the investigated time window we do not observe full recovery of the initial drain current value.

The decrease in I_{DS} magnitude is proportional to the anti-CMV Ab concentration, hence a calibration curve (**Figure 5.5 B**) was constructed by measuring the sensor response in the equilibrium regime of each concentration. The response was quantified in terms of signal (S), defined as the relative change of the current at a certain analyte concentration with respect to the initial value (in the absence of the analyte) ($S = -\Delta I_{DS} / I_{DS[0]}$). This curve shows a non-linear monotonic trend with increasing concentration of anti-CMV Ab, demonstrating that the device is sensitive to changes in analyte concentration in the nanomolar concentration range. From these data, a quantitative relationship between S and [anti-CMV Ab] was obtained by fitting the signal the Langmuir isotherm model, yielding an estimated binding constant $K_L = (1.2 \pm 0.2)\times10^7$ and an estimated maximum signal $S_{max} = 0.821$ (**Figure 5.5 B**). Furthermore, because the recorded signal is proportional to the amount of anti-CMV Ab protein bound to the gate electrode surface, it is possible to convert the signal S into the surface fraction coverage (θ), defined as $\theta = S/S_{max}$, where S_{max} is the maximum signal estimated from the Isotherm fitting.

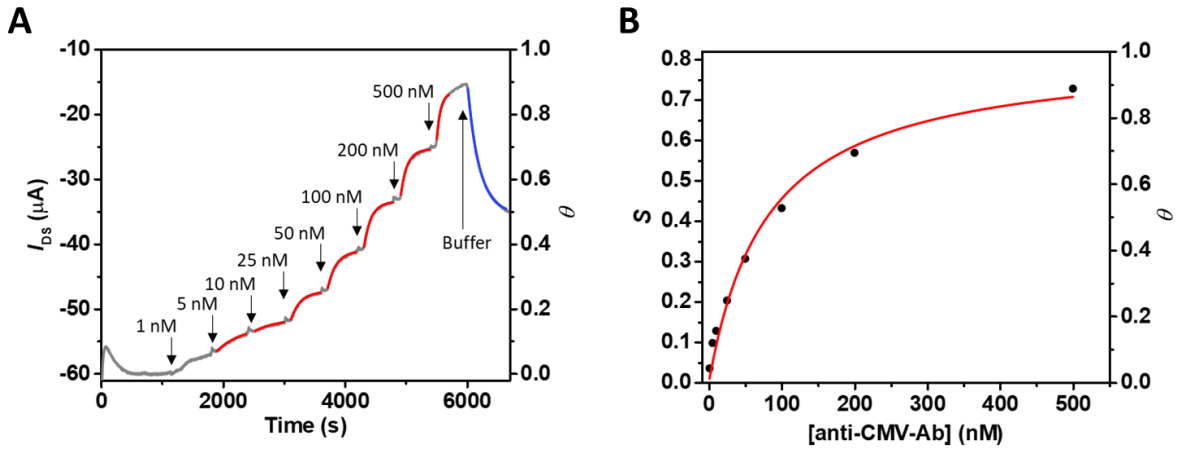

Figure 5.5. Real-time electrical sensing of the binding of anti-CMV Ab to CMV-pp65 immobilized onto the gate electrode surface, using an OECT-based biosensor. **(A)** Sensor current variation to increasing concentrations of anti-CMV Ab, plotted as I_{DS} *vs.* time (grey trace). The labeled arrows indicate the injection of the analyte standard solutions and of clean buffer. Red traces correspond to the fitting of the time-dependent θ changes (left Y axis) by kinetic analysis based on the two-compartment steady-state model. The blue trace represents the fitting of the un-binding phase with a first-order (exponential) model. **(B)** Sensor calibration curve expressed in terms of signal (S) and the corresponding surface coverage (θ) as a function of anti-CMV Ab concentration. The red trace represents the fitting with the Langmuir isotherm model, giving an estimated $K_L = (1.2 \pm 0.2)\times10^7$ and $S_{max} = 0.821$.

The theoretical limit of detection (LOD) by averaging the fluctuation of the noise in the absence of the analyte plus three times its standard deviation: $S_{noise} + 3\sigma$. This value was converted in

[anti-CMV Ab] using the Langmuir isotherm curve reported in **Figure 5.5 B**, giving a LOD = 0.5 nM.

5.3.2 Control Experiments

Non-specific binding interactions at the channel or at gate electrode surfaces are a common source of interference in the measured signal of a sensing experiment. Therefore, two different types of control experiments were performed to assess the specificity of the biosensor response to anti-CMV Ab. To this end, we recorded the drain current changes upon exposure to a solution containing 100 nM anti-IL-1β, to test the device response to a different antibody, and 100 nM IL-6, to test the response to a molecule that has potentially increased levels in elderly subjects and could be an interferent.[31] The non-specific response to 100 nM anti-IL-1β (**Figure 5.6**, light green background) has a significant signal, while the response to 100 nM IL-6 is practically negligible (dark green background); however, both these signals are much lower than the specific response to anti-CMV Ab (pink background) at the same concentration, indicating the satisfactory selectivity of the biosensor.

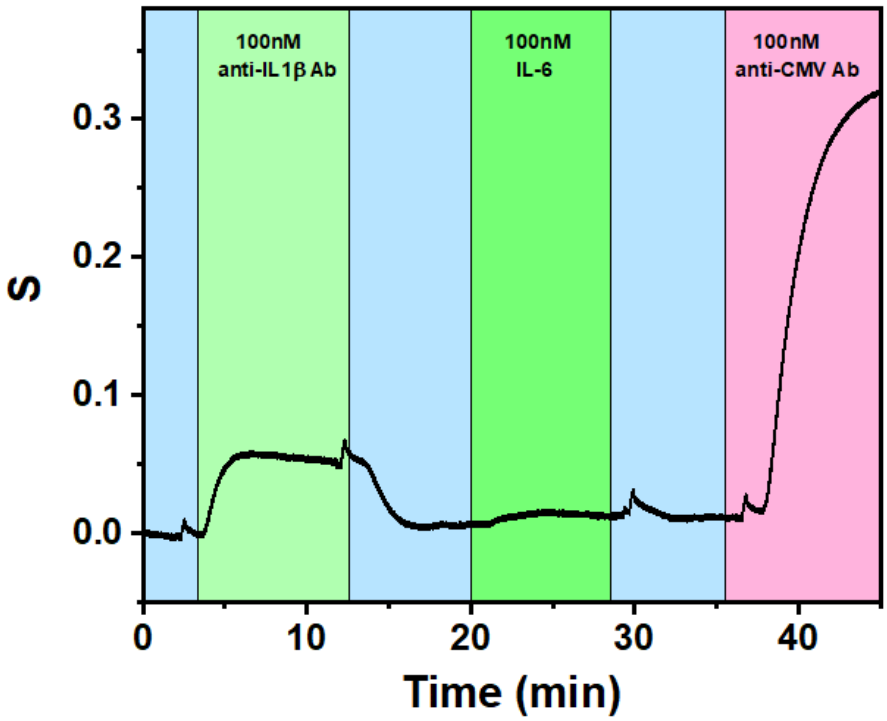

Figure 5.6. Real-time electrical monitoring of the OECT-based biosensor response to proteins different than Anti-CMV Ab: anti-IL-1β Ab and IL-6 (light and dark green, respectively). Response to the analyte anti-CMV Ab at the same concentration (pink) is then recorded as a comparison. Blue background represents the washing steps buffer solution.

5.3.3 Kinetics Analysis

The real time data obtained from the OECT sensor integrated into the microfluid system allows to extract information about the dynamic of the binding process. In this context, the so-called 'two-compartment model' is one of the most widely exploited models for describing the binding kinetics of analytes in solution to surface-immobilized ligands, under a constant flow rate of solution.[32,33] Although commonly applied for the interpretation of SPR kinetics data, it has been applied also in the field of electronic biosensors.[1,5] In this model, the overall binding kinetics is treated as two-step process:

$$A_{(bulk)} \xleftrightarrow{k_m} A_{(s)} + B \xleftrightarrow{k_{on},k_{off}} AB$$

The first step is the transport of the analyte (A, the antibody in this case) from the bulk of the solution (outer compartment) to the region close to the sensor surface (inner compartment). This step is followed by the reaction of the analyte with the binding site (B) on the surface of the sensor.[32,33] Here, k_{on} is the second order adsorption rate constant, k_{off} is the first order desorption rate constant and k_m is the mass transport coefficient describing the diffusive movement of the analyte between the two compartments. This model is attractive because it can be formulated in terms of a relatively simple system of ordinary differential equations:[34]

$$V\frac{dC_s}{dt} = S\left[k_m L_D(C_0 - C_s) - k_{on}C_s P_0(1-\theta) + k_{off}P_0\theta\right] \quad (5.1)$$

$$\frac{d\theta}{dt} = k_{on}C_s(1-\theta) - k_{off}\theta \quad (5.2)$$

The model approximates the bulk (outer compartment) concentration C_0 as constant over time, while the concentration of the analyte near sensor surface (C_s) changes over time because the analyte is transported from the bulk of the solution and because it binds/dissociates from the ligand immobilized on the sensor surface. Here, θ is the electrode surface coverage which is proportional to the amount of analyte bound to the receptor, P_0 is the maximum concentration of available binding sites (mol cm^{-2}), V (cm^3) is the volume of the inner compartment and S (cm^2) is the surface area of the sensor and L_D (cm) is the height of the inner compartment above the sensor surface.

Although no analytical solutions are known for systems formed by Eq. (5.1)–(5.2), and so it can only be solved by numerical integrations, under certain conditions it can be simplified, allowing to obtain analytical solutions. If the analyte transport to the sensor surface is much faster than the binding reaction, the analyte concentration can be considered constant ($C_s = C_0$) during the whole binding process: the model is then described only by Eq. (5.1) and results in

a simpler first order binding kinetic (this model is often referred as 'rapid mixing model'). On the other hand, mass transport effects will influence the binding kinetics when the association rate is similar to or faster than the mass transport rate. In this situation, the term k_m ($C_0 - C_s$) cannot be neglected anymore and therefore the model depends on four unknown parameters: k_{on}, k_{off}, k_m and the ratio V/S (equivalent to the height of the inner compartment). However, previous studies demonstrated that the solutions to Eq. (5.1)–(5.2) are insensitive to the value of V/S; in fact, works by Myszka *et al.* and Sigmundsson *et al.* showed that once the binding or dissociation is initiated, C_s changes rapidly over a very short period of time (with respect to the binding kinetic timeframe) and then very slowly thereafter.[34,35] Furthermore, while this rapid change in C_s is occurring, there is a negligible change in θ. This behavior means that a quasi-steady-state approximation can be made where $dC_s/dt = 0$.[34,36] In this condition, V/S drops out of Eq. (5.1), explaining why the value of the ratio does not affect the final solution.

Under quasi-steady-state approximation, the model can be described by a single differential equation with the following form:

$$\frac{d\theta}{dt} = k_{on}\left(\frac{k'_m C_0 + k_{off}\theta}{k'_m + k_{on}(1-\theta)}\right)(1-\theta) - k_{off}\theta \qquad (5.3)$$

where $k_m' = k_m L_D/P_0$ ($M^{-1}\ s^{-1}$), corresponding to the coefficient that can be extracted directly from the fitting procedure (as described below). This factor can still be considered as a mass transfer coefficient, but its numerical value also depends on the initial concentration of binding sites P_0. The Eq. (5.3) describes the formation of analyte-ligand complex under partially limiting mass transport conditions. Sigmundsson *et al.* showed that this differential equation has an analytical solution which takes the form:[35]

$$\theta = K_1\left[1 - \frac{1}{K_2}W\left(K_2 e^{(K_2 - K_3 k_{off}\, t)}\right)\right] \qquad (5.4)$$

Where W represents the Lambert W function and

$$K_1 = \frac{k_{on}C_0}{k_{on}C_0 + k_{off}} \qquad (5.5)$$

$$K_2 = \frac{{k_{on}}^2 C_0}{(k_{on}C_0 + k_{off})k'_m + k_{on}k_{off}} \qquad (5.6)$$

$$K_3 = \frac{(k_{on}C_0 + k_{off})^2 k_m}{k_{off}[(k_{on}C_0 + k_{off})k'_m + k_{on}k_{off}]} \qquad (5.7)$$

Hence the exact solution Eq. (5.4) depends on four parameters C_0, k_{on}, k_{off} and k'_m. The surface coverage θ equals 0 at t = 0 s, while for a very long reaction time, the equilibrium value for θ is equal to K_1:

$$\theta_{eq} = K_1 = \frac{k_{on}C_0}{k_{on}C_0 + k_{off}} \qquad (5.8)$$

Eq. (5.8) describes the same equilibrium condition obtained from the Langmuir isotherm and from the rapid mixing model (see above explanation), as would be expected given that the constant flow of analyte solution tends toward a final constant concentration value equal to C_0.

As a first step into the analysis of the experimental kinetic traces, the data were initially fitted using the rapid mixing model and hence with simple exponential functions to extract an observed rate constant (k_{obs}) at each concentration of anti-CMV Ab (**Figure 5.7**). The results show a non-linear trend of k_{obs} versus C_0 which is in contrast to the relationship obtained from the model where $k_{obs} = k_{on}\ C_0 + k_{off}$, suggesting that at least in the low nanomolar regime the recorded kinetics may be affected by mass transport limitations.

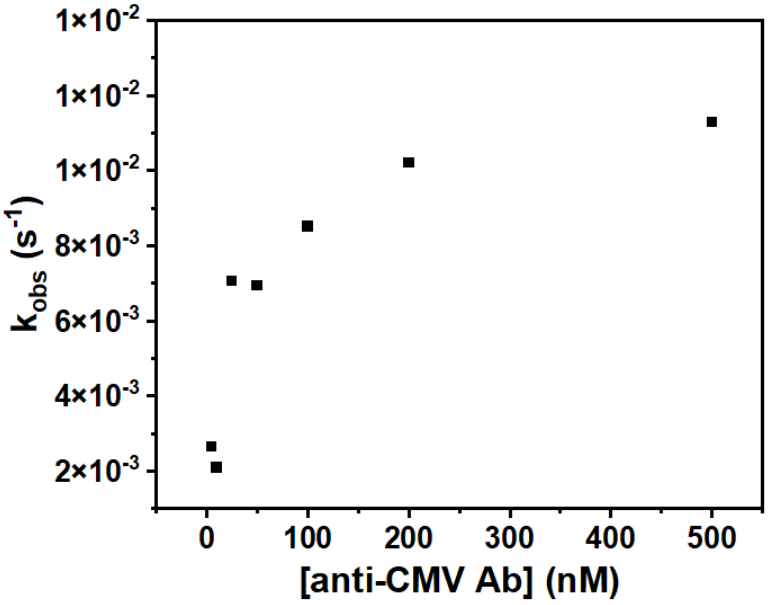

Figure 5.7. k_{obs} *vs.* [anti-CMV Ab] from the simple exponential function for binding kinetics analysis.

Therefore, we performed the analysis of the kinetic data considering the possible effect of the mass transfer rate. The analytical solution for the quasi-steady state model Eq. (5.4) was then used to fit the kinetic data of θ versus time, recorded at different initial concentrations of antibodies, using k_{on}, k_{off} and k_m as fitting parameters. The results of the curve fitting procedure are shown in **Figure 5.5 A** as red traces overlayed with the experimental ones (gray traces). In

order to obtain a more consistent estimate for the rate constants, the values of the parameters obtained at each concentration C_0 were averaged. The fitting procedure yielded a k_{on}=(5.7±0.9)×10^4 M^{-1} s^{-1}, k_{off} =(3.7±0.9)×10^{-3} s^{-1} and k_m=(3.8±0.3)×10^5 M^{-1} s^{-1}.

The k_{on} value obtained is somewhat lower with respect to the k_{on} values typically measured in antigen-antibody pairs in solution (~10^5–10^6 M^{-1} s^{-1}),[37–39] whilst the obtained k_{off} is in line with characteristic values reported in the literature (~10^{-4}–10^{-3} s^{-1}).[37–39] According to the kinetic model, the ratio k_{on}/k_{off} =(1.5±0.2)×10^7 closely matches the value of the binding association constant (K_L) obtained from the Langmuir isotherm reported above, further supporting the application of the two-compartment model to describe this binding process. Furthermore, the smaller value of k_{on}=(5.7±0.9)×10^4 M^{-1} s^{-1} with respect to the ones observed in kinetic experiments in solution hints to a slightly reduced binding affinity on the electrode surface with respect to solution.

Finally, after the binding process with the highest anti-CMV Ab concentration, the system was washed with buffer solution in order to allow the complex anti-CMV Ab/CMV-pp65 to dissociate. The kinetic trace for this dissociation phase could be fitted with a mono-exponential function, assuming a first order kinetics (**Figure 5.5 A**, blue trace). The result allows to estimate the value of k_{off} independently from the fitting procedure used with the association phase curves, yielding a value of k_{off} = (4.93±0.01)×10^{-3} s^{-1}, again very similar to the one obtained previously and further corroborating the adequacy of the binding model to our experimental data. Furthermore, this result suggests that for the 500 s after the injection of pure buffer, the recorded dissociation rate is much slower than the transport rate and hence diminishing the effect of the mass transport rate and effectively reducing this initial phase to a pseudo-first order kinetics.

Overall, the kinetic analysis reveals that while k_m is larger than k_{on}, the difference between them is not very large (k_m/k_{on}≈6.5). This suggests the presence of potential effects due to mass transport limitation in the observed rate binding constant, especially at the beginning of the experiment (where the binding sites are essentially empty) and with the lower concentration of anti-CMV Ab. Then, during the course of the experiment, the electrode surface becomes more and more saturated, and the injected samples have a higher starting concentration, reducing the influence of the mass transport. Here we note that generally, biosensors based on electrolyte gated transistor devices are effectively used to detect analytes at very low concentrations (even sub-pico o nanomolar) and therefore require a high density of binding sites to reach such a high

sensitivity. Hence, when kinetic data is recorded under these experimental conditions, the possible effects due to mass transport limitations should be taken into account.

5.4 CONCLUSIONS

In conclusion, in this chapter we report the fabrication of an OECT-based biosensor in which we exploited the poly-histidine tag technology to functionalize the gate electrode with a specific receptor for a target analyte. As a case study, we applied this methodology for the detection of anti-CMV antibodies in solution. We demonstrated that it is possible to obtain high receptor densities on the surface of the gate electrode, allowing to obtain high sensitivity in the nanomolar concentration range for anti-CMV Ab. The poly-histidine tag technology is a workhorse of recombinant protein purification technologies, hence making this functionalization strategy very flexible and adaptable to a large variety of analyte/receptor pairs. Furthermore, by integrating the OCET sensor into a microfluidic system, we were able to perform the sensing in real-time by continuously monitoring the current variation as a consequence of analyte binding to the gate electrode. The analysis of the kinetic traces demonstrated that mass transport limitations can influence the observed association rate constants when the measurements are performed at low analyte concentration together with a high density of binding sites on the gate electrode.

5.5 REFERENCES

[1] X. Duan, Y. Li, N. K. Rajan, D. A. Routenberg, Y. Modis, M. A. Reed, *Nat. Nanotechnol.* **2012**, *7*, 401.

[2] M. Larisika, C. Kotlowski, C. Steininger, R. Mastrogiacomo, P. Pelosi, S. Sch, S. F. Peteu, C. Kleber, C. Reiner-rozman, C. Nowak, W. Knoll, **2015**, 13245.

[3] M. Berto, S. Casalini, M. Di Lauro, S. L. Marasso, M. Cocuzza, D. Perrone, M. Pinti, A. Cossarizza, C. F. Pirri, D. T. Simon, M. Berggren, F. Zerbetto, C. A. Bortolotti, F. Biscarini, *Anal. Chem.* **2016**, *88*, 12330.

[4] P. A. Manco Urbina, M. Berto, P. Greco, M. Sensi, S. Borghi, M. Borsari, C. A. Bortolotti, F. Biscarini, *J. Mater. Chem. C* **2021**, *9*, 10965.

[5] M. L. Hammock, O. Knopfmacher, B. D. Naab, J. B. H. Tok, Z. Bao, *ACS Nano* **2013**, *7*, 3970.

[6] E. Macchia, K. Manoli, B. Holzer, C. Di Franco, M. Ghittorelli, F. Torricelli, D. Alberga, G. F. Mangiatordi, G. Palazzo, G. Scamarcio, L. Torsi, *Nat. Commun.* **2018**, *9*, 1.

[7] E. Macchia, K. Manoli, C. Di Franco, R. A. Picca, R. Österbacka, G. Palazzo, F. Torricelli, G. Scamarcio, L. Torsi, *ACS Sensors* **2020**, *5*, 1822.

[8] F. Torricelli, D. Z. Adrahtas, Z. Bao, M. Berggren, F. Biscarini, A. Bonfiglio, C. A. Bortolotti, C. D. Frisbie, E. Macchia, G. G. Malliaras, I. McCulloch, M. Moser, T.-Q. Nguyen, R. M. Owens, A. Salleo, A. Spanu, L. Torsi, *Nat. Rev. Methods Prim.* **2021**, *1*.

[9] L. Sarcina, L. Torsi, R. A. Picca, K. Manoli, E. Macchia, *Sensors* **2020**, *20*, 3678.

[10] M. J. Cannon, D. S. Schmid, T. B. Hyde, *Rev. Med. Virol.* **2010**, *20*, 202.

[11] J. J Heath, M. D Grant, *Cells* **2020**, *9*, 766.

[12] J. Hesson, N. Fudge, M. Grant, *Viruses* **2021**, *13*, 2321.

[13] J. Geisler, J. Touma, A. Rahbar, C. Söderberg-Nauclér, K. Vetvik, *Cancers (Basel).* **2019**, *11*, 1842.

[14] H. Foster, K. Piper, L. Depledge, H. F. Li, J. Scanlan, Y. Jae-Guen, M. Boeckh, C. Cobbs, *Neuro-Oncology Adv.* **2019**, *1*, 1.

[15] C. S. Nauclér, J. Geisler, K. Vetvik, *Oncotarget* **2019**, *10*, 4333.

[16] A. Blum, A. Peleg, M. Weinberg, *Clin. Exp. Med.* **2003**, *3*, 157.

[17] C. Grahame-Clarke, N. N. Chan, D. Andrew, G. L. Ridgway, D. J. Betteridge, V. Emery, H. M. Colhoun, P. Vallance, *Circulation* **2003**, *108*, 678.

[18] E. M. Hamilton, N. E. Allen, A. J. Mentzer, T. J. Littlejohns, *J. Infect. Dis.* **2022**, *225*, 1179.

[19] N. S. Lurain, B. A. Hanson, J. Martinson, S. E. Leurgans, A. L. Landay, D. A. Bennett, J. A. Schneider, *J. Infect. Dis.* **2013**, *208*, 564.

[20] P. J. E. J. van de Berg, A. van Stijn, I. J. M. ten Berge, R. A. W. van Lier, *J. Clin. Virol.* **2008**, *41*, 213.

[21] S. Landolfo, M. Gariglio, G. Gribaudo, D. Lembo, *Pharmacol. Ther.* **2003**, *98*, 269.

[22] C. S. Morello, L. D. Cranmer, D. H. Spector, *J. Virol.* **1999**, *73*, 7678.

[23] M. R. Schleiss, *J. Virus Erad.* **2016**, *2*, 198.

[24] Y. Nikmanesh, M. H. Karimi, R. Yaghobi, S. M. Marashi, M. Mahmoudi, A. Moravej, S. Shahmahmoodi, *Iran.J.Immunol* **2019**, *16*.

[25] M. Agnarsdóttir, S. Popova, I. Alafuzoff, *PLoS One* **2019**, *14*.

[26] F. Giess, M. G. Friedrich, J. Heberle, R. L. Naumann, W. Knoll, *Biophys. J.* **2004**, *87*, 3213.

[27] R. Hasler, C. Reiner-Rozman, S. Fossati, P. Aspermair, J. Dostalek, S. Lee, M. Ibáñez, J. Bintinger, W. Knoll, *ACS Sensors* **2022**, *7*, 504.

[28] J. Homola, S. S. Yee, G. Gauglitz, *Sensors Actuators B Chem.* **1999**, *54*, 3.

[29] J. E. Baio, D. J. Graham, D. G. Castner, *Chem. Soc. Rev.* **2020**, *49*, 3278.

[30] B. Holzer, K. Manoli, N. Ditaranto, E. Macchia, A. Tiwari, C. Di Franco, G. Scamarcio, G. Palazzo, L. Torsi, *Adv. Biosyst.* **2017**, *1*.

[31] E. T. Roberts, M. N. Haan, J. B. Dowd, A. E. Aiello, *Am. J. Epidemiol.* **2010**, *172*, 48104.

[32] D. G. Myszka, *Curr. Opin. Biotechnol.* **1997**, *8*, 50.

[33] D. G. Myszka, P. R. Arulanantham, T. Sana, Z. Wu, T. A. Morton, T. L. Ciardelli, *Protein Sci.* **1996**, *5*, 2468.

[34] D. G. Myszka, X. He, M. Dembo, T. A. Morton, B. Goldstein, *Biophys. J.* **1998**, *75*, 583.

[35] K. Sigmundsson, G. Másson, R. Rice, N. Beauchemin, B. Öbrink, *Biochemistry* **2002**, *41*, 8263.

[36] L. A. Segel, M. Slemrod, *SIAM Rev.* **1989**, *31*, 446.

[37] L. Bar, J. Dejeu, R. Lartia, F. Bano, R. Richter, *Anal. Chem.* **2020**, *92*, 5396.

[38] J. L. Pellequer, M. H. V Van Regenmortel, J. L. Pellequcr, *J. Immunol. Methods* **1993**, *166*, 133.

[39] S. Liu, H. Zhang, J. Dai, S. Hu, I. Pino, D. J. Eichinger, H. Lyu, H. Zhu, *MAbs* **2015**, *7*, 110.

6 p-Tau$_{181}$ Biosensor

In this chapter, a new configuration of EGOT is introduced, different from the top-gated EGOT presented in this thesis. This side-gate EGOT was utilized for detecting p-Tau$_{181}$, a biomarker for Alzheimer's Disease. Through this study, we examine how the binding event affects the threshold voltage and its correlation with the potential change at the gate electrode.

6.1 INTRODUCTION

6.1.1 p-Tau: Alzheimer's Disease biomarker

Alzheimer's Disease (AD) is a prevalent form of dementia and neurodegenerative disease. It is characterized by the gradual deterioration of the central or peripheral nervous system, leading to a decline in memory and cognition. While the exact cause of Alzheimer's disease remains unclear, research suggests that it may involve various factors such as inflammation, mitochondrial dysfunction, oxidative stress, and changes in protein clearance, with age being considered to be the most significant risk factor.[1,2] In a representative population sample of 70-year-olds, the prevalence of pathologic AD markers was 46%.[3]

Neuroimaging is currently the most accurate technique for AD prediction, but new biomarkers are needed for better drug development, personalized medicine, and pre-clinical diagnosis, especially for distinguishing AD from other neurodegenerative diseases, since it is very challenging due to the frequent co-pathology.[4] Understanding the pathophysiology of AD by investigating the many disease mechanisms and their progression over time, as well as its correlation with other neurodegenerative diseases, is crucial for finding reliable biomarkers.[5] Among the many potential biomarkers, fluid biomarkers are gaining more interest for improving diagnostics accuracy, prognosis, and monitoring response to the treatments, as well as for early disease diagnosis. In **Figure 6.1** we can find a schematic diagram of the many mechanisms involved in Alzheimer's Disease and several potential fluid biomarkers.

The cerebrospinal fluid (CSF) is situated in immediate proximity to the extracellular milieu of the brain, thereby rendering any biochemical alterations within the brain to be reflected on the CSF. Therefore, any changes on CSF levels of biomarkers for AD may provide insight into the central pathogenic process.[3,4] The pathogenesis of Alzheimer's disease involves the activation of innate immunity and microglial cells, which results in the hyperphosphorylation and oligomerization of the Tau protein.[6] Precisely, phosphorylated Tau (p-Tau) protein is one of the most promising biomarker with high selectivity of 80% and specificity of 92% for AD; these values are the result of analysing 36 different studies, including about 2500 AD patients and 1400 controls.[3] Unlike the other two main candidates, total Tau and $A\beta_{1-42}$, p-Tau is apparently the only biomarker that is not increased under other neuropathologies, highlighting its important role as biomarker for AD for its discrimination from other co-pathologies.[3,4,7]

Within the several p-Tau proteins, according to the phosphorylated site, Tau protein phosphorylated at threonine position 181 ($p\text{-}Tau_{181}$) is the most common biomarker for AD diagnosis, with an 85 % selectivity, slightly above the p-Tau average. It has been measured as

biomarker for AD, giving great importance to its role or discriminating AD from other dementia diseases, and the average CSF values of p-Tau$_{181}$ for AD were established at ~ 70 pg/mL, being 2 to 3 times the values from healthy control subjects.[8–10]

Therefore, this AD biomarker p-Tau$_{181}$ has been chosen as one of the target molecules for the development of EGOT-based biosensors. The current standard technique for the detection of p-Tau proteins is based in the enzyme-linked immunosorbent assay (ELISA).[8–10] However, a more direct technique, that does not require large volumes of biological samples and with less sophisticated equipment would be desirable for its implementation in the clinical practice.

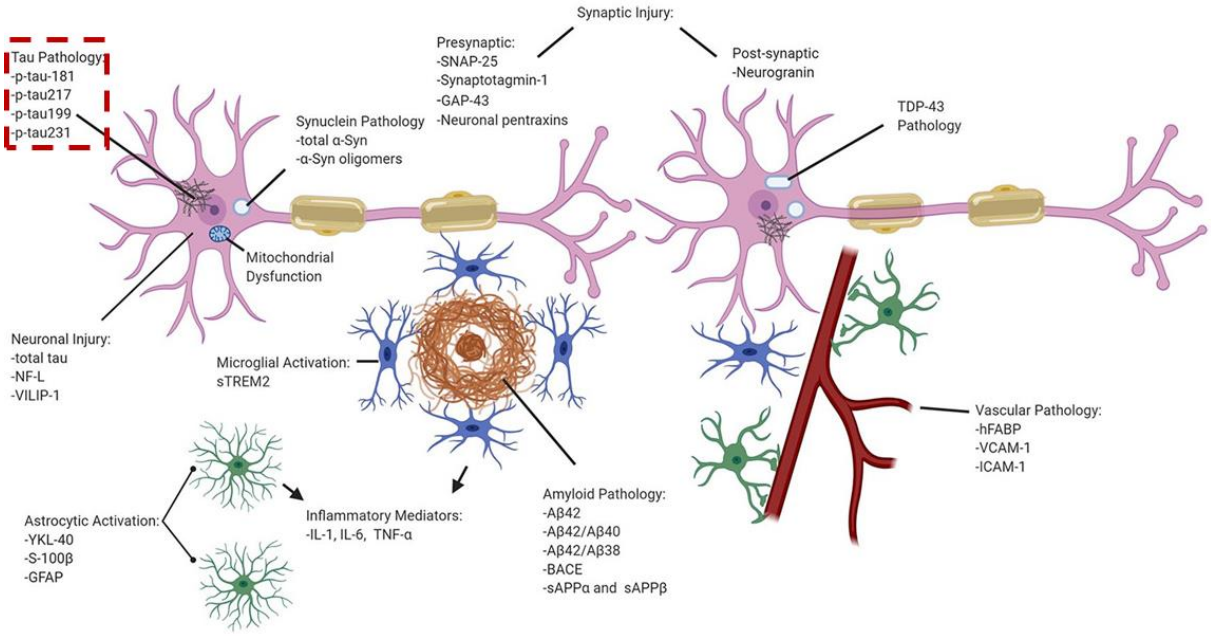

Figure 6.1. Schematic diagram of many potential biomarkers of Alzheimer's Disease and their implication on other co-pathologies. This figure was adapted from a review by Rawan Tarawneh.[5]

6.1.2 DPP-DTT EGOT-based biosensors

In this work, we propose an alternative sensing platform for the detection of p-Tau$_{181}$ and for its potential implementation at the Point-of-Care (PoC) testing. Electrolyte Gated Organic Transistors (EGOTs) have emerged as a very promising architecture for label-free sensing, due to their ability to amplify small biological signals in biological samples and transform them into readable electrical signals, bridging the gap between the biological and technological world.[11–15]

EGOTs can be classified as Electrolyte Gated Organic Field Effect Transistors (EGOFET) or as Organic Electrochemical Transistors (OECT). Both architectures are composed by three electrodes: drain (D) and source (S) electrodes which are interconnected by means of an organic semiconductor (OSC) material forming the channel. Subsequently, this channel is

connected to a third electrode, the gate (G), via the electrolyte. Under these circumstances, the gate capacitance is very high, higher than its counterpart Organic Field Effect Transistors (OFETs) by 3 orders of magnitude approximately. This allows the operability at very low voltages (<1 V), which is of great importance when interfacing with biological components. and when working in aqueous environment to avoid undesired faradaic processes. [16]

The architecture of choice for this biosensor was a side-gated EGOT, which can feature controlled design by photolithography yielding a very precise gate geometry. Additionally, when used into optoelectronics devices, having the surface above channel (unlike the top-gated configuration) uncovered is of great importance.[17]

The polymer DPP-DTT, explained in more detail in Chapter 2, was the OSC material used for the fabrication of EGOT-based biosensors during this work. Organic field effect transistors (OFETs) fabricated with DPP-DTT have shown excellent electrical performances, with reported very high hole mobility and ON/OFF ratio values, 10.5 cm^2 V^{-1} s^{-1} and 10^6 respectively.[18] In recent years, EGOTs with DPP-DTT as OSC have been reported in literature for their great electrical performance.[19–23] These EGOTs have been used not only as sensors for analyte detection in electrolyte, but also for interfacing cell cultures, showing good stability over time, which is one of the main drawbacks of such devices.[21]

6.2 EGOT FABRICATION

6.2.1 Transistor fabrication

EGOTs were fabricated on a quartz substrate featuring interdigitated drain and source electrodes, as previously described in Chapter 2.1.1, with a channel width/length (W/L) of 2000. The substrates were first cleaned in accordance with the following protocol: i) a first rinse with acetone to remove the photoresist layer and gently drying with nitrogen flow, ii) then a washing step in hot acetone (70 °C for 10 minutes), and iii) a final washing step in piranha solution (H_2SO_4:H_2O_2 1:1) for 1 minute at 150 °C, followed by iv) abundant rinsing with water and drying in nitrogen flow. The OSC DPP-DTT (5mg mL^{-1} in DMSO) was deposited by spin coating at 2000 rpm for 2 minutes, followed by a thermal annealing step in the oven at 140 °C for 45 minutes. Devices were stored immersed in 50 mM Phosphate Buffer solution (pH 7.4) until use.

6.2.2 Gate Functionalization

To complete the biosensor fabrication, we need to provide the device with biorecognition capabilities. During this work we used a planar gold gate electrode on a Kapton substrate that was functionalized with anti-p-Tau_{181} Ab, exploiting the well-known Protein G strategy,

explained in more detail in Chapter 2.1.4. Before functionalization the gate was cleaned in an ultrasonication bath in 1% Hellmanex II for 5 minutes. The substrate was then rinsed with acetone and ethanol and dried under N_2 flow. The functionalization process was performed as follows: (i) previous reduction step of the disulfide bound of the cy-Protein G with tributyl phosphine and tris (2-carboxyethyl) phosphine (TCEP), (ii) gate overnight incubation in 2 mg mL^{-1} reduced cys-Protein G in 50 mM Phosphate Buffer at 4 °C, (iii) Incubation in 0.1 mg mL^{-1} anti-p-Tau_{181} antibody in 50 mM Phosphate buffer pH 7.4 for 1 hour. (iv) incubation in 10 μM OEG in water for 30 minutes at room temperature, followed by a final passivation step of (v) incubation in 0.1 mg mL^{-1} BSA in Phosphate Buffer for 30 minutes are room temperature.

6.2.3 Characterization of Functionalization Process

6.2.3.1 Electrochemical Characterization

The sensing interface in EGOTs can be either at the gate/electrolyte or at the channel/electrolyte interface, albeit the latter is less commonly utilized.[24] For the p-Tau_{181} sensor, the antibody was immobilized at the gate/electrolyte interface, using a Protein G monolayer as an anchoring matrix. This strategy has been widely adopted for Ab immobilization, exploiting the high affinity of Protein G to the heavy chains of immunoglobulins G (IgG) and ensuring a precise and uniform orientation of the Ab at the gate electrode.[25–28] Additionally, Protein G can be molecularly engineered to bear a single Cysteine (Cys) residue on the surface, facilitating the creation of covalent bonds with the gold surface. This functionalization step has been monitored electrochemically by means of Cyclic Voltammetry (CV) as shown in **Figure 6.2 A**. The measurements were performed in a three-electrodes setup: the gate electrode was the working electrode, and Ag/AgCl and Pt wire were reference and counter electrodes, respectively. We used a 5mM $K_3[Fe(CN)_6]$ solution as a redox probe, containing 1 M KCl as a supporting electrolyte. Upon examining the CV, we can see that only partial (i.e. sub-monolayer) coverage of the gate electrode is attained following the chemosorption of Protein G. This is indicated by a larger peak-to-peak distance and a decrease in current density. These changes are the result of the reduction of electron exchange between the redox probe ($[Fe(CN)6]^{3-}$/$[Fe(CN)6]^{4-}$) in solution and the electrode. By applying the Randles-Sevcik equation (refer to Chapter 2.3, eq. 2.2), we analyzed the changes in current density and estimated the gate coverage with Protein G. The result showed that 23.6±3.7 % of the gold surface was passivated. This result is lower than what has been reported in the literature (~40% coverage). Following the protein G adsorption, the antibody immobilization was also monitored with cyclic voltammetry, showing no further coverage of the gate electrode, which

is expected since the antibody binds only the protein G which is already on the surface. As a final step, OEG was used as antifouling agent, leading to a full coverage of the remaining bare gold spots, as witnessed by the reduction in faradaic current as a consequence of the complete blockage of the electron exchange between the redox probe and the electrode.

6.2.3.2 Electrical Characterization

The subsequent steps of the functionalization process were monitored by electrical characterization using an EGOT with the functionalized gold electrode as the gate (**Figure 6.2 B**). Transfer curves were recorded after each functionalization step, starting from the gate with the already formed Protein G monolayer. We can observe a decrease in drain current after each functionalization step. However, the most significant decrease occurs after the passivation process with OEG. This is likely due to the formation of a compact monolayer that covers the exposed gold spots following Protein G immobilization.

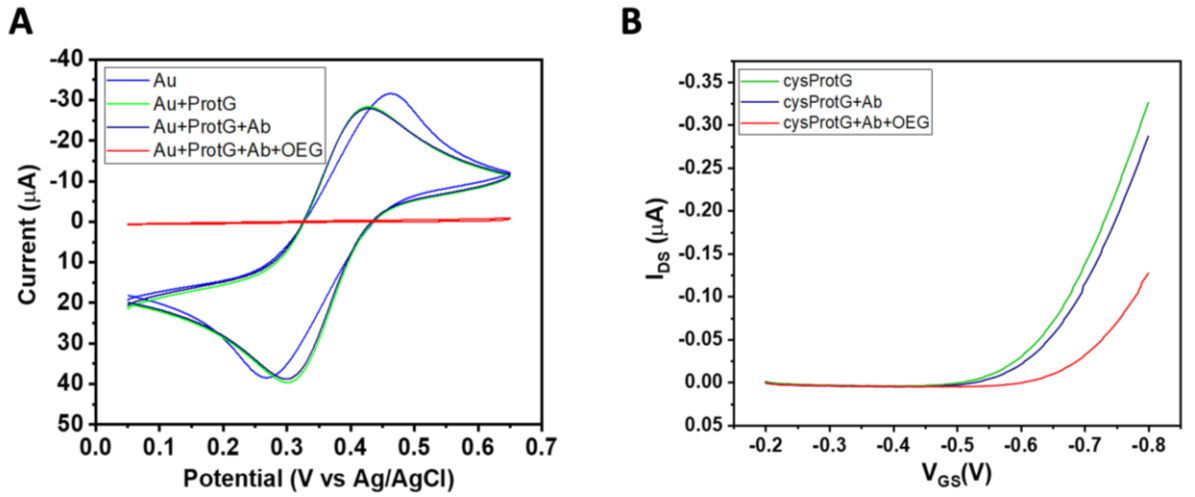

Figure 6.2. Electrochemical and electrical characterization of the gate functionalization process. **A)** Cyclic voltammograms monitoring the chemisorption of Protein G (light green line) on the gold surface. Measurements were performed in 5 mM $K_2[Fe(CN)_6]_3$ solution containing KCl. **B)** Transfer curves recorded after each functionalization step. Measurements were performed in 50 mM Phosphate Buffer solution, pH 7.4.

6.3 BIOSENSOR RESPONSE

6.3.1 Transfer Curves

The functionalized planar gold was integrated into the EGOT architecture as a gate electrode in a side-gated configuration. Kapton and quartz substrates were assembled together on a PDMS support to avoid leakages from the joint. The EGOT devices were operated inside a Faraday cage using an Agilent B2912A Source Measure Unit. Transfer curves were recorded by applying a sweeping gate-source potential (V_{GS}) from -0.3 V to -0.8 V, and a fixed drain-source potential (V_{DS}) of -0.2 V.

Incubation in p-Tau_{181} was carried out *ex situ*, by only exposing the functionalized gate to artificial cerebrospinal fluid (aCSF) containing increasing concentrations of p-Tau_{181} and measuring the response by means of change in drain current in 50 mM Phosphate Buffer solution pH 7.4. A first stabilization step was performed by recording continuous transfer curves in 50 mM Phosphate Buffer solution until superimposable curves were observed, this would take approximately 20 to 30 minutes. Next, the gate was exposed to aCSF (namely blank) by incubation for 15 minutes and gently washing with buffer solution, followed by recording transfer curves. This step was repeated 6 – 7 times testing the device stability by controlling that the corresponding transfer curves obtained in fresh blank solutions would be superimposable, as expected. Finally, the gate was incubated in aCSF containing p-Tau_{181} in concentrations ranging from 25 pg mL^{-1} to 200 pg mL^{-1} for 15 minutes each concentration, followed by gentle washing. The sensor response was measured by recording transfer curves in 50 mM Phosphate Buffer after *ex situ* exposure to each concentration.

Figure 6.3 shows the response of a DPP-DTT EGOT-based biosensor to increasing concentrations of p-Tau_{181} protein in an aCSF at the gate electrode. The drain current (I_{DS}) decreased monotonically at all explored gate voltages with increasing p-Tau_{181} concentration. The current decrease was relatively small for the lowest concentration (25 pg mL^{-1}) and more marked for higher concentrations. The concentration range explored is of clinical relevance, covering the physio-pathological concentrations of p-Tau_{181} in CSF, with a threshold for discriminating patients affected by Alzheimer's Disease at about 70 pg mL^{-1}.[9,10] This behaviour was consistent across 6 independent experiments, indicating the robustness and reproducibility of the device response to the target analyte.

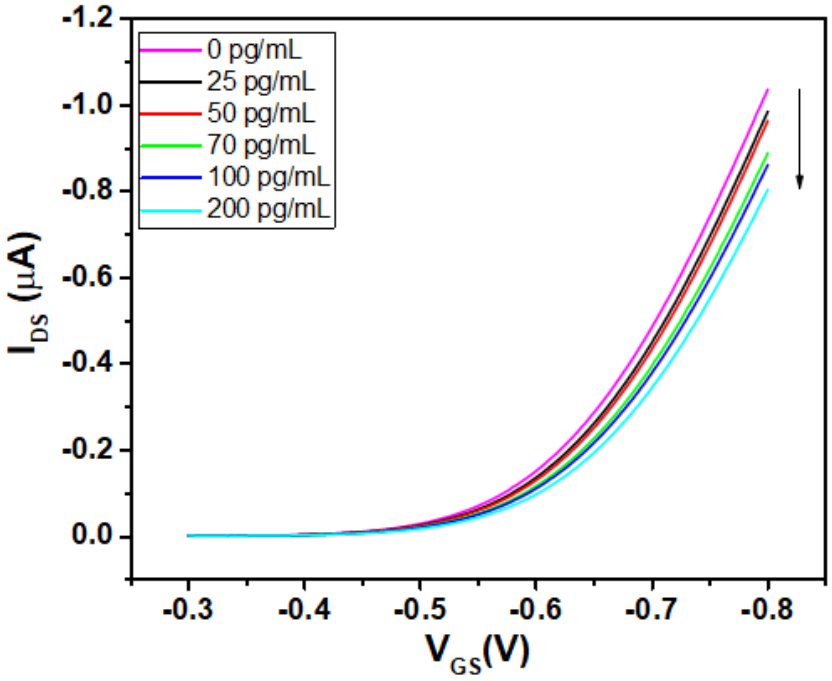

Figure 6.3. Transfer characteristics of DPP-DTT EGOT-based biosensor monitoring the changes in drain current upon analyte binding at the functionalized gate. Transfer curves were recorded in 50 mM Phosphate Buffer solution, pH 7.4, at a fixed V_{DS} of -0.2 V.

We also wanted to analyse the response of the sensor in terms of changes in transconductance (g_m), which represents the slope of the linear region of the transfer curve. It can be expressed as:

$$g_m = \frac{W}{L}\mu C_G V_{DS} \qquad (6.1)$$

where W and L are the channel width and length, respectively, μ is the charge carrier mobility, C_G is gate capacitance, and V_{DS} is the drain voltage.[29]Taking into consideration that W/L ratio and the V_{DS} are fixed values, changes in g_m can only be attributed to changes in the product μC_G, which in turn can be affected by the binding of the analyte at the gate electrode. The changes as function of p-Tau$_{181}$ concentration are depicted in **Figure 6.4**, g_m was calculated as the first derivative of the transfer curve as function of V_{GS}. One can observe by visual inspection that the curves are slightly shifted but keeping the same slope and with similar maximum g_m, with a maximum shift < 10%. This would suggest that the drain current changes are mainly due to a shift in threshold voltage (V_{th}). We think that by increasing the gate electrode area to 50 times the size of the channel, the impact of capacitance would be reduced, allowing V_{th} to have a dominant effect.

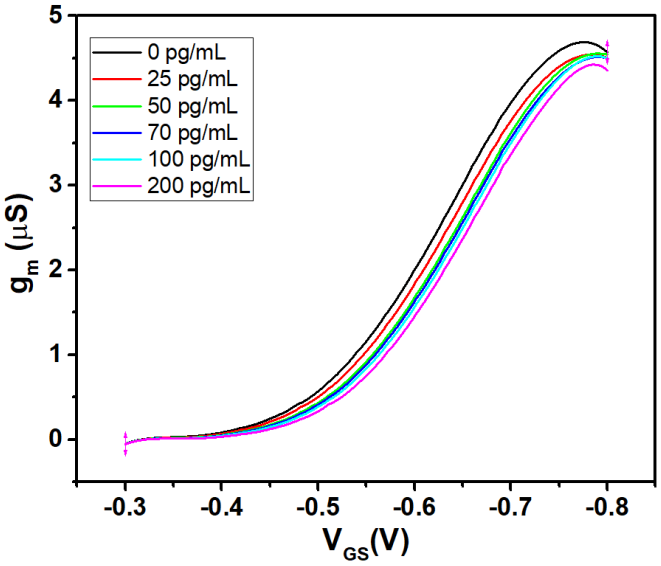

Figure 6.4. Changes in transconductance (g_m) as a response to the analyte binding at the gate electrode across different V_{GS}. Transconductance curves were calculated from the first derivative of the transfer curves recorded at a constant V_{DS} = -0.2 V.

6.3.2 Response quantification

By analyzing changes in the transfer curves, we can gain insight into the impact of the binding events at the gate electrode on the electrical response of the device. EGOTs are multiparametric devices that allow us to quantify and correlate changes not only in I_{DS}, but also in V_{th}, or g_m with the concentration of the analyte. The simplest and most used quantification method is studying the changes in I_{DS} expressed in terms of signal S, which has been already presented in the previous chapters. However, a less commonly used way of quantifying the sensor response is by normalizing the relative changes in drain current by the transconductance, expressed as: $\Delta I_{DS}/g_{m[0]} = (I_{DS[c]} - I_{DS[0]})/g_{m[0]}$, measured at a given V_{GS}.[30] For this set of data, the changes in drain current were calculated at V_{GS} = -0.63 V, which is within the threshold region for all 6 devices; such gate voltage regime has been proved to yield the highest sensitivity in previous reported EGOT-based biosensors.[31–33] By normalizing the change in current by the g_m, one might expect to estimate the change in surface charge Δq induced by the adsorbent which modifies the surface potential and therefore shifts the threshold voltage. [30] In parallel, the shift of V_{th} was also quantified as a function of [p-Tau$_{181}$], by taking the V_{th} at concentration 0 pg mL^{-1} as reference. Indeed, as suggested by Reed and co-workers, the following equation relates the change in drain current normalized by transconductance to the threshold voltage shift: [30]

$$\Delta \frac{I_{DS}}{g_m} = \Delta V_{th} = \frac{\Delta q}{c_0} \qquad (6.2)$$

where c_0 quantifies the capacitive coupling between the analyte molecules and the channel. [30] The results are presented in **Figure 6.5**, showing that the shift of the gate potential upon analyte binding (black squares) very closely mirrors the shift in V_{th} (blue squares), not only in terms of trend but even in magnitude, with a maximum V_{th} shift of 27 mV towards more negative values at [p-Tau$_{181}$] = 200 pg mL^{-1}. From the plot we can see that both normalized drain current changes and threshold voltage shifts increase in magnitude monotonically with increasing concentrations of p-Tau$_{181}$, almost reaching saturation at the highest concentration [p-Tau$_{181}$] = 200 pg mL^{-1}. Based on these findings, it can be concluded that alterations caused by the binding of the analyte are most likely linked to alterations in the gate potential rather than the total capacitance. The sensor successfully detects p-Tau$_{181}$ in the physio-pathological concentration range in aCSF.

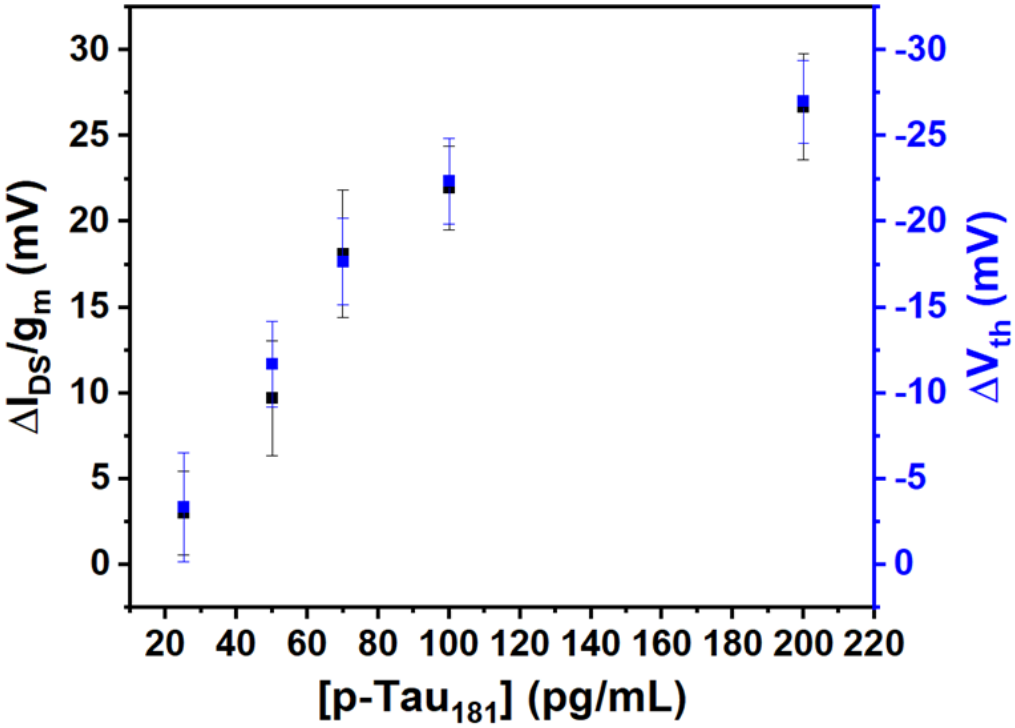

Figure 6.5. Black squares: dose curve in terms of $\Delta I_{DS}/g_{m[0]}$ *vs.* [p-Tau$_{181}$], change in current and g_m were calculated at V_{GS} = -0.63 V and V_{DS} = -0.2 V. Blue squares: shift in V_{th} *vs.* [p-Tau$_{181}$]. The data points are calculated as the average of 6 independent experiments with error bars representing the SEM.

From the previous results, it is apparent that the binding event leads to changes in V_{th}; therefore, further analysis will be performed by means of this parameter. To gain insight into the thermodynamics of the recognition between the surface immobilized anti-p-Tau$_{181}$ antibody and the corresponding antigen, the dose curve of ΔV_{th} *vs.* [p-Tau$_{181}$] was further analyzed using both the "classical" and a modified Langmuir model isotherm. We introduce here the Uniform

Langmuir model, which accounts for the existence of numerous binding sites on the electrode surface. These sites are assumed to possess binding energies (U) that are supposed to be evenly dispersed throughout the $U_{min}<U<U_{max}$ range.[34] When the Uniform Langmuir model is used, which neglects, as the Langmuir model, interactions between adsorbates, the resulting isotherm will reflect the distribution of binding energies across the adsorption sites. The Uniform Langmuir model can be expressed as:

$$S = \frac{S_{max}}{2A} ln\left(\frac{1+K_{avg}e^{A}c}{1+K_{avg}e^{-A}c}\right) \quad (6.3)$$

where A is a parameter defined as:

$$A = \frac{1}{2k_BT}(U_{max} - U_{min}) \quad (6.4)$$

With S_{max} representing the maximum signal, which corresponds to the saturation of the binding sites, K_{avg} is the average binding constant (corresponding to a Langmuir constant of a hypothetical material with adsorption sites characterized by uniform binding energy), c is the analyte concentration, k_B is the Boltzmann constant, and T is the temperature. The successful fitting with this model has been previously reported by our group for the analysis of binding between cortisol and its corresponding antibody immobilized on the gate of a CNT-FET: the significant improvement in the fitting capability of the Uniform Langmuir model with respect to the standard version indicated that in that case a variety of different binding sites could be attributed to a random orientation of the antibodies, yielding a heterogeneous electrode surface.[35] On the contrary, as witnessed in **Figure 6.6**, both classical Langmuir and the Uniform Langmuir model yield a satisfactory fit of our data, with no marked difference between the two models from visual inspection. From the extracted parameters, the Langmuir model and the Uniform Langmuir model yielded a K_D of 103 and 100 if expressed in terms of pg mL^{-1}, respectively, which would correspond to 1×10^{-12}. The parameter A, which is associated to the heterogeneity of the sensing surface, takes a rather small value ($\sim10^{-5}$): this would hint to the fact that in the present case the adsorption sites are quite uniform in terms of binding energy. This would imply that in the present case ΔU takes an almost negligible value, which further highlights that all the binding sites have the same or very similar binding affinity, like in the classical Langmuir model. These results can be explained by the fact that we are using Protein G for grafting the antibody to the electrode surface, which should impart an expected unique orientation of the antibody with respect to the surface at variance with randomly oriented antibodies immobilized on gate surfaces by EDC/NHS coupling to self-

assembled monolayers exposing carboxylic headgroups. It is important to notice though that the experimental concentration range explored is very narrow, which suggests that care should be taken when interpreting the thermodynamic parameters obtained by fitting with the described models.

Another important parameter for biosensors is the limit of detection (LOD), which can be calculated as the $V_{th[0]}$ + 3σ, where $V_{th[0]}$ is the average signal from the blank, and σ is the standard deviation. For the p-Tau$_{181}$ sensor, the calculated theoretical LOD was 26 pg mL^{-1}, which is equivalent to 0.45 pM. This value indicates that the first experimental point at 25 pg mL^{-1} should be discarded, and it was therefore not included in the fitting analysis (see **Figure 6.6**). Our devices have therefore proved to detect p-Tau$_{181}$ in the physio-pathological concentration range, with a very low theoretical LOD. This is, to the best of our knowledge, the first time an EGOT-based biosensor has been reported for the detection of p-Tau$_{181}$. Previous transistor-based biosensors have been developed for the detection of p-Tau,[36] at all phosphorylation sites, and for p-Tau$_{127}$,[37] which, like p-Tau$_{181}$, is a very promising biomarker for the very specific detection of AD, also with good reproducibility and low LOD.

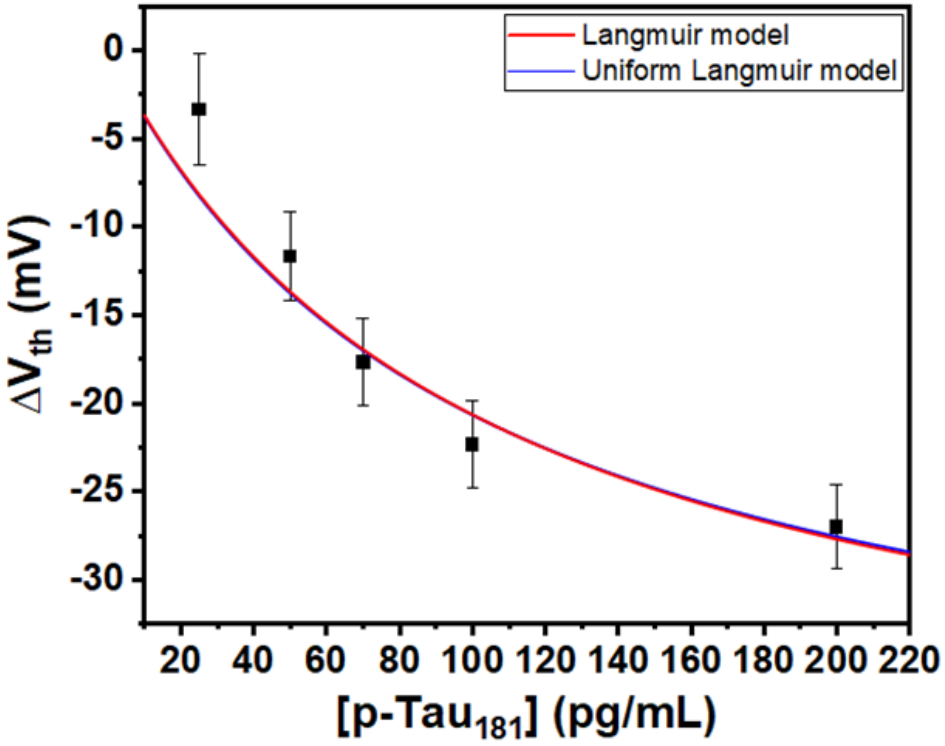

Figure 6.6. Dose curves in terms of ΔV_{th} *vs.* [p-Tau181]. The classical Langmuir fitting is represented as a red line, while the uniform Langmuir fitting is represented by a blue line. The data shown is the average of 6 independent experiments with its respective SEM.

6.3.3 Control Experiments

To test the device selectivity, we exposed the functionalized gate electrode to a high concentration of cytokine IL-6, which is a possible interfering protein. In certain conditions, such as AD, the levels of this pro-inflammatory cytokine can increase up to 23 pg mL^{-1},[38,39] and even reach hundreds of pg mL^{-1} for other age-related diseases.[40] As a control experiment, we also conducted tests by functionalizing the gate electrode with anti-cortisol Ab instead of anti-p-Tau_{181} Ab. We tested the sensor response to *ex situ* exposure of the functionalized gate to increasing concentrations of p-Tau_{181} protein. In this case, no response was expected due to the absence of a specific biorecognition unit against p-Tau_{181}. Again, the sensor response was quantified in terms of *S* as a function of analyte concentration. In **Figure 6.7** a comparison between the sensor response against [p-Tau_{181}] and the two controls described before is depicted; the dashed line represents the LOD, which is the smallest concentration that can be detected with reasonable certainty. We can see that the signal of the p-Tau negative control (i.e. with immobilized antibody not specific towards p-Tau, light blue circles) is very small in magnitude, invariably below the LOD even at the highest p-Tau_{181} concentration explored and not displaying any concentration-dependent trend. Also, the IL-6 control, for which only a high concentration of 200 pg mL^{-1} was investigated shows an almost negligible signal below the LOD. From these results we can safely claim that our developed p-Tau_{181} EGOT-based biosensor is sensitive in the physio-pathological concentration range, tending towards saturation at the highest concentrations (> 100 pg mL^{-1}) and with selectivity towards the target as proved by the control experiments.

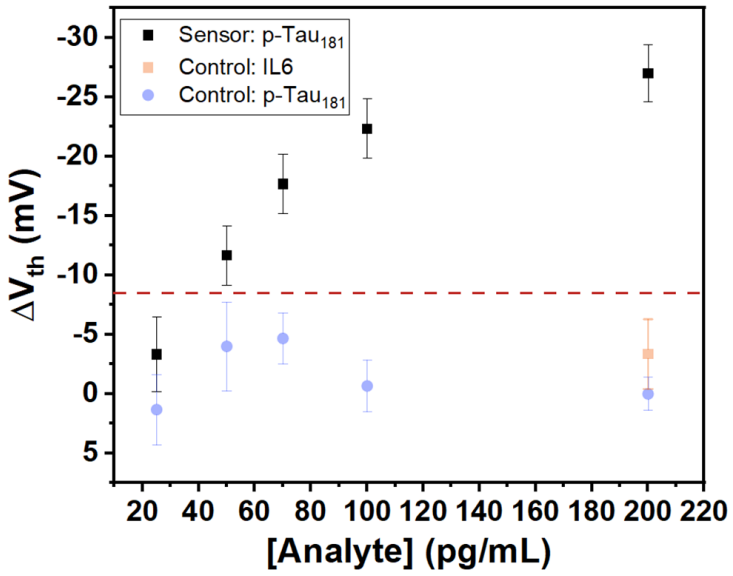

Figure 6.7. Comparison of the dose curve (black squares, ΔV_{th} *vs.* [p-Tau]) compared with the sensor response to the control experiments. IL-6 control (pink square) is the developed p-Tau sensor exposed to a high (200 pg mL^{-1}) concentration of IL-6, and p-Tau$_{181}$ (blue square) is an EGOT-based biosensor with a different antibody not specific towards p-Tau$_{181}$, exposed to increasing concentration of p-Tau$_{181}$. The dashed line represents the LOD of the biosensor. The signal of the controls is the average of 3 independent experiments with its respective SEM.

6.4 CONCLUSIONS

In this chapter, we evaluated the detection of p-Tau$_{181}$ by EGOT-based biosensors. We explored a side-gated configuration, which differs from the top-gated transistors mentioned in previous chapters during this thesis. The gate electrode used was considerably larger than the channel, with the aim of reducing the effect of changes in capacitance following binding between antigen and antibody on the device response. Indeed, the comparison between the drain current change normalized by the transconductance with the V_{th} shift shows very similar values, suggesting that the device response is indeed dominated by electrostatic effects upon analyte binding. We investigated the thermodynamics of the binding between p-Tau$_{181}$ and its corresponding antibody by applying either the Langmuir or the Uniform Langmuir model: the two isotherms yield very similar values, possibly hinting to the fact that the adsorption sites on the gate surface might have a narrow distribution of binding energies. Our independent experiments showed good consistency and successfully detected p-Tau$_{181}$ at concentrations ranging from 50 pg mL^{-1} to 200 pg mL^{-1} in a complex medium such as artificial cerebrospinal fluid, with a theoretical limit of detection (LOD) of 26 pg mL^{-1}. These results, together with the negligeable non-specific response, corroborate the successful applicability of EGOT-based biosensor for the detection of p-Tau$_{181}$.

Other transistors-based biosensors, reported in the literature, have been developed for the detection of other p-Tau-based biomarkers, [36,37] with excellent performances and sensing capabilities, demonstrating a growing interest in this technology for sensing purposes applied to neurological disorders.

6.5 REFERENCES

[1] O. Sheppard, M. Coleman, in *Azheimer's Dis. Drug Discov.* (Ed.: X. Huang), **2020**, pp. 1–22.

[2] S. J. Fuller, H. R. Sohrabi, K. G. Goozee, A. Sankaranarayanan, R. N. Martins, *Neurodegener. Alzheimer's Dis. Role Diabetes, Genet. Horm. Lifestyle* **2019**, 9.

[3] S. Kern, H. Zetterberg, J. Kern, A. Zettergren, M. Waern, K. Höglund, U. Andreasson, H. Wetterberg, A. Börjesson-Hanson, K. Blennow, I. Skoog, *Neurology* **2018**, *90*, e1682.

[4] E. Andersen, B. Casteigne, W. D. Chapman, A. Creed, F. Foster, A. Lapins, R. Shatz, R. P. Sawyer, *Biomarkers in Neuropsychiatry* **2021**, *5*, 100041.

[5] R. Tarawneh, *Biomark. Insights* **2020**, *15*.

[6] R. B. Maccioni, A. González, V. Andrade, N. Cortés, J. P. Tapia, L. Guzmán-Martínez, *Open Neurol. J.* **2018**, *12*, 50.

[7] W. Tang, Q. Huang, **2014**.

[8] T. T. Seppälä, A. M. Koivistoa, P. Hartikainenb, S. Helisalmia, H. Soininena, S.-K. Herukka, *J. Alzheimer's Dis.* **2011**, *25*, 583.

[9] E. B. Erhardt, J. C. Adair, J. E. Knoefel, A. Caprihan, J. Prestopnik, J. Thompson, S. Hobson, D. Siegel, G. A. Rosenberg, *Front. Aging Neurosci.* **2021**, *13*, 1.

[10] S. Morimoto, M. Takao, H. Hatsuta, Y. Nishina, T. Komiya, R. Sengoku, Y. Nakano, A. Uchino, H. Sumikura, Y. Saito, K. Kanemaru, S. Murayama, *PLoS One* **2017**, *12*, 1.

[11] M. Berggren, A. Richter-Dahlfors, *Adv. Mater.* **2007**, *19*, 3201.

[12] J. Rivnay, R. M. Owens, G. G. Malliaras, *Chem. Mater.* **2014**, *26*, 679.

[13] D. T. Simon, E. O. Gabrielsson, K. Tybrandt, M. Berggren, *Chem. Rev.* **2016**, *116*, 13009.

[14] L. Torsi, M. Magliulo, K. Manoli, G. Palazzo, *Chem. Soc. Rev.* **2013**, *42*, 8612.

[15] X. Strakosas, M. Bongo, R. M. Owens, *J. Appl. Polym. Sci.* **2015**, *132*, 41735.

[16] D. Wang, V. Noël, B. Piro, *Electronics* **2016**, *5*.

[17] K. Xu, S. K. Fullerton-Shirey, *J. Phys. Mater.* **2020**, *3*.

[18] J. Li, Y. Zhao, H. S. Tan, Y. Guo, C. A. Di, G. Yu, Y. Liu, M. Lin, S. H. Lim, Y. Zhou, H. Su, B. S. Ong, *Sci. Rep.* **2012**, *2*, 1.

[19] R. Giridharagopal, J. Guo, J. Kong, D. S. Ginger, *Cite This ACS Appl. Mater. Interfaces* **2021**, *13*, 34624.

[20] B. Schmatz, A. W. Lang, J. R. Reynolds, B. Schmatz, A. W. Lang, J. R. Reynolds, *Adv. Funct. Mater.* **2019**, *29*, 1905266.

[21] Y. Zhang, Q. Zeng, Y. Shen, L. Yang, F. Yu, *ACS Appl. Mater. Interfaces* **2020**, *12*, 56216.

[22] K. Chennit, N. Delavari, S. Mekhmoukhen, R. Boukraa, L. Fillaud, S. Zrig, N. Battaglini, B. Piro, V. Noël, I. Zozoulenko, G. Mattana, *Adv. Mater. Technol.* **2023**, *8*, 2200300.

[23] T. T. K. Nguyen, H. V Tran, T. T. Vu, S. Reisberg, V. Noël, G. Mattana, M. C. Pham, B. Piro, *Biosens. Bioelectron.* **2019**, *127*, 118.

[24] B. Burtscher, P. A. Manco Urbina, C. Diacci, S. Borghi, M. Pinti, A. Cossarizza, C. Salvarani, M. Berggren, F. Biscarini, D. T. Simon, C. A. Bortolotti, *Adv. Healthc. Mater.* **2021**, *2100955*.

[25] A. E. Sauer-Eriksson, G. J. Kleywegt, M. Uhlén, T. A. Jones, *Structure* **1995**, *3*, 265.

[26] M. Berto, E. Vecchi, L. Baiamonte, C. Condò, M. Sensi, M. Di Lauro, M. Sola, A. De Stradis, F. Biscarini, A. Minafra, C. A. Bortolotti, *Sensors Actuators, B Chem.* **2019**, *281*, 150.

[27] K. Solodka, M. Berto, D. Ferraro, C. Menozzi, M. Borsari, C. A. Bortolotti, F. Biscarini, M. Pinti, *Adv. Mater. Interfaces* **2022**, *9*.

[28] C. Diacci, M. Berto, M. Di Lauro, E. Bianchini, M. Pinti, D. T. Simon, F. Biscarini, C. A. Bortolotti, *Biointerphases* **2017**, *12*.

[29] K. Melzer, M. Brändlein, B. Popescu, D. Popescu, P. Lugli, G. Scarpa, *Faraday Discuss.* **2014**, *174*, 399.

[30] X. Duan, Y. Li, N. K. Rajan, D. A. Routenberg, Y. Modis, M. A. Reed, *Nat. Nanotechnol.* **2012**, *7*, 401.

[31] M. Berto, S. Casalini, M. Di Lauro, S. L. Marasso, M. Cocuzza, D. Perrone, M. Pinti, A. Cossarizza, C. F. Pirri, D. T. Simon, M. Berggren, F. Zerbetto, C. A. Bortolotti, F. Biscarini, *Anal. Chem.* **2016**, *88*, 12330.

[32] X. P. A. Gao, G. Zheng, C. M. Lieber, *Nano Lett.* **2010**, *10*, 547.

[33] P. A. Manco Urbina, M. Berto, P. Greco, M. Sensi, S. Borghi, M. Borsari, C. A. Bortolotti, F. Biscarini, *J. Mater. Chem. C* **2021**, *9*, 10965.

[34] H. Swenson, N. P. Stadie, *Langmuir* **2019**, *35*, 5409.

[35] A. Paradisi, M. Berto, M. Di Giosia, S. Mazzali, M. Borsari, D. Marforio, F. Zerbetto, M. Calvaresi, A. Orieshyna, N. Amdursky, C. A. Bortolotti, F. Biscarini, *Chem. A Eur. J.* **2023**.

[36] M. Á. García-Chamé, Ó. Gutiérrez-Sanz, E. Ercan-Herbst, N. Haustein, M. S. Filipiak, D. E. Ehrnhöfer, A. Tarasov, *Biosens. Bioelectron.* **2020**, *159*, 112129.

[37] S. H. Ciou, A. H. Hsieh, Y. X. Lin, J. L. Sei, M. Govindasamy, C. F. Kuo, C. H. Huang, *Biosens. Bioelectron.* **2023**, *228*, 115174.

[38] J. P. Jia, R. Meng, Y. X. Sun, W. J. Sun, X. M. Ji, L. F. Jia, *Neurosci. Lett.* **2005**, *383*, 12.

[39] R. Taipa, S. P. das Neves, A. L. Sousa, J. Fernandes, C. Pinto, A. P. Correia, E. Santos, P. S. Pinto, P. Carneiro, P. Costa, D. Santos, I. Alonso, J. Palha, F. Marques, S. Cavaco, N. Sousa, *Neurobiol. Aging* **2019**, *76*, 125.

[40] M. H. Ji, H. M. Yuan, G. F. Zhang, X. M. Li, L. Dong, W. Y. Li, Z. Q. Zhou, J. J. Yang, *J. Anesth.* **2013**, *27*, 236.

7 FINAL REMARKS

This chapter encompasses a comparison of the different EGOT devices fabricated and characterized during this thesis, in terms of electrical performance, as well as with respect to their operation as biosensors.

During this work, three OSC materials were explored, as reported in Chapter 2 – 6, namely the small-molecule TIPS-Pentacene, and polymers PEDOT:PSS and DPP-DTT. Before the operation of these devices as sensors, they were characterized in phosphate buffer solution, using a pristine gold wire electrode as a gate in a top-gated configuration. We will now compare the performances of the different kinds of devices developed throughout this thesis**.** Error! Reference source not found. shows typical transfer (**A**) and output (**B**) curves, in this specific case these are the recorded curves from an EGOT device fabricated on a commercial Micrux substrate using DPP-DTT as OSC (for more details please refer to Chapter 2). We provide them here as an example, since these curves are used to extract the figures of merit of the devices that we used for comparing their electrical performances also with respect to the biosensing capability.

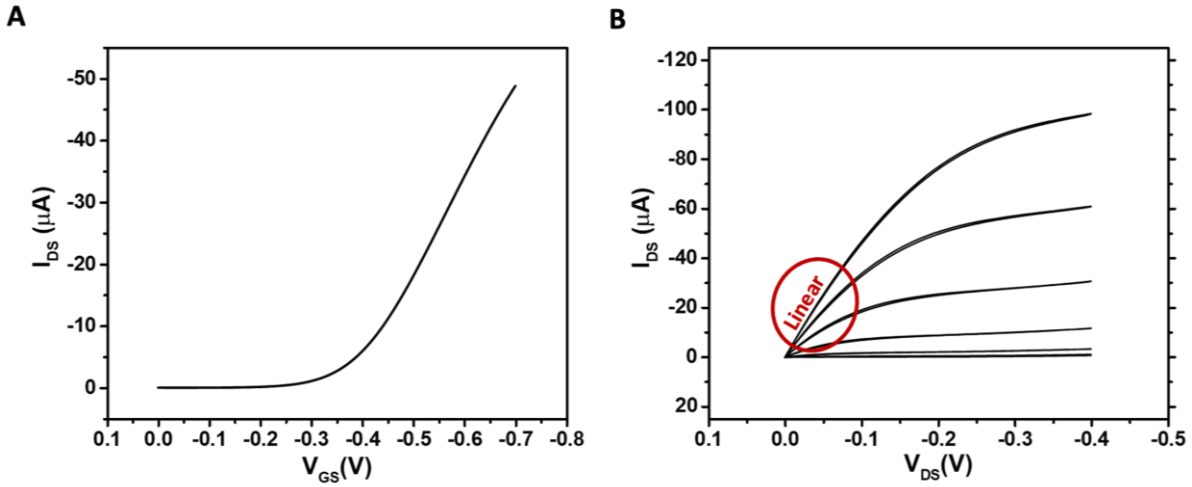

Figure 7.1. Electrical characterization of EGOT, using DPP-DTT as OSC. **A)** Transfer curve recorded by applying a sweeping V_{GS} from 0 to -0.8 V, and a constant V_{DS} potential of -0.1 V. **B)** Output curve recorded by applying a sweeping V_{DS} from 0 to -0.5 V, and an increasing V_{GS} from 0 to -0.7 V, with -0.1 V per step; the linear regime is highlighted. Measurements were performed in Phosphate Buffer solution.

Indeed, the EGOT devices were electrically characterized in terms of the following figures of merit: the threshold voltage (V_{th}), the ON/OFF ratio, and the maximum transconductance ($g_{m,max}$), all these parameters were obtained from the transfer curves. The output curves are used to identify the linear and saturation regimes. The V_{DS} value was chosen so that the transfer curves would always be obtained in the linear regime. When working in this regime, the equation describing the dependence of the drain current on geometrical and operational parameters is the following[1]:

$$I_{DS} = \frac{W}{L} C_{CDL} \mu (V_{GS} - V_{th}) V_{DS} \qquad \text{Eq. 7.1}$$

Where $\frac{W}{L}$ is the channel width/length ratio, C_{CDL} is the capacitance of the charge-double-layer, and μ is the charge carriers mobility. In our case the charge carriers are invariably holes because all three OSCs are p-type materials [2]. The $g_{m,max}$ was extracted from the maximum the first derivative of the transfer curve (dI_{DS}/dV_{GS}), while V_{th} was obtained from the second derivative of the transfer curve. Finally, the devices were also characterized in terms of stability[3], which was calculated as the percentage of the initial I_{DS} retained after 10 minutes of continuous transfer curves collection, except in the case of OECT fabricated by drop casting PEDOT:PSS, since measurements were performed in I_{DS} *vs.* time, the stability was calculated from the drift in the baseline after 10 minutes of continuous measurement.

Overall, five devices combinations of device architecture, active materials and sensing targets were explored throughout the thesis: **(1)** EGOFET featuring TIPS-Pentacene and **(2)** OECT using PEDOT:PSS as OSC for the detection of IL-6, **(3)** OECT featuring PEDOT:PSS for the detection of anti-CMV Ab, EGOT using DPP-DTT as OSC for the detection of **(4)** IL-1β and **(5)** p-Tau$_{181}$. Both OECTs differ in the processing technique used for the deposition of the OSC, in **(2)** PEDOT:PSS was deposited by spin coating, in **(3)** by drop casting. In **(4)**, the OSC was deposited on glass substrate, while in **(5)**, it was deposited on quartz substrate, featuring a *W/L* of 49 000 and 2000, respectively.

Table 7.1 displays the figures of merit of the electrical characterization of the above-described EGOTs; these parameters are reported as the average of five devices with its respective SEM for each case. The V_{th} was only measured for EGOFET and EGOT fabricated with DPP-DTT, it was not possible to estimate it from the OECTs transfer curves because in the operating potential window, the devices are not reaching the off state. With respect to this figure of merit, we can clearly see a difference between TIPS-Pentacene- and DPP-DTT-based devices, the former yielding V_{th} lower (by roughly 50%) than the latter. The devices fabricated with DPP-DTT show a slightly lower V_{th} when the *W/L* is increased by 25-fold, but it is invariantly significantly higher than TIPS-Pentacene devices. In terms of ON/OFF ratio, the material that leads to a higher value is DPP-DTT. Devices fabricated with DPP-DTT and PEDOT:PSS have comparable ON current values, however, PEDOT:PSS based devices do not reach the OFF state, therefore no comparison of the ON/OFF ratio values can be made between these materials. When also comparing the TIPS-Pentacene based devices, the current values in the ON state are much lower, while the "OFF" vales are comparable with those obtained for DPP-DTT-based devices. Between the two DPP-DTT based devices, the one with a higher *W/L* ratio yields an ON/OFF ratio one order of magnitude larger, in line with expectations. Along the

same line, the devices fabricated with DPP-DTT featuring a *W/L* of 49 000 yielded the highest $g_{m,max,}$ as expected considering that transconductance is directly proportional to *W/L*. Besides, OECTs, which feature the lowest *W/L* values, also yield very high $g_{m,max}$, because of the very large tree-dimensional capacitance of PEDOT:PSS channel due to its permeability to ions penetration[4]. Finally, in terms of stability, all five devices showed a good stability in the phosphate saline solution and in aCSF during the time course of the experiment. The material that displayed the lowest stability was TIPS-Pentacene, which also showed to be more sensitive to environmental conditions, such as detergent Tween 20, as mentioned in Chapter 3. This detergent had to be removed from the assay buffer when working with TIPS-Pentacene based devices architecture because it severely worsened its electrical performance, while OECTs based on PEDOT:PSS showed unaltered electrical performances in the presence of Tween 20. The investigated PEDOT:PSS OECTs prepared by drop casting yielded the highest stability, by maintaining 99.67% of its initial drain current after 10 minutes of measurement. It is important to notice that in this case, the stability was measured by applying a constant V_{GS} and V_{DS}, unlike the other cases where the drain current was measured after recording continuous transfer curves, with a sweeping V_{GS} and a constant V_{DS}. This satisfactory stability was closely followed by DPP-DTT based EGOTs, independently of the substrate material and *W/L* ratio. ratio.

Table 7.1 Comparison of EGOT devices in terms of threshold voltage (V_{th}), ON/OFF ratio, maximum transconductance ($g_{m,max}$), and stability.

OSC	W/L	V_{th} (V)	ON/OFF ratio	$g_{m,max}$ (µS)	Stability (%)
TIPS-Pentacene	2000	-0.23 ± 0.03	1.7 (± 0.3)x10^2	3.5 + 0.4	85.02 ± 4.66
PEDOT:PSS (spin coating)	50	-	-	173.5 ± 31.7	93.48 ± 2.28
PEDOT:PSS (drop casting)	50	-	-	181.8 ± 90.9	99.67 ± 0.12
DPP-DTT	49 000	-0.44 ± 0.03	2.1 (± 0.8)x10^4	757.9 ± 58.6	96.96 ± 0.72
DPP-DTT	2000	-0.54 ± 0.01	2.8 (± 1.0)x10^3	20.2 ± 4.5	96.20 ± 1.72

Table 7.2 is a summary of the five developed biosensors for four aging biomarkers. Among them, the biomarkers are different proteins, ranging from small (17 kDa) to large (150 kDa) biomacromolecules. All four proteins have an isoelectric point (pI) below 7.4, which is the pH at which all electrical measurements were performed, therefore all of them are expected to be

negatively charged under such conditions. When analyzing the EGOT-based biosensors response, we obtained that the binding of the two cytokines, IL-6 and IL-1β, led to an increase in drain current, while the detection of the larger proteins anti-CMV Ab and p-Tau$_{181}$, led to a decrease in drain current. This shows that the sign of the current change cannot be predicted solely based on the charge of the protein. Indeed, we are working with four different immobilization strategies, which can affect the sensor response and amplification mechanisms at the gate/electrolyte interface, as discussed in Chapter 4. Finally, the analysis of the thermodynamics of each sensor showed that all architectures are valid for studying the thermodynamics and, in one case, even the kinetics of biorecognition events. From our results, IL-6 and p-Tau$_{181}$ biosensors exhibited the best performance in terms of sensing, reaching LOD well below the pM concentration range, and with association binding constant in line with values reported in the literature. The reproducibility of the sensor response can be inferred from the data points of the dose curves, which are provided with their associated SEM, showing a fairly good reproducibility among the independent experiments.

Table 7.2. Summary of the EGOT-based biosensors for the detection of IL-6, IL-1β, anti-CMV Ab, and p-Tau$_{181}$.

Analyte			**EGOT**		**Biosensor**		
Name	*Size (kDa)*	*pI*	*Functionalization*	*OSC*	*LOD (M)*	*Isotherm model*	K_a
IL-6	21.1	6.2	SAM-forming linkers	TIPS-Pentacene	$4x10^{-14}$	Frumkin	$6.09(\pm1.69)x10^{11}$
				PEDOT:PSS	$3x10^{-13}$		$1.44(\pm0.49)x10^{12}$
IL-1β	17	4.7	Avidin/biotin layer	DPP-DTT	$1x10^{-9}$	Langmuir	$2.27(\pm0.21)x10^{7}$
anti-CMV Ab	150	5.5	Metal-ion chelate affinity	PEDOT:PSS	$5x10^{-10}$	Langmuir	$1.20(\pm0.20)x10^{7}$
p-Tau$_{181}$	48-70	<6.3	Protein G sub-monolayer	DPP-DTT	$5x10^{-13}$	Langmuir	$5.59(\pm2.15)x10^{11}$

From these two tables, we can infer that the material that yields the best electrical performances is PEDOT:PSS, followed by DPP-DTT, and finally TIPS-Pentacene. However, when comparing the final sensor device, IL-6 EGOT-based biosensors and p-Tau$_{181}$ EGOT-based biosensor showed a better performance in terms of sensing. A real comparison of the biosensors is not possible, since for each sensor, the substrate, the OSC, and the gate functionalization strategy are different. However, it is apparent that all three materials, although with some differences, are excellent choices for the development of EGOT-based biosensors, and that the main factor determining the biosensing capability of the device appears to be the sensing interface, taking into consideration the functionalization strategy, as well as the biorecognition element. This goes in line with what was observed in Chapter 3, when IL-6 EGOT-based

biosensors were compared, based on the same functionalization strategy, but featuring two different OSC materials, TIPS-Pentacene and OECT. In this case, both architectures could be compared because they only differ with respect to the OSC, showing very similar sensing performances in terms of LOD and sensitivity. In addition, the thermodynamic analysis provided in Chapter 3 for these two biosensors unified the sensor response for both architectures, suggesting that it is dominated by events at the sensing interface, and independent from the OSC material.

Finally, further work should continue in the development of a microfluidics setup and multiplexing architecture to merge those individual biosensors for the simultaneous detection of all four biomarkers. To this end, a prototype was developed in collaboration with Deniz Saygin, Fabio Biscarini and Pierpaolo Greco at the Italian Institute of Technology (IIT, Ferrara) and University of Ferrara. **Figure 7.2 A** shows the design of the proposed EGOT architecture, featuring a large gate and interdigitated drain and source electrodes. **Figure 7.2 B** displays the microfluidics prototype for two sensors in a multiplexing configuration. The microfluidics chamber was made of PDMS, which was successfully integrated with the device fabricated on Kapton. This prototype represents the first step that was taken towards implementing a sensor for simultaneous detection of the different analytes, for which individual biosensors were developed as described in the present thesis.

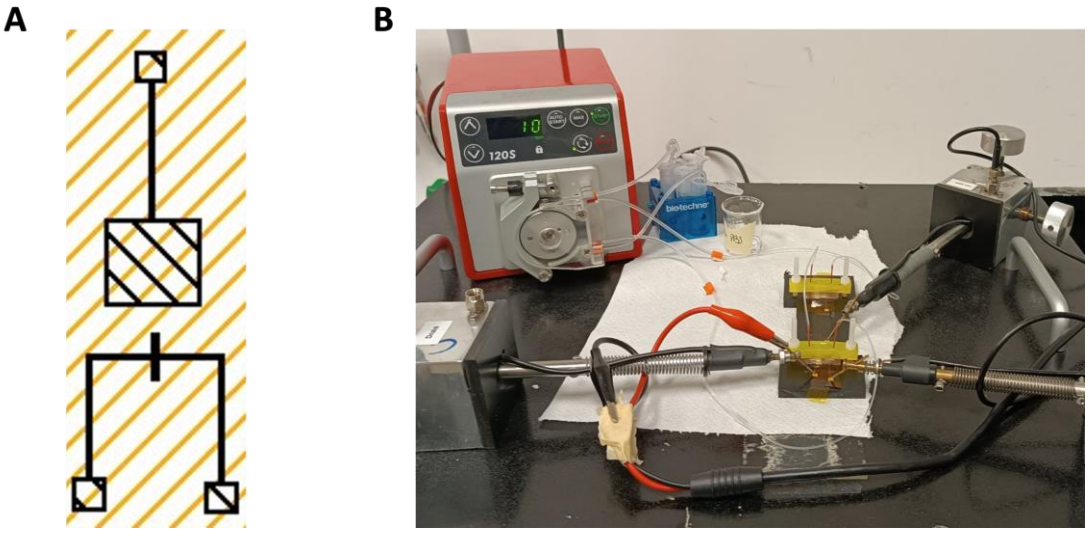

Figure 7.2. A) Design of the co-planar EGOT architecture, to be fabricated on kapton by photolithography. **B)** First prototype of the microfluidics setup for multiplexing.

7.1 REFERENCES

[1] E. Macchia, K. Manoli, C. Di Franco, R. A. Picca, R. Österbacka, G. Palazzo, F. Torricelli, G. Scamarcio, L. Torsi, ACS Sensors 2020, 5, 1822.

[2] D. Wang, V. Noël, B. Piro, Electron. 2016, 5.

[3] A. Nawaz, Q. Liu, W. L. Leong, K. E. Fairfull-Smith, P. Sonar, Adv. Mater. 2021, 33, 1.

[4] J. Rivnay, S. Inal, A. Salleo, R. M. Owens, M. Berggren, G. G. Malliaras, Nat. Rev. Mater. 2018, 3.

8 CONCLUSIONS

The main goal of this thesis was the development of organic transistor-based biosensors for the detection of aging biomarkers. Despite the lack of one specific aging biomarker, several longitudinal studies suggest that pro-inflammatory cytokines are associated with pathological aging, as well as the immune response to the infection by cytomegalovirus (CMV). The levels of these markers have been reported in elevated concentrations in the elderly. Additionally, phosphorylated Tau (p-Tau) protein is a promising biomarker of Alzheimer's Disease, which is also an age-related disease. Taking all this into consideration, the chosen potential aging biomarkers were the cytokines interleukin-6 (IL-6) and interleukin-1b (IL-1β), IgG anti-CMV antibody, and the p-Tau protein. The current standard techniques for the detection of such proteins are reliable and robust; however, they present some drawbacks that limit their implementation in clinical practice.

In this work, we addressed this need for a more portable, and yet still very sensitive and robust sensing platform. We proposed the fabrication of EGOT devices, which are endowed with biorecognition capabilities towards the target molecule. EGOTs are characterized by low-cost manufacturing, easy operability, a fast and real-time response, and biocompatibility; additionally, the possibility of operating in a liquid environment and its easy integration into a microfluidics system would allow the implementation of these devices at the PoC testing.

For the development of these sensing devices, three different organic semiconductor materials were investigated, and four functionalization strategies were studied and optimized using electrochemical and optical techniques. The functionalization was performed on the gate electrode surface for all EGOT devices.

For the first biomarker, IL-6, we explored both EGOT architectures, EGOFET and OECT, proving high sensitivity and specificity towards the target analyte. The sensor exhibited a good response in the physio-pathological range in buffer solutions. In this case, we used these devices not only for analytical purposes but also for thermodynamic studies, proving that EGOTs are a valuable tool for investigating the binding events at the gate/electrolyte interface. In a similar approach, an IL-1β EGOT-based biosensor was developed, and the gate sensing capabilities were tested with optical techniques and compared to the EGOT response. In this case, neither the optical nor electrical devices showed sensitivity in the sub pM range, which is the relevant concentration range for IL-1β in circulation. Although the EGOT-based

biosensor proved to be reproducible and specific to the target analyte, it needs to be further optimized for its application in routine testing.

The previously mentioned sensing devices were operated in static conditions. On the contrary, for the sensing of anti-CMV antibodies, the OECT-based biosensor was integrated with a microfluidics system, providing a real-time response. First, the functionalization strategy, based in the poly-histidine tag technology, was flexible and adaptable to a large variety of analyte/receptor pairs, providing high receptor densities on the surface. Then, by obtaining the binding curves from the real-time measurements, we investigated the kinetics of the biorecognition event, therefore estimating both k_{on} and k_{off} and comparing the thermodynamic affinity constant K_a obtained by kinetic considerations with the value obtained by fitting the equilibrium data with Langmuir model. Among the main findings of this thorough fundamental investigation, was the importance of paying attention to the mass transport limitations at low analyte concentration when working with high-density binding sites on the surface.

Finally, an EGOT-based biosensor was developed for the detection of p-Tau; although it is not strictly an aging biomarker, it is relevant for Alzheimer's Disease, which is an age-related disease. In this case, the explored functionalization strategy provides the sensing interface with potentially uniform antibody orientation towards the target analyte. The sensor response showed high sensitivity and specificity against p-Tau, with very low LOD, in the sub-pM range, which is relevant for circulating p-Tau in biological samples. Further analysis of the thermodynamics of the binding between p-Tau and its corresponding antibody support the argument that the sensing surface is characterized by a uniform distribution of the biorecognition elements, which would allow to interpret the dose curves using the simple Langmuir model.

In summary, this work demonstrated that organic electronics is a promising platform for sensing purposes, but also for investigation of fundamental aspects, both thermodynamic and kinetic, of biorecognition. However, some optimization is still required, especially in terms of sensitivity and performance in complex biological samples. The advantages and characteristics of this technology render EGOT-based biosensors a potential alternative to the current gold standard techniques. Regarding the detection of aging biomarkers, a multi-sensing platform for the simultaneous detection of several biomarkers in biological samples would be desirable; thus, the follow-up of this work will be focused on the integration of the devices with a microfluidics system to obtain a single, multiplex platform for simultaneous detection of the age-related biomarkers.

List of abbreviations

Ab	Antibody
aCSF	artificial Cerebrospinal fluid
AD	Alzheimer's Disease
BSA	Bovin serum albumin
CE	Counter electrode
CHF	Congestive Heaart Failure
CMV	Cytomegalovirus
CMV-pp65	Cytomegalovirus phosphoprotein 65
CNT-FET	Carbonanotuves Field Effect Transistors
COVID-19	Coronavirus disease 19
cps	Counts per second
CRP	C-reactive protein
CSF	Cerebrospinal fluid
CV	Cyclic Voltammetry
DC	Direct current
EDL	Electrical double layer

EG-EGOT	Extended Gate - Electrolyte Gated Organic Transistor
EGOFET	Electrolyte Gated Organic Field Effect Transistor
EGOT	Electrolyte Gated Organic Transistor
EIS	Electrochemical Impedance Spectroscopy
ELISA	Enzyme-linked immunosorbent assay
f-EIS	faradaic Electrochemical Impedance Spectroscopy
FET	Field Effect Transistor
FO	Fiber Optic
FO-SPR	Fiber Optic Surface Plasmon Resonance
g_m	Transconductance
HCMV	Human Cytomegalovirus
I_{DS}	drain current
Ig	Immunoglobulin
I_{GS}	Gate current
IL	Interleukin
IMAC	Immobilized metal affinity chromatography
IRP	Immune risk profile
LOD	Limit of detection

MCH	Mercaptohexanol
MIP	Molecular imprinted polymers
MUA	Mercaptoundecanoic acid
NA	NeutrAvidin
nf-EIS	non faradaic Electrochemical Impedance Spectroscopy
NSR	Normalized sensor response
OECT	Organic Electrochemical Transistor
OEG	Olygoethylene glycol
OFET	Organic Field Effect Transistors
OLED	Organic Light Emitted Diodes
OSC	Organic Semiconductor
PoC	Point-of-care
p-Tau	Phosphorylated Tau
RE	Reference electrode
RIU	Refractive index unit
RT	Room temperature
S	Signal
SAM	Self-assembled monolayer

S_B	SPR sensitivity
SEM	Scanning Electron Microscopy
SEM	Standard error of the mean
SMU	Source measurement unit
SPFS	Surface plasmon-enhanced Fluorescence Spectroscopy
SPR	Surface plasmon resonance
SVA	Solvent vapour annealing
TNF	Tumor Necrosis Factor
TP	Test Pattern
V_{DS}	Drain voltage
V_{GS}	Gate voltage
V_{th}	Threshold voltage
WE	Working electrode

List of figures

Acknowledgements

This PhD journey would have not been possible without the support of many of people during these four years.

I would like to start by thanking my supervisor, Professor C. A. Bortolotti, for giving me the opportunity of performing my PhD his guidance and for introducing me to the world of Organic Electronics. I am grateful for all the knowledge transmitted to me and for his patience over the years. I would also like to thank Professor F. Biscarini for allowing me to work in his laboratory and for all the knowledge shared with me during this project.

I cannot forget all my colleagues from LEO lab UNIMORE: Marcello and Matteo, thank you for teaching from the very first day everything about EGOT and biosensors. Alessandro, thank you for working with me side by side and sharing your experience and knowledge. Kateryna, Deniz, and Sofia, thank you also for your support in the laboratory, the many scientific discussions, and the many pleasant conversations we had whenever we needed a break.

I am grateful for being a Marie Curie Sklodowska Fellow, it not only allowed my PhD journey, but made of it a great scientific and personal experience, giving the opportunity to work in different laboratories and attending to several conferences, and especially for providing all the training needed during those years. In this regard, I would like to thank Professor W. Knoll for hosting me at the Austrian Institute of Technology, to Professor G. Gomila for hosting me at the Institute of Bioengineering of Catalonia, and Professor E. Ismailova for hosting me at Ecole des Mines de Saint-Etienne. I would also like to thank my colleagues from the BORGES consortium, Marina, Shubbam, and with especial mention to Larissa and Roger, with whom we shared many hours in the laboratory, several scientific discussions, but also for teaching me new non-scientific skills such as sailing and flying.

I would also like to thank Chiara for all her help in the administrative stuff, and for teaching me and easing the Italian bureaucracy.

Finally, I would like to thank my whole family, my mom and my dad, and my brother for all their support over the years, for always believing in me an encouraging to pursue my objectives.

Last but not least, I want to thank my friends from Spain, who are like family, and my friends here in Italy, with whom COVID pandemic was bearable.